Abstract

The plasma jet, a commonly used ignition device, has been investigated as a source of acoustic energy suitable for sub-bottom profiling. Named the plasma gun, the device discharges electrical energy in a cylindrical arc ignited in a gaseous environment surrounded by water. When the arc energy evaporates water, it produces a rapidly expanding vapor bubble that creates the acoustic pressure wave.

Acoustic properties of the device are similar to small explosives, and to electric sparkers. Multiple bubble oscillations, a problem of explosive-type sources, are generally less troublesome for the plasma gun than with the sparker sources. Some degree of frequency control of the acoustic pulse is possible if proper values are selected for the electrical circuit components and for the total stored electrical energy. Peak acoustic pressures are controlled both by the total electric energy and by the rate it is delivered to the arc. These quantities are determined by capacitance, inductance, and charging voltage. Frequency components of the primary pressure pulse depend on the arc discharge frequency and on the immersion depth of the device. The bubble period depends primarily on the amount of energy discharged into the water; this in turn is proportional to the total stored electrical energy.

The plasma gun has been compared to small air guns, pingers, sparkers, and boomers. Sub-bottom profiles obtained show penetration less than the 1 in^3 air gun but with more resolution.

Stored energy in the plasma gun, however, was nearly five times less. Penetration was equal and resolution better than electric sparkers of the same energy. Penetration was better and resolution poorer than the pinger, and resolution poorer and penetration slightly better than the boomer source. Except for the sparkers, which used the same power supply, the plasma gun has a decided advantage in equipment size and ease of deployment.

Examiners:

Dr. R. M. Clements, Supervisor (Dept. of Physics and Astronomy)

Dr. G. B. Friedmann, Dept. Member (Dept. of Physics and Astronomy)

Dr. A. Watton, Dept. Member (Dept. of Physics and Astronomy)

Dr. R. N. O'Brien, Outside Member (Dept. of Chemistry)

Dr. D. M. Farmer, Outside Member (Institute of Ocean Sciences)

Dr. D. R. Topham, Outside Member (Institute of Ocean Sciences)

Dr. H. Hoskins, External Examiner
(Woods Hole Oceanographic Institution)

Table of Contents

List of Figures

ACKNOWLEDGEMENTS

I would like to thank my supervisors Dr. Monty Clements for his assistance in the research and the preparation of this dissertation, and for the use of his sailing vessel *Sabrina*, and Dr. David Topham for his guidance in the theoretical portion of the study. Finally to my wife, Janet, very special thanks for putting up with this endeavor this late in our lives.

Special thanks are also due to the Research Associates and Technicians that have been involved in this research during the past six years, in particular: David Ridley, Russell Warren, Gary Sheffler, Lawrence Pitt, David Smith, Peter Ward, Lin Sun and Owen Stephenson. The use of the facilities of the Institute of Ocean Sciences and the Pacific Geosciences Centre is gratefully acknowledged. The help accorded by Dr. T. S. Hamilton of PGC and the officers and crew of the C. S. S. Parizeau was particularly useful. Dr. P. R. Smy and R. F. Halley of the University of Alberta kindly lent their equipment and help for the high speed video images. Adelle Clements kindly gave her editorial expertise.

The financial support provided by the British Columbia Science Council, the Natural Science and Engineering Research Council, Butte College, and by the Physics and Astronomy Department is greatly acknowledged.

CHAPTER 1

Introduction

1.1 Underwater acoustic source historical review.

One of the first references to the use of sound as a tool to locate objects in the sea was by Leonardo da Vinci late in the fifteenth century. The development of underwater acoustics did not proceed in earnest, however, until naval-military establishments required sea detection apparatus to use against opposing forces early in this century. Commercial applications of these military devices have evolved into standard instruments for conventional depth sounding, bottom profiling, detection of sub-bottom geologic features, and communications [Urick 1975].

The majority of underwater acoustic sources now in use present are grouped in two broad areas--impulsive and electromagnetic. The latter type results from the reaction of a material object to periodic electric or magnetic fields. While impulsive sources, including air guns, water guns, and sparkers are necessarily single shot or low repetition rate devices, electromagnetic devices, such as piezoelectric crystals, are able to be used repetitively. The properties of many of these devices are summarized by Bunce [1980]. Impulsive type sources presently in use in underwater acoustics are primarily air guns and to a lesser extent electric sparkers. Because of probable environmental harm, underwater use of large chemical explosives is uncommon.

A class of sources, represented by the boomer, the Uniboom®, and the Bubble Pulser® have some characteristics of both the impulsive and continuous electromagnetic sources. The pulse shape is similar to an impulsive device but the repetition, although at a lower frequency, has similar characteristics to the electromagnetic sources.

Because this dissertation reports the study of the processes of an impulsive acoustic source, the details of repetitive sources will only be discussed peripherally. The impulsive acoustic source is primarily used for sub-bottom profiling. Because the technique used is based on measurements in the far field of the acoustic source, a discussion of the far field is included in Appendix A. Most comparisons of the plasma device will be made to air guns, electric sparkers, and to boomers. The following discussion will provide the background for these devices.

1.1.1 The air gun

The air gun is a pneumatic acoustic source. It consists of an air compressor with storage reservoir, and control system aboard ship. An underwater chamber connected pneumatically and electrically to the ship allows pressurization and control to vent air pressurized between 5 to 30 MPa. The explosive venting of the high pressure air results in an initial pressure wave followed by several bubble oscillations. Each succeeding oscillation has a shorter period because of energy losses to the surroundings. The collapse of the bubble can produce subsequent pressure pulses greater than the initial pressure pulse. Some degree of control of the shape of the pressure signature of an air gun can be achieved by altering the size of the pressure chamber and the amount of air pressure applied [Parkes and Hatton 1986].

1.1.2 The electric sparker.

The electric sparker is one of the simplest devices for producing an acoustic pulse. The system consists of a high voltage power supply, a switching circuit, and a pair of electrodes. On firing, the stored electrical energy is discharged between the two electrodes through the seawater. The discharge vaporizes the seawater into steam, gases, and plasma consisting of various ions, electrons, and atoms. The rapid vaporization produces the initial acoustic pulse. As with the air gun,

contraction and re-expansion of the cooling steam bubble results in a series of pressure pulsations of decreasing periods. Since the sparker produces a bubble primarily of steam, the tendency for repeated bubble oscillations is somewhat reduced compared to the air gun because most gas is condensed after the first contractions (air in the air gun bubble takes longer to be absorbed by the surrounding water [Kramer et al. 1968]). Peak pressures of the collapsing bubbles may also exceed the primary pressure pulse [Kosenko et al. 1980]. Because of the relatively poor conductivity of fresh water compared to sea water electrical sparkers do not work reliably in fresh water unless the voltages used are very high. This also affects their shot-to-shot reproducibility in near shore marine environments of variable salinity. An electrodeless spark underwater sound source having many similar characteristics of sparkers but with better reproducibility has been investigated by Wright [1970].

A certain degree of control over penetration and resolution of a sparkers gives them a versatility comparable to air guns when various power supply and electrode geometry combinations are used. Stored energy can be varied by changing either the value of the storage capacitors in the power supply, the charging voltage, or both. The nature of the electrical discharge--peak current, current duration, and electrical damping can be partially controlled by changing the electrical components of the total circuit--capacitance, inductance, and resistance. The shape of the initial acoustic pulse is also affected by the electrical parameters and electrode geometries; the period of the bubble pulsation depends on the total electrical energy stored in the circuit [Caulfield 1962].

1.1.3 Boomer types of acoustic sources.

These devices, sometimes called pulsed electromagnetic, operate on Lenz' law, i.e. that a changing magnetic field will induce currents in surrounding conductors that will oppose the inducing change. When current in a coil adjacent to a conducting disk (or pair of disks) forces the disks away from the coil, the rapidity of the movement creates a pressure wave in the surrounding water. The shape of the pressure pulse is controlled by the sizes of the disks, the peak current, and the current duration. Because of its mechanical and electrical stability, boomer pressure traces are very reproducible. Boomer sources are directional, the pressure pulse is confined within a cone of approximately 60° with higher frequency components limited to only 10°. In moderate seas this directionality limits the contol of the position of the area insonified by the device (the footprint). Intensity of the pressure pulse is limited by cavitation effects from the plates returning to their equilibrium positions. A loosely fitting flexible membrane to reduce the cavitation covers the outer surface of the conducting disk in the Uniboom® device.

1.2 General considerations for acoustic sources.

An ideal acoustic source would have a very fast rising pressure pulse. This pressure signature would then contain a very wide band of acoustic frequencies which could be used with various combinations of filtering to study different sizes of objects and to probe to different depths. The resolution of an acoustic source depends upon its effective operating frequency, the higher the frequency the better the resolution. Because water and earth materials attenuate acoustic energy approximately as the square of the frequency [Urick 1975], lower frequency sources (poor resolvers) provide better penetration. Real acoustic sources can only approximate the characteristics of an ideal source, and are always a compromise between resolution and penetration. Repeated pressure pulses due to the collapses and expansions of gas bubbles are to be avoided if

possible to prevent further confusion of the acoustic signature [Parkes and Hatton 1986].

Attempts to eliminate bubble oscillations from explosive type devices depend on the destruction of the bubble. Devices have been added to air guns that reinflate the collapsing bubble, preventing it from collapsing. Bubble oscillation can be reduced for airguns and sparkers by towing them slightly submerged so the bubbles break when they pierce the water surface. Unwanted bubble pulsations can also be ameliorated by arrays of individual devices operated at different energies. Because the time between the primary pressure pulse and the bubble pulse depends on the energy deposited into the water, the bubble pulses from different individual sources within an array will occur at differing times, but the primary pulses will all begin at the same time if triggering is simultaneous. Under these conditions, the primary pulses will add constructively whereas the bubble pulses will not. Mathematical techniques exist to deconvolve the primary pressure pulse from the bubble pulse if the shape of the pressure signature is accurately known. Unfortunately individual airguns and sparkers produce varying signatures because the bubbles produced by them do not have the same geometric shape. The pulse shaping that results from using arrays does waste potentially useful energy, but it is expedient.

1.3 Plasma jet historical review.

The following section is included to give the reader some perspective of the operation of the plasma jet, some of the studies of its operation, and some of the uses that have been found for the device.

The origin and the inventors of the pulsed plasma jet are somewhat in dispute. Although several U. S. patents were issued between 1959 and 1971 for spark igniters that use the concept of a central electrode recessed below the surface of the plug, the first published account of the use of the plasma jet as a device to enhance

combustion was given by Topham, et al. [1975]. (Waterston [1973] used a similar device in ignition studies for his doctoral dissertation, but his work remains unpublished).

During the past fifteen years, the plasma jet as an ignition source in internal combustion engines fueled by gaseous and liquid fuels has held the interest of many investigators. Much of this work has been summarized by Clements [1984]. These studies have generally been directed toward the enhanced combustion of leaner than normal mixtures of fuel and air with the hope that more efficient, faster, and cleaner burning would result. The ignition of gases in hostile environments of temperature and pressure has also been investigated. The plasma jet was studied as a source to ignite unattended furnaces in an arctic environment by Cote et al. [1986] and by Pearce et al. [1990], and to reignite a jet engine in a simulated situation of flameout by Cheriyan et al. [1990]. Although the plasma jet devices used by each of the various experimenters are slightly different the essential details are shown in Figure 1.1.

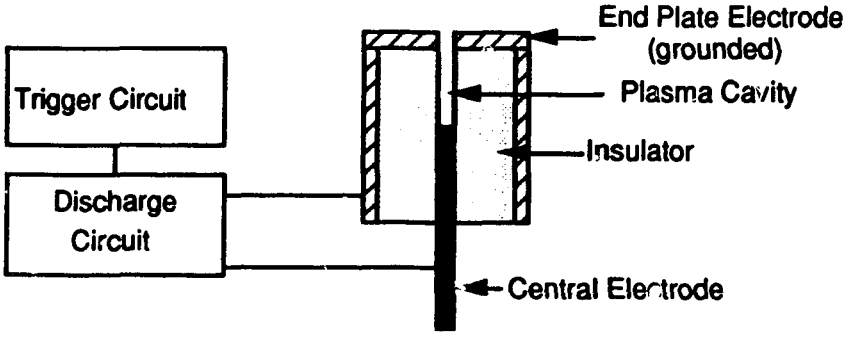

Figure 1.1: Schematic of plasma jet and circuitry.

The discharge circuit consists of two separate sections: a trigger circuit and a storage circuit. In firing, the trigger circuit switches a small charged capacitor across a pulse transformer producing a high voltage across the the cavity of the plasma jet (between the central and the end plate electrodes). This causes the gases in the cavity to

ionize creating a conductive path. The storage circuit containing up to several hundred joules of electrical energy can then discharge currents up to thousands of amperes. The trigger circuit and the storage circuit are isolated from each other by either an inductor or a bank of diodes.

When a large amount of electrical energy is supplied to a plasma in a blind cavity in a short period of time, a jet of plasma is ejected from the open end of the cavity. This plasma contains ions, electrons, and neutral atoms and molecules. Temperatures of the plasma on the order of 10^4 K have been measured by several investigators [Topham 1972a, b]. The highly energetic and chemically active nature of the discharge has been detailed in combustion studies relating to shock heating and turbulence [Topham et al. 1986] and the effect that free radicals and chemistry play in the process has also been reported. [Weinberg et al. 1978], [Clements et al. 1984] and [Ridley et al. 1985].

Topham et al. [1975] were the first to extensively study the nature of the discharge in a gaseous environment in and near the cavity of the plasma jet. They investigated the shape of the discharge using both framing and streak photography, measured pressures on and off axis, and calculated electron density and gas temperature. Smy et al. [1982] measured plasma jet exit velocities of the order of 5×10^3 m/s and showed that there were thin boundaries (< 1 mm) of the jet. The large shear forces that developed result in large instabilities that produced considerable turbulence. The turbulent downstream structure of the plasma jet exhaust investigated in more detail by Smy et al. [1987] was found to be similar to the aerodynamic shock structure characteristic of highly under-expanded jet flow detailed by Adamson and Nicholls [1959].

The detailed development of the arc discharge within the plasma jet cavity linking the energy and momentum of the ejected fluid to the electrical input parameters and the cavity size is being investigated by Topham [1990]. In this analysis the arc process is that of a quasi-steady supersonic jet driven by a variable stagnation pressure

which is similar in temporal shape to the current input waveform. The model simulates an expanding radial electric arc running the length of the cavity acting as a radial piston that produces the necessary driving pressure. Topham's model is based on his earlier works [Topham 1971 and 1972a, b] and on the work of Cowley [1974]. Both studies model a more general class of cylindrical electric arcs and the mathematical techniques that characterize them. The theoretical development of the very early stages of the pressure pulse of the plasma jet discharging underwater in this dissertation is based on these analyses.

1.4 Outline of remaining chapters.

Three objectives guided the work in this dissertation:

1. To investigate the relevant physics involved in discharging the pulsed plasma jet underwater and the acoustic pulse that it develops.
2. To develop a theoretical model which describes the physics as closely as possible.
3. To use a device that evolved from the initial experiments and describe its performance as an underwater acoustic source.

Experiments were carried out in laboratories, from docks and piers, and aboard ship to determine the basic physics of the device. Most of the physics was initially determined from the acoustic pressure signature, which could only be separated from the multitude of acoustic reflections present in small enclosed environments by making measurements aboard ships.

Preliminary experiments involved adapting the traditional plasma jet igniter to discharge reliably underwater and studying the process using high speed imaging methods. Pressure signatures were originally measured in small volume acoustical tanks, but reflection problems indicated measurements should be made in larger environments. Measurements made at the dock of the Royal Victoria Yacht Club yielded positive preliminary results. These led to the

construction of a device that was used as an acoustic source during a geophysical cruise aboard the CSS *Parizeau* along inlets in the mainland coast of British Columbia. The acoustic performance of the device, now named the plasma gun, was by this time deemed to be of sufficient value that patents for the concepts were applied for. (See Patents [1988])

Physical processes that related the stored electrical energy, the arc processes in the plasma cavity, the development of the acoustic pressure pulse in the water, and the extent that the pressure pulse could be controlled were poorly understood during this preliminary experimental period. It was determined that to develop the plasma gun as an acoustic source, detailed measurements of the effects of electrical circuit parameters and plasma cavity geometry had on the pressure signature would be necessary. Near field pressure measurements were conducted in a larger acoustical facility (2.4 m diameter by 2.4 m height) and at the dock of the Institute of Ocean Sciences, Sidney, B. C. Both near and far field signatures were measured in Cadboro Bay and Haro Strait from the sailing vessel *Sabrina*.

A theoretical model relating the pressure signature to the electrical parameters and stored energy that produced reasonable results was developed using previous work on cylindrical electrical arcs, classical acoustics, thermodynamics, and oscillations of bubble cavities in fluids. This model can estimate the pressure signature and parts of its acoustic spectrum.

Finally, a packaged plasma gun was designed and built for use as a sub-bottom profiler. The system was tested extensively using single and multi-element hydrophones detectors and graphic recorders commonly employed for shallow high resolution marine geophysical surveys.

CHAPTER 2

Preliminary experiments

2.1 The prototype device.

The plasma jet operates in a gaseous environment, and thus to operate underwater, gas must be supplied to the plasma cavity. Flowrates of a few millilitres per second are required to produce reliable firing. Initially a standard ignition plasma jet was altered to allow airflow into the plasma cavity. Later, a somewhat more sophisticated apparatus was designed from standard plastic plumbing pipe that allowed the plasma jet to be operated approximately one

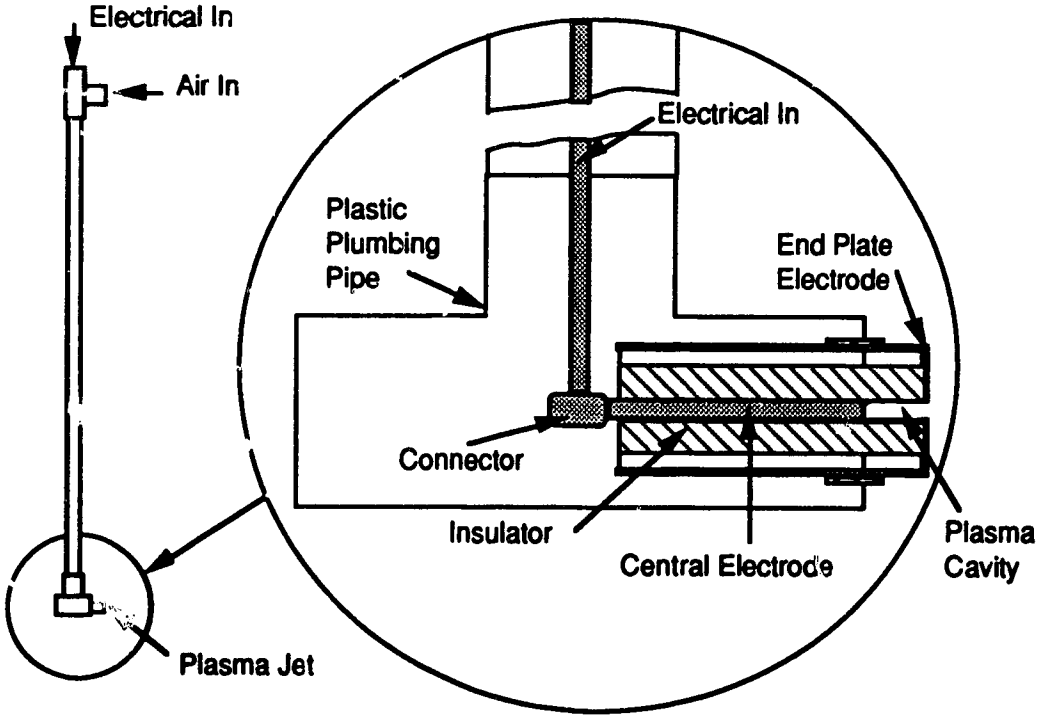

Figure 2.1: Prototype underwater plasma jet.

metre below the water surface. Figure 2.1 shows the basic features of the first underwater plasma jet used in a reasonably open environment. In this device air was supplied to the plasma cavity by pressurizing the entire piping system to a few hundred kilopascals. The annular space between the central electrode and the insulator provided the conduit for the air to pass into the plasma cavity and then into the surrounding water. Power was supplied to the plasma jet by a metal conductor passing coaxially down the inner length of the plastic tubing where it was connected to the central electrode. The end plate electrode was connected by a return cable (not shown) to the power supply. A block circuit diagram of the electrical system is shown in Figure 2.2.

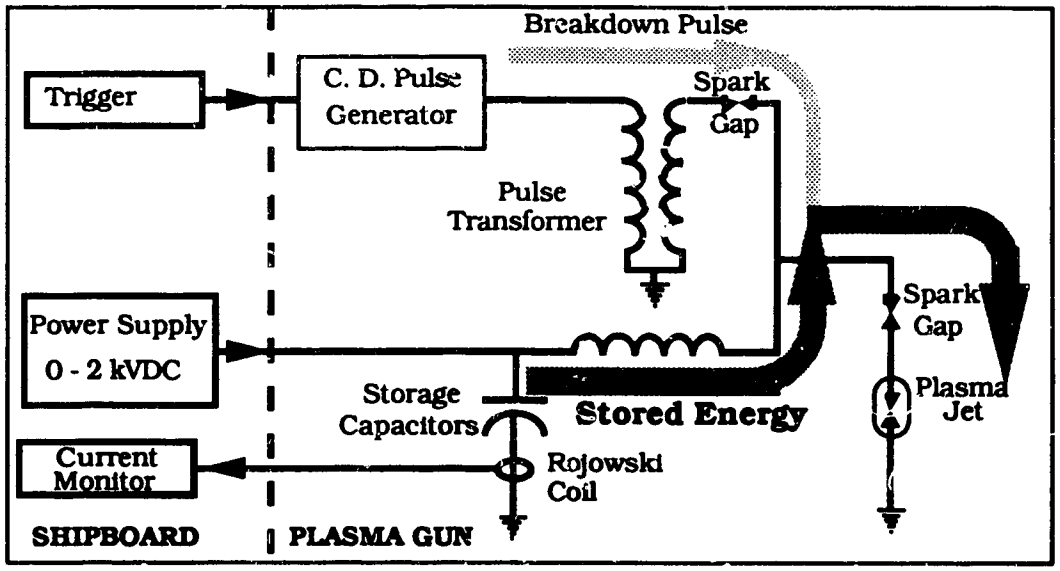

Figure 2.2: Electrical circuit diagram.

High speed photographic experiments were conducted using a Fastax® high speed 16 mm camera to determine the nature of the plasma discharge into the water. The maximum frame rate possible with the camera was approximately two frames per millisecond. Figure 2.3 shows the results of the underwater discharge using a total stored electrical energy of 5 joules.

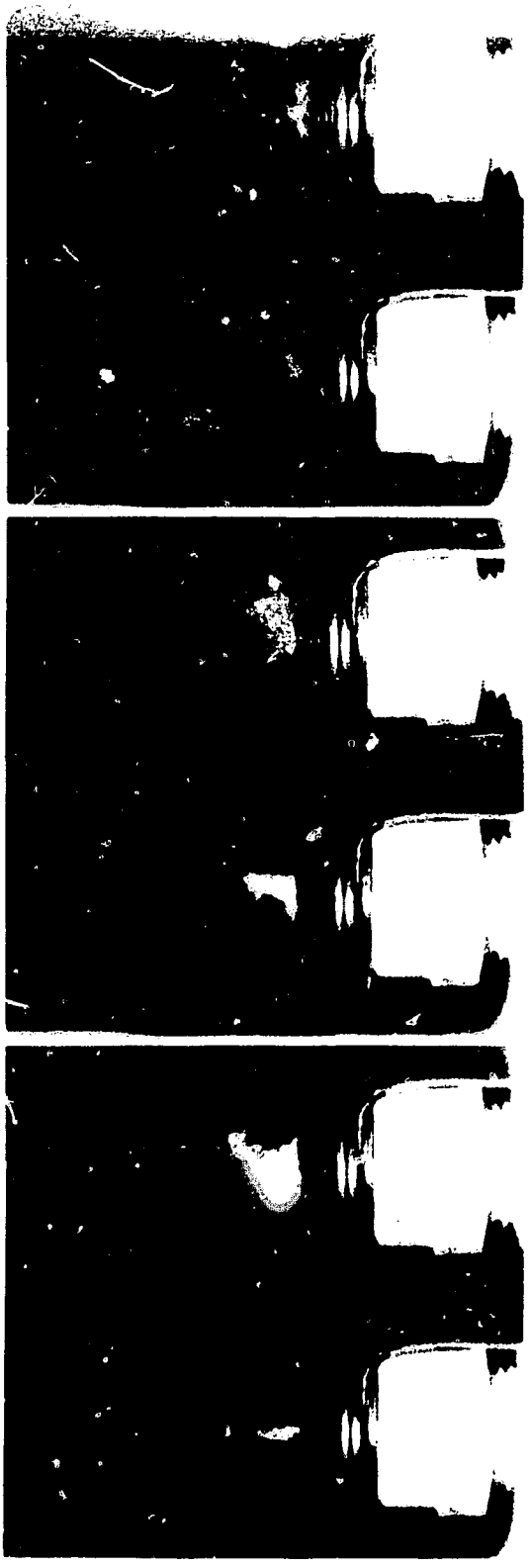

Figure 2.3: High speed photographs of bubble growth after underwater discharge of a 5 J plasma jet. Figure 2.3 a is an uncertain time after discharge. Each succeeding photo is 0.5 ms later.

The major discovery from this part of the study was the appearance of the bubble seen in photographs 2.3a, b, and c. Bubbles of this type are associated with most types of impulsive underwater acoustic sources, e.g. chemical explosives, airguns, and sparkers [Sheriff and Geldart 1982]. These photographs initially led to the belief that the plasma plume, shown in Figure 2.3d, e, and f, issuing from the plasma cavity after the bubble development destroyed the collapsing bubble prior to its complete collapse [Smith, et al. 1987]. A similar set of images taken at the University of Alberta with the Spin Physics® high speed video system using shadowgraph optics shown in Figure 2.4 tends to confirm this idea. While this may be true for some plasma discharges it is not generally the case, Figure 2.5 shows the

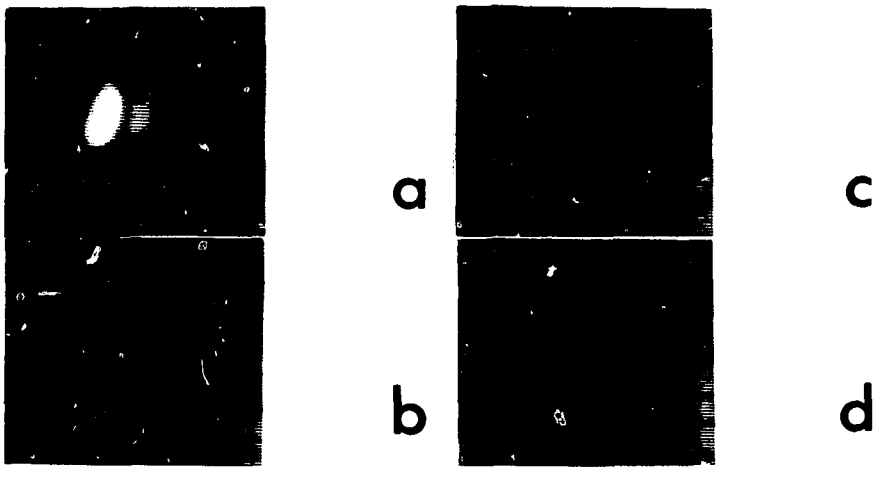

Figure 2.4: Video shadowgraph images of the bubble growth after underwater discharge of a 10 J plasma jet. Image *a* is at time 0, each succeeding image is 0.5 ms later.

shock wave resulting when a bubble collapsed before it was destroyed. This figure is a videograph taken with the Spin Physics® system, using shadowgraph optics at a framing rate of 4 frames per millisecond with exposure time of 200 nanoseconds. Sub-microsecond exposures are required to freeze the motion of the shock wave.

Shadowgraph imaging allows the imaging of objects that have a large difference in refractive index with respect to the background field. It is useful in the imaging of shock fronts, flow fields, and in gas or vapor bubbles immersed in fluids. It may be shown [Goldstein, 1970] that the change in intensity between two points in an image field is proportional to the second derivative of the refractive index with respect to distance in the plane perpendicular to the illumination axis.

Figure 2.5: Video shadowgraph showing shock wave at bubble collapse.

Pressure measurements conducted in small test tanks (less than 1 m^3 volume) in the laboratory yielded no clear results as to the nature of the pressure pulse produced by the plasma jet discharge. The pressure measurements were confused by the many nearby reflecting surfaces of the small tank environment. To overcome the problem of the reflections, the device was set up on a pier at the Royal Victoria Yacht Club. An Atlantic Research LC-10 hydrophone (sensitivity 25,000 Pa/V, 0 to 30 kHz) was deployed on an adjacent pier at a distance of 11 m. The plasma jet and the hydrophone were immersed 1 m in water of depth of approximately 5 m. Figure 2.6 is a copy of an oscillogram recorded by the Tektronics 7D20 digitizing oscilloscope of the pressure pulse received by the hydrophone.

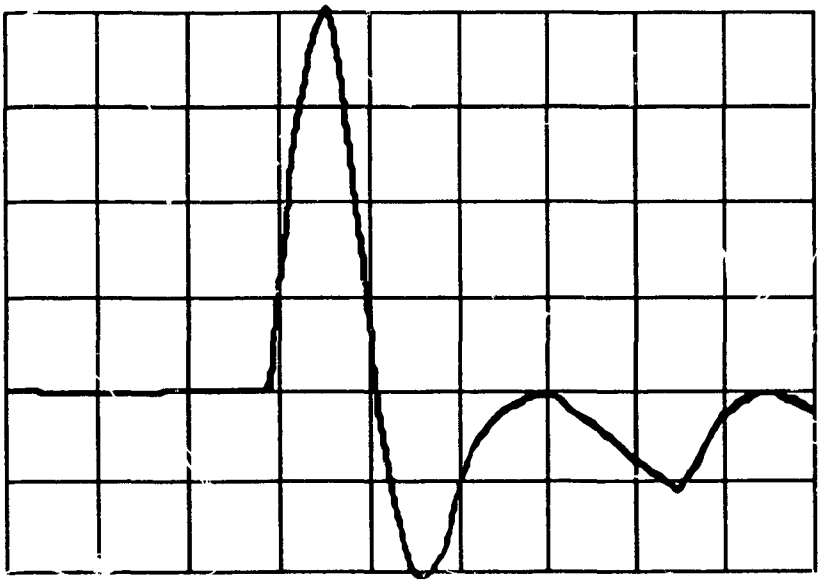

Figure 2.6: Received acoustic signal from 30 J stored electrical energy plasma jet. Horizontal scale: 100 μs/div, vertical scale 5 mV/div.

At this time in the study of the underwater discharge of the plasma jet (Summer 1986), it was felt that sufficient knowledge had been gained to apply for Canadian and United States patents for the device [see Patents 1988]. In addition, an opportunity arose to take part in a geophysical research cruise sponsored by the Pacific Geosciences Centre of Sidney, B.C. aboard the *CSS Parizeau*.

2.2 The seagoing device.

For the cruise aboard the *Parizeau* the device was completely redesigned to allow it to be deployed from the large ship and to be self-contained electrically. It stored 150 J of electric energy and could be charged and discharged twice per minute. A further constraint, because of time considerations, was that the device be fabricated from off-the-shelf materials. Figure 2.7 shows the essentials of the newly evolved system the plasma gun.

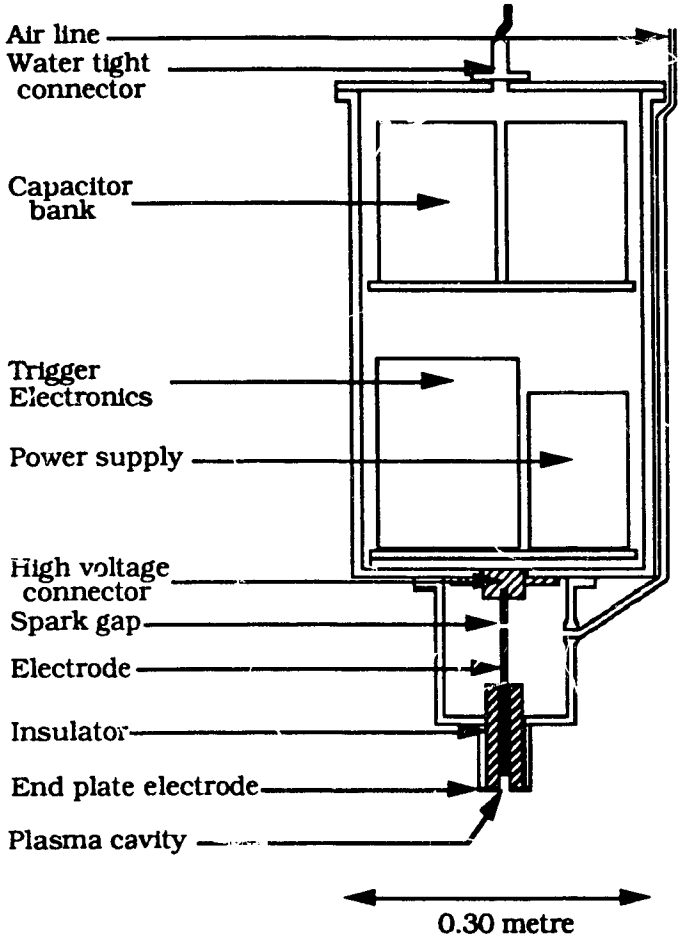

Figure 2.7: Cross-section of the plasma gun.

2.3 Single waveform pressure signatures.

During the *Parizeau* cruise pressure waveforms were measured in both the near and far field environments. (A discussion of the near field and far field is given in Appendix A). Figure 2.8 shows the pressure traces measured at three water depths: 15, 1.5, and 0.3 m. At 15 m, the pressure signature is that in the near field (no surface reflection), at depth 0.3 m is that in the far field (strong surface reflection), and at 1.5 m it is between the near and far fields . There is evidence of a bubble pulse on the near field pressure signature (15 m depth) at approximately 5 ms. The other signatures taken at lesser depths (hence pressure) probably would not have shown a bubble pulse

on this time scale. Acoustic pressure signatures were detected with a single EDO Model 6194 hydrophone with a 0-50 kHz passband using a 100x preamplifier and recorded using a digitizing oscilloscope in conjunction with a PDP 1120 computer.

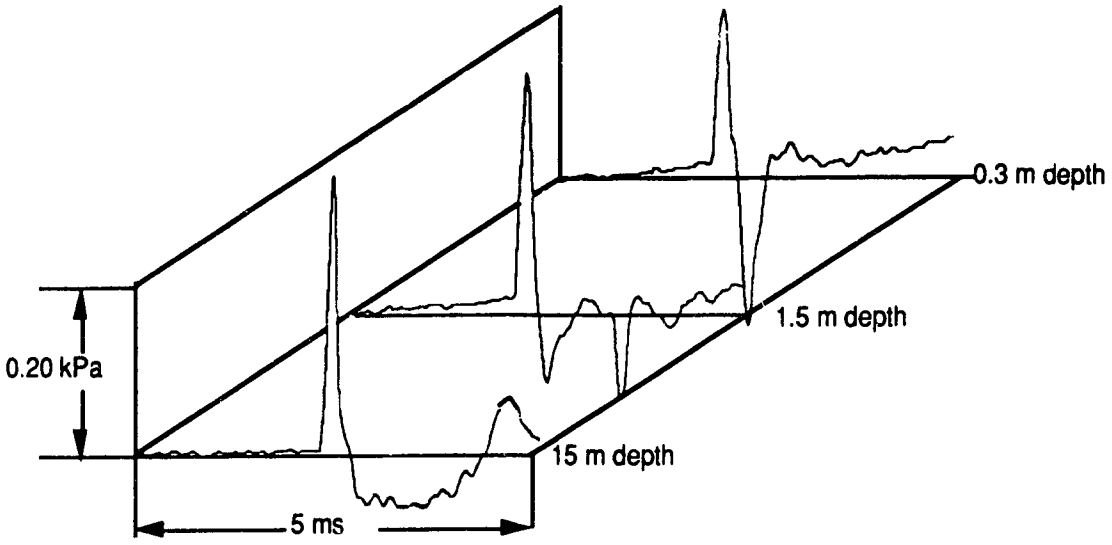

Figure 2.8: Near, intermediate, and far field pressure signatures of the plasma gun.

The primary acoustic source device aboard for the *Parizeau* cruise was a Bolt PAR® 1 cubic inch (1.6×10^{-5} m^3) air gun. Figure 2.9 shows the pressure signatures of both the air gun and the plasma gun under similar conditions. Both acoustic signatures were detected with the same system as that of Figure 2.8. The hydrophone was located 24 m below the surface directly under the source. To suppress the bubble pulse both devices were immersed to a depth of approximately 0.3 m. Note the absence of the pressure precursors in the plasma gun. In the air gun these precursors are caused by the valve mechanisms that vent the high pressure air into the water. The electrical energy stored in the capacitors of the plasma gun was approximately 150 J and the energy stored in the air gun is calculated to be 700 J, assuming an average between adiabatic and isothermal

expansions. Previous measurements on plasma jets in air [Smy et al. 1983], show the amount of energy deposited as thermal energy in the cavity that subsequently heat and expands the gas is 8-10% of the stored electrical energy or approximately 12-15 J for the plasma source. The energy available to the air gun chamber is therefore nearly 50 times greater than that available to the plasma gun cavity.

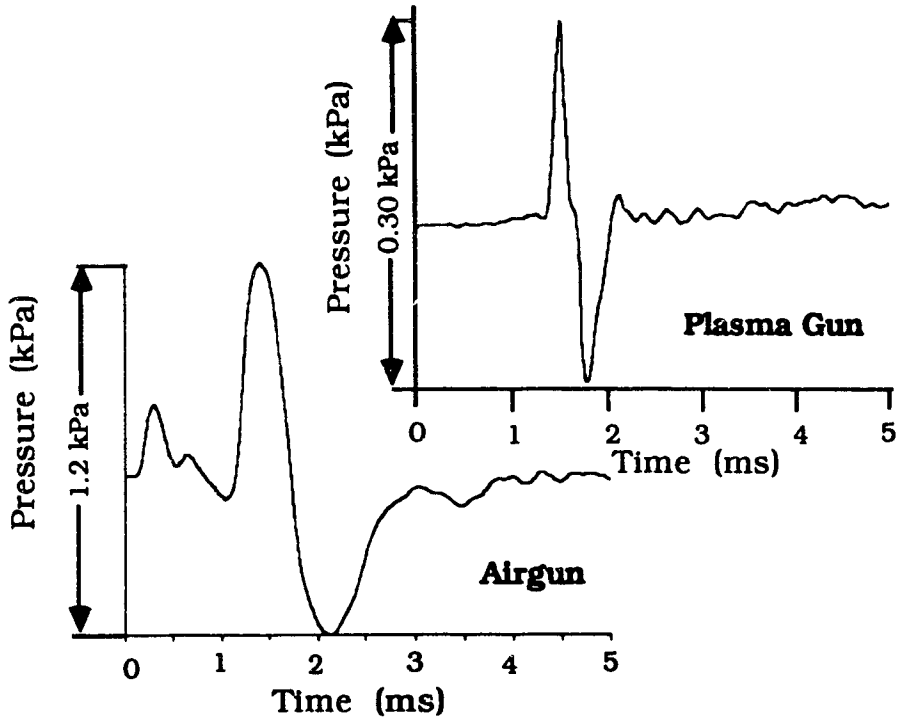

Figure 2.9: Pressure signatures of air gun and plasma gun at immersion depths of 0.3 m.

More details of these experiments, particularly as related to seismic profiling are found in Pitt et al. [1988]. After the preliminary experiments were completed, it was deemed necessary to determine the fundamental physics of the device. The effects of cavity volumes, cavity airflow rates, and the effects of electrical circuit parameters on the pressure signature were measured using single hydrophones in both the near and far fields (including the surface reflection) and studied in detail.

CHAPTER 3

Detailed single hydrophone measurements

3.1 Pressure measurements in large volume environments.

The first method to measure the pressure pulse from the plasma gun in the near field was to sling the device with ropes and to deploy it from the dock at the Institute of Ocean Sciences in Sidney, British Columbia. The weight of the device, inability to maintain proper orientation, and the combined effects of tides and bottom reflections all combined to produce results that were less than satisfactory. Next a 2.5 m long metal tube bent at a right angle near the end was fashioned to fit the end of the plasma gun. Lowered into the water approximately two metres, the right angle bend allowed the horizontal orientation of the cavity end of the device to be directed toward the receiving hydrophone. Although the results obtained were superior to the previous attempts, confusion of the pressure pulse by bottom and surface reflections continued to be a problem. Maintaining the plasma gun and the hydrophone at the same depth was also difficult.

If the plasma gun could be shown to be omnidirectional, or nearly so, problems involving the orientation of the plasma gun and the hydrophone could be simplified a great deal. The directivity of the plasma gun was measured in the acoustic test tank (2.4 m diameter and 2.4 m height) at the Institute of Ocean Sciences. Another plasma gun similar to that shown in Figure 2.1 but fabricated of metal to lessen electrical interference was positioned at the geometric center

of the tank. Two EDO 6166 calibrated hydrophones (-207 ± 2 dB re 1V/μPa, 0 to 100 kHz), one fixed at a known distance from center, the other movable both in the radial and polar directions were deployed in the same horizontal plane as the plasma gun. Circuit parameters for the experiment were C = 300 μF, L = 51 μH, V= 800 V, stored energy 96 J. Because there is some shot to shot variation in the pressure signature of the plasma gun, the ratio of the maximum pressure of the movable hydrophone to the maximum pressure of the fixed hydrophone was used to monitor any abnormal pressure signatures during the measurement. Sound pressure levels (SPL = 20 log P/P_0, P_0 = 1 μPa) were then calculated using eight averaged pressure values for each position. The positions of the receiving hydrophones were arranged so wall, bottom, and surface reflections did not confuse the the primary pressure pulse until well after the maximum pressure was reached. Measurements were made in the polar direction from -10° through 190°, 0° being straight in front of the plasma gun. Symmetry of the plasma gun structure about the 0--180° axis allowed pressure values from 190° to 360° to be assumed from this symmetry. Figure 3.1 shows the results of the pressure measurements when the movable hydrophone was at a distance of 0.711 m from the plasma gun tip. Figure 3.2 shows the results of a similar set of measurements with the movable hydrophone at a distance of 0.356 m from the plasma gun. Note the significant notch in the pressure pattern directly behind the body of the plasma gun device, caused by the plasma gun structure shadow. At the larger distance the notch is not apparent.

Figures 3.1 and 3.2 show that the device is nearly omnidirectional at least at distances greater than 0.711 m. It was now possible to

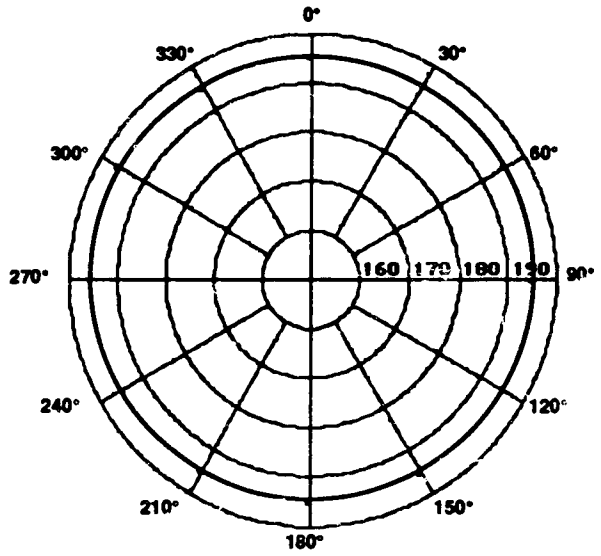

Figure 3.1: Polar plot of sound pressure level (dB re 1μPa at 1 m) measured at 0.711m.

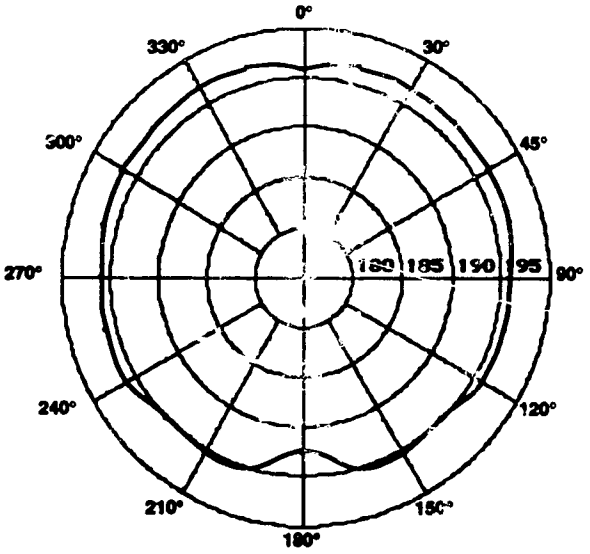

Figure 3.2: Polar plot of sound pressure level (dB re 1μPa at 1 m) measured at 0.356 m.

measure the pressure signature of the plasma gun without knowing the exact position of the receiving hydrophone, as long as it was at a reasonable distance from the source. The actual distance could be determined from the oscilloscope trace by measuring the time between the firing signal and the arrival of the acoustic signal.

In Haro Strait a series of open ocean experiments in water deep enough (25 m) to prevent bottom reflections interfering with results were undertaken using a plasma gun similar to Figure 2.7. Here both near and far field pressure signatures were measured which allowed peak pressures, total radiated acoustic energy, and efficiency to be ascertained. Plasma gun, coaxial, and parallel sparker pressure signatures were measured and compared (these sparker designs are used in China by the Beijing Electrical Engineering Institute [Sun 1988j). Dimensions of the parallel and coaxial sparker electrodes are shown in Figure 3.3. The sparker electrodes were designed to replace the plasma gun electrodes directly so the same power supply and electronics system could be used for all three devices.

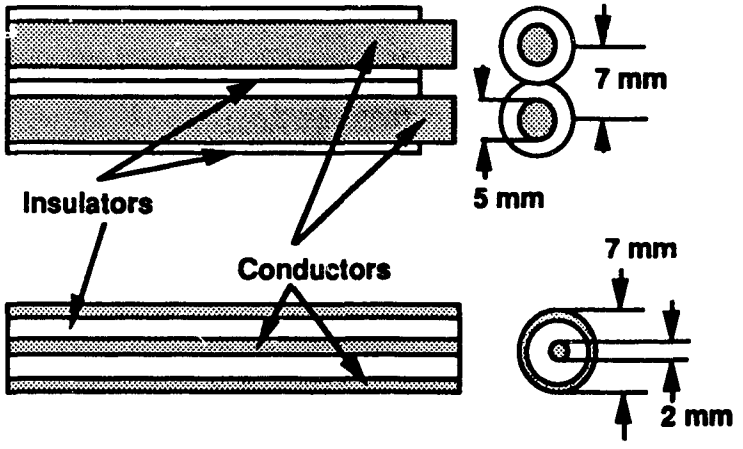

Figure 3.3: Parallel and coaxial sparker electrodes.

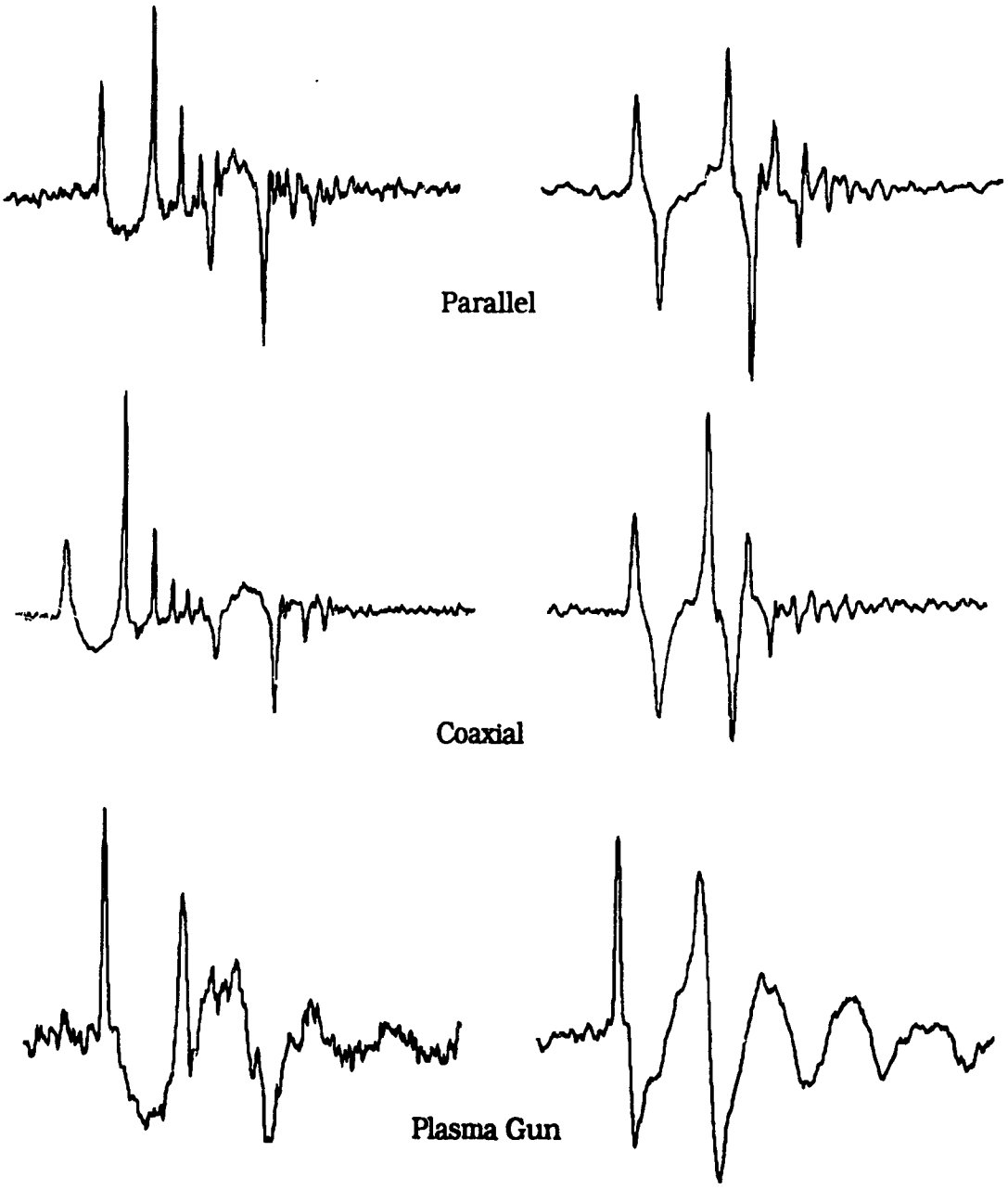

Figure 3.4: Pressure signatures of sparkers, and plasma gun. Near (left) and far field (right), each trace is 20 ms long.

Figure 3.4 shows pressure signatures measured from parallel and coaxial sparkers, and a plasma gun obtained in the near and the far field. These pressure signals were collected using a Tektronic 7D20 digital oscilloscope and recorded on a PDP 1120 computer. The deployment scheme for the near and far field signatures are shown in Figure 3.5. In both cases the depth of the hydrophone was approximately ten metres.

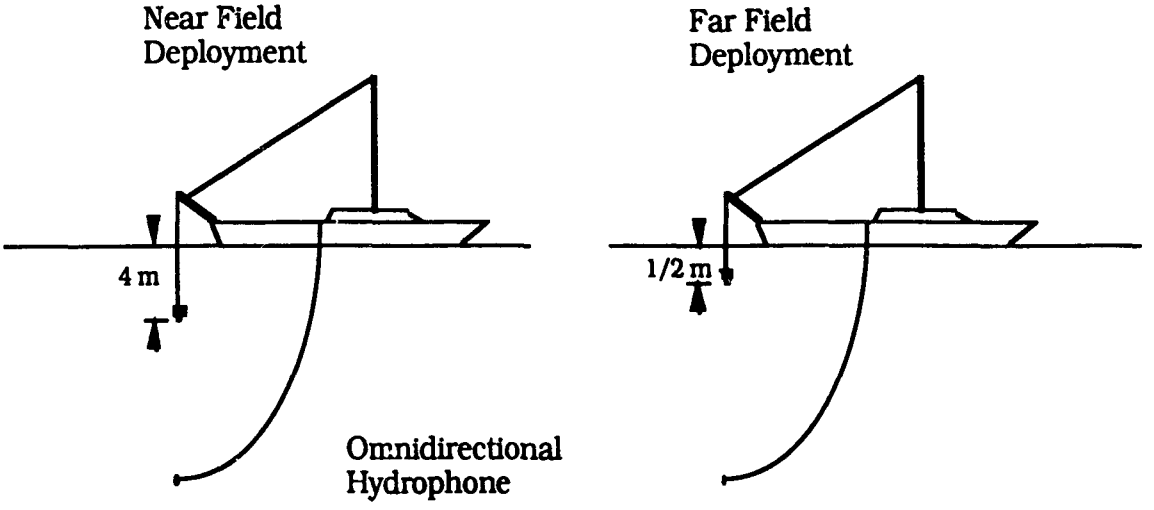

Figure 3.5: Deployment scheme for near and far field pressure signatures.

3.2 Pressure measurements in limited volume environments.

With the completion of measurements in the open ocean, enough experience and confidence in separating reflections from primary signals allowed an extensive series of data gathering in the laboratory to begin. A 2.4 m diameter by 2.4 m high acoustic tank was constructed in the Plasma Physics laboratory to allow near field pressure signature measurement (design criteria for the tank followed those given by Levin [1974]). The same data collection system as used aboard the *Sabrina* was used for these experiments. Experiments

were designed to determine the effects of cavity diameter, cavity length, air flow, stored energy, current discharge time, and peak current upon various portions of the pressure signatures.

3.2.1a. Cavity size experiments.

To determine the extent to which the plasma gun could be tuned by altering the size of the plasma cavity, the primary pulse width (the time that the positive going pressure pulse is greater than ambient pressure), the bubble pulse period, and the maximum pressure was determined for four different cavity diameters and seven cavity lengths between 4 and 10 mm. These parameters are detailed Figure 3.6, a sketch of a typical plasma gun pressure signature. The range of cavity dimensions was dictated by the criterion of reliable discharges (shorter or longer lengths and larger diameters result in inconsistent firing). A calibrated hydrophone placed 130 mm directly ahead of the plasma gun cavity end was used to measure the pressure signatures. Eight discharges were collected and averaged for each data point. The results for the cases of 96 J of stored energy (circuit component values: C = 300 μF, L = 51 μH, Voltage 800 V) are shown in Figures 3.7 a, b, c, and d.

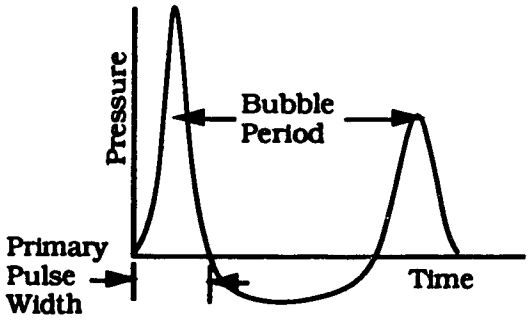

Figure 3.6: Plasma Gun pressure signature.

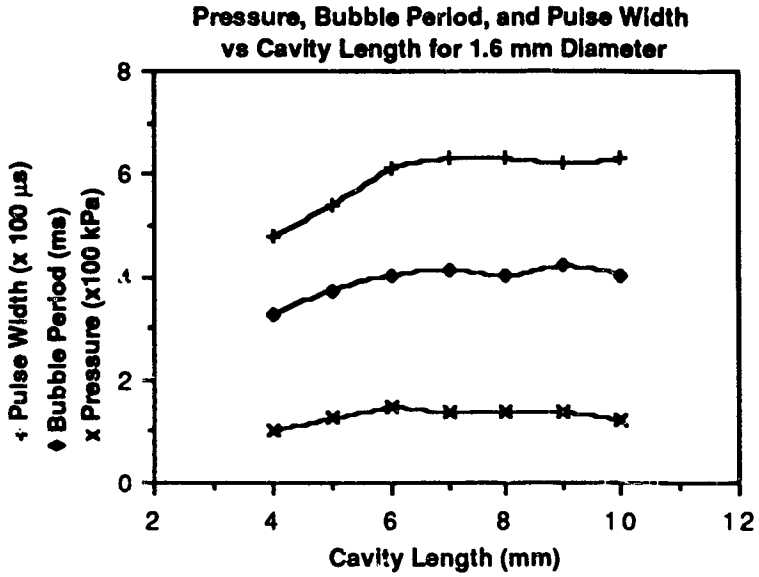

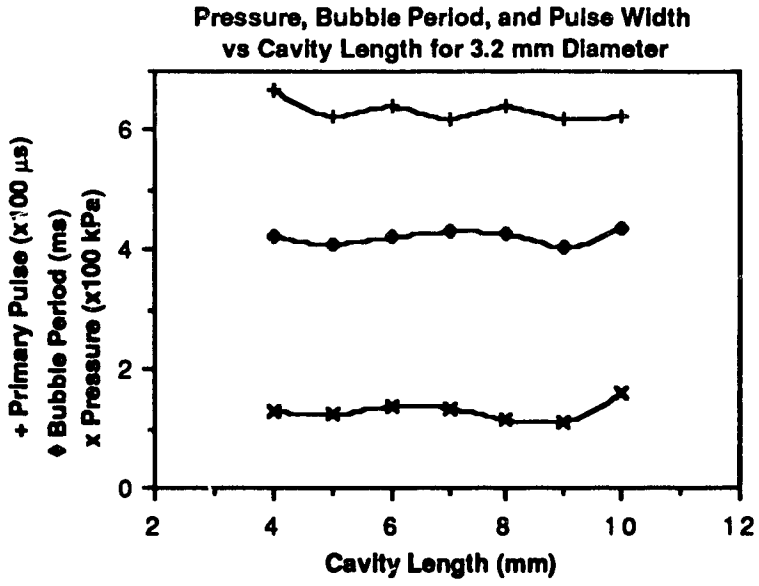

Figures 3.7a and b: Effect of cavity size on pressure parameters.

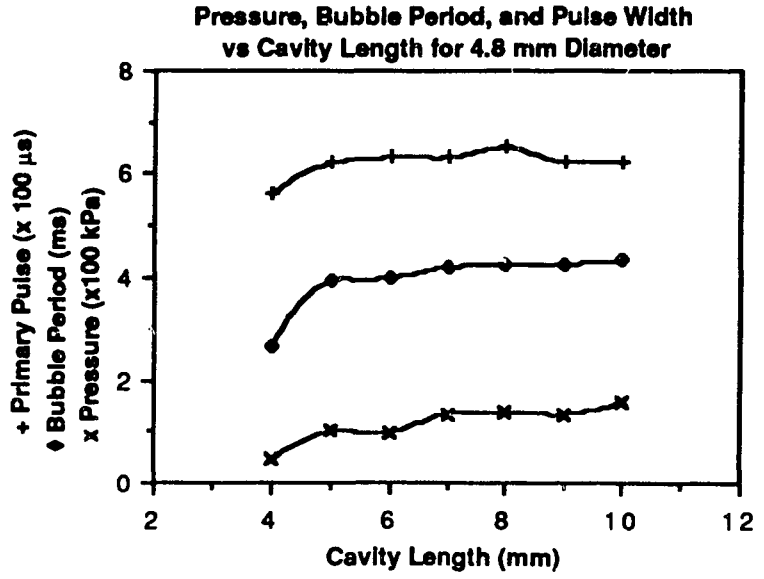

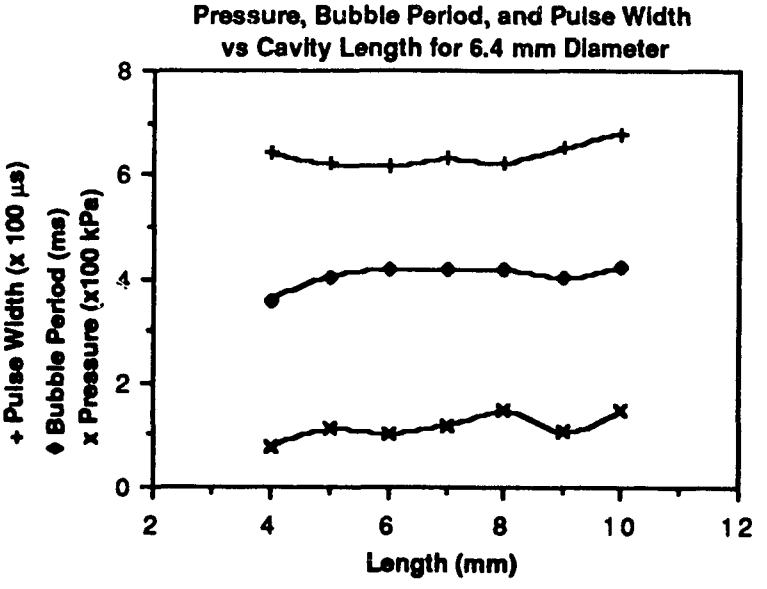

Figure 3.7c and d: Effect of cavity size on pressure parameters.

3.2.1b. Results of cavity size on pressure parameters.

The experimental data show the cavity dimensions have very little effect upon the pressure parameters. Peak pressure, which seems to be most affected by cavity length does not appear to be dependent on the cavity diameter. The primary pulse width remains almost constant throughout all dimensional variations. Similar experiments for voltages of 600 and 1000 volts for the same cavity sizes also showed little effect on the pressure parameters.

3.2.2. Air flowrate effects on peak pressure.

The effects of air flow on the peak pressure produced by the plasma gun were determined by measuring flows with a standard rotometer which was calibrated by capturing the air passing through the plasma cavity in a large graduated cylinder. A 3.2 mm diameter by 8 mm length cavity, capacitance 300 μF, and inductance 51 μH was maintained throughout the experiment. Results of the study for three values of capacitor voltage are shown in Figure 3.8. Results show that

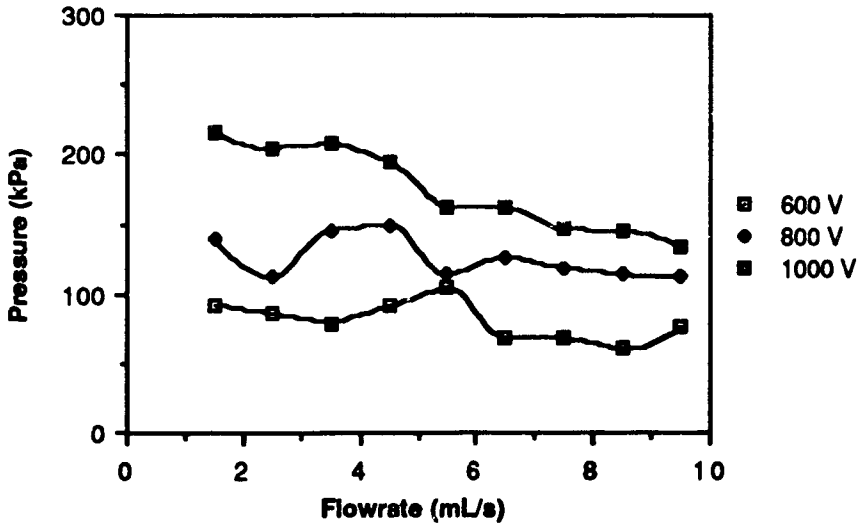

Figure 3.8: Effects of airflow on peak pressure.

maximum pressure produced by the plasma gun is achieved when the airflow is maintained at a minimum value. Air flows less than 1 mL/s result in inconsistent operation. The effect of air flow on pressure is not a strong function. The probable effect of increasing airflow is due primarily to the poor acoustic coupling of the discharge into aerated water [Albers 1965] and secondarily to changing the effective cavity size because larger air bubbles are produced at the cavity exit. The deviations from a straight line trend are likely a measure of the experimental error.

Helium gas instead of air was tested in the plasma gun with no significant differences noted.

3.2.3. The effect of stored electrical energy on bubble pulse period.

Underwater explosions have been studied in great detail by many experimentalists. Cole [1948] found the bubble period to be proportional to the one third power of the weight of the explosive. Assuming the explosive energy to be proportional to its weight, the bubble period would then also be proportional to the cube root of the explosive energy. Using differing capacitances, voltages, and inductances, many experiments were conducted studying discharges of stored energy between a few Joules and many hundreds of Joules. Figure 3.9 shows that the bubble period produced by the plasma gun and the cube root of the stored energy are in a linear relationship (similar to explosives). Each data point represents an average of eight individual measurements.

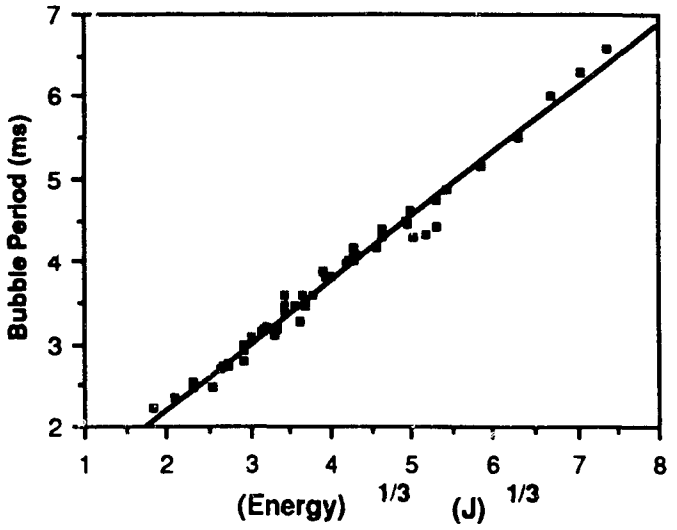

Figure 3.9: Bubble period versus cube root of stored energy.

3.2.4 Circuit inductance and capacitance effects on the primary pulse shape.

3.2.4 a. The effect of maximum current on peak pressure.

The effect of the maximum current in the discharge circuit upon the peak acoustic pressure was studied for a variety of charging voltages and capacitances. All of the experiments were conducted with a cavity diameter of 3.2 mm and length between 6 and 8 mm and a circuit inductance of either 13 or 51 μH. Results are shown in Figure 3.10. A polynomial fit to the data of Figure 3.10 by a standard graphics package yielded a best fitting line with a quadratic function. Figure 3.11 shows the same data with the pressure plotted versus the square of the current (without capacitance and inductance differentiation). Since the square of the current would be proportional to the power delivered to the device if the resistance of the arc were constant, the nearly linear relationship between the pressure and the square of the current indicate that even with a variable arc resistance the peak pressure depends on an average power delivered to the arc.

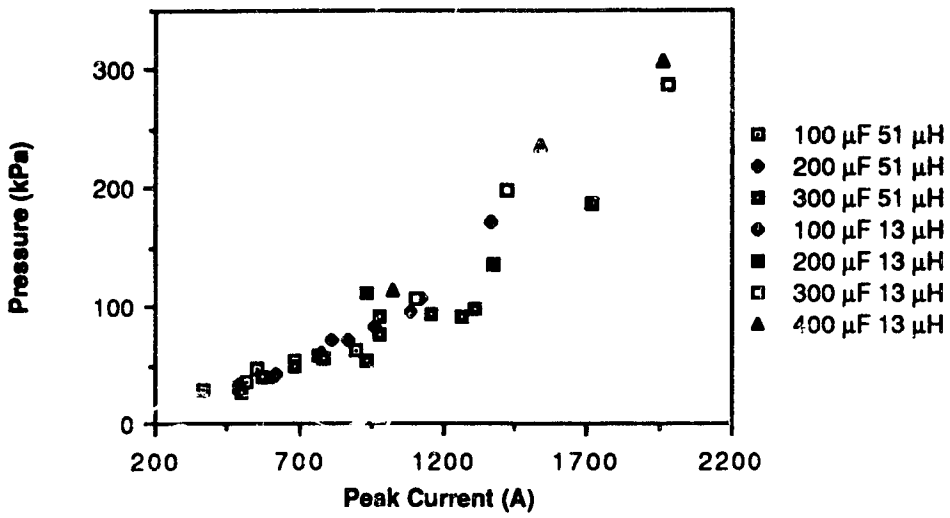

Figure 3.10: Acoustic pressure versus discharge current.

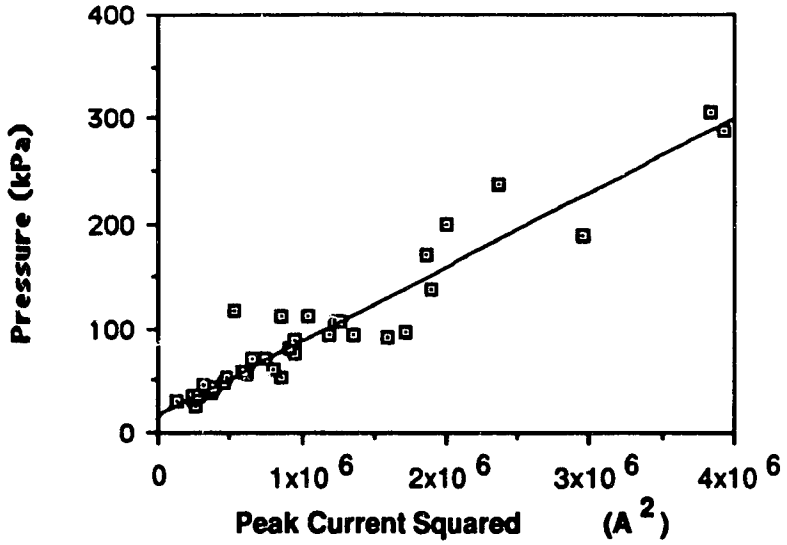

Figure 3.11: Acoustic pressure versus discharge current squared.

The electrical circuit of the plasma gun is essentially a series RLC circuit (see Figure 2.2) with a resistance that changes during the arc discharge. Because the values of the circuit parameters used in the plasma gun are near the conditions that result in critical damping, i.e. a circuit taking the longest time to decay to zero, slight changes in resistance can produce either an overdamped or underdamped discharge. Usually, the system behaves as an overdamped circuit, but occasionally an underdamped oscillation occurs. When it occurs, the underdamped discharge commonly only oscillates for one-half cycle, because the voltage across the arc is insufficient during the negative part of the first half-cycle to maintain the discharge: the arc is extinguished.

Both the distributed capacitance and inductance in the circuitry and transmission lines of the plasma gun's series RLC circuit are small compared to the storage capacitance and the blocking inductor. The two series arcs--the plasma cavity arc and secondary spark gap arc, (see Figure 2.2)--fix the resistance. Thus the storage capacitance and the blocking inductance can be altered somewhat to affect the current shape and thence the primary pressure signature.

Studies involving similar electrical systems used with underwater sparker sources [Caulfield 1962] have shown that particularly at the leading edge the pressure signature follows the shape of the electrical current pulse producing the underwater arc. Although the plasma gun arc is initially established in a gaseous environment while the sparker arc is in a liquid environment, enough similarities exist between the two systems--particularly later in the discharge--to warrant a study of how the primary pressure signature is influenced by the shape of current discharge.

Current in a series RLC circuit in both the overdamped and underdamped discharges is [Davie 1964]

$$I = \frac{V}{\omega L} e^{-\frac{Rt}{2L}} \sinh \omega t \qquad (3.1)$$

Equation (3.1) is valid only if care is taken about the real and imaginary nature of the frequency, ω, and the identity $\sinh(i\omega t) = i \sin(\omega t)$ is used, where

$i = \sqrt{-1}$

I = Current, V = initial capacitor voltage

R = Average total resistance

L = Total Inductance

$$\omega = \frac{1}{2L}\left(\frac{4L}{C} - R^2\right)^{\frac{1}{2}}$$

C = Total capacitance

t = time

The capacitance and the inductance both influence the shape of the current pulse.

Experimentation with the circuit parameters confirm capacitance and inductance have strong effects on both the amplitude and duration of the current pulse. Figure 3.12 shows the results of several measurements of peak current versus voltage for several values of capacitance and inductance. Changing the inductance is a more convenient method to alter the peak current because the total energy stored is not altered when the inductance is changed.

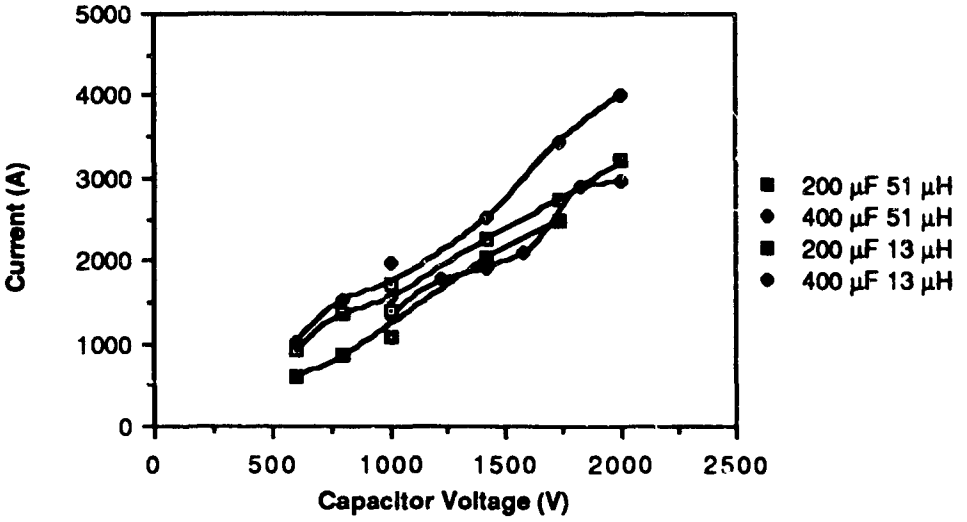

Figure 3.12: Peak current versus capacitor voltage.

3.2.4 b. Capacitance and inductance effects on primary pressure pulse width.

The frequency of an RLC circuit is controlled by its resistance, inductance and capacitance. If the primary pressure pulse width can be influenced by the discharge current shape, the most dramatic effect would be by controlling the current period. In general the period of an RLC circuit is given by

$$T = 2\pi \left(\frac{4L^2C}{4L - R^2C} \right)^{1/2} \qquad (3.2)$$

Analysis of (3.2) shows that for fixed resistance the inductance is more important than the capacitance in determining the period. Values of inductance (tens of microhenrys), capacitance (hundreds of microfarads) and arc resistance (several tenths of an ohm) in a typical plasma gun result in a circuit close to the boundary of

underdamped and damped oscillation [Scott 1959]. Figure 3.13 shows the effect of capacitance upon the primary pressure pulse width with constant inductance of 13 and 51 μH. The values shown are averages for several voltages. Standard deviation from the averages was a maximum of six percent. The results show that some reduction in the primary pulse width can be attained by decreasing either the capacitance or the inductance of the circuit. Changing the value of the inductance does not alter the stored energy in the circuit ($1/2\ CV^2$). Again it may be desirable to alter the primary pulse width without affecting the bubble period of the pressure signature. In general the bubble period is responsible for one of the dominant frequencies of the pressure signature.

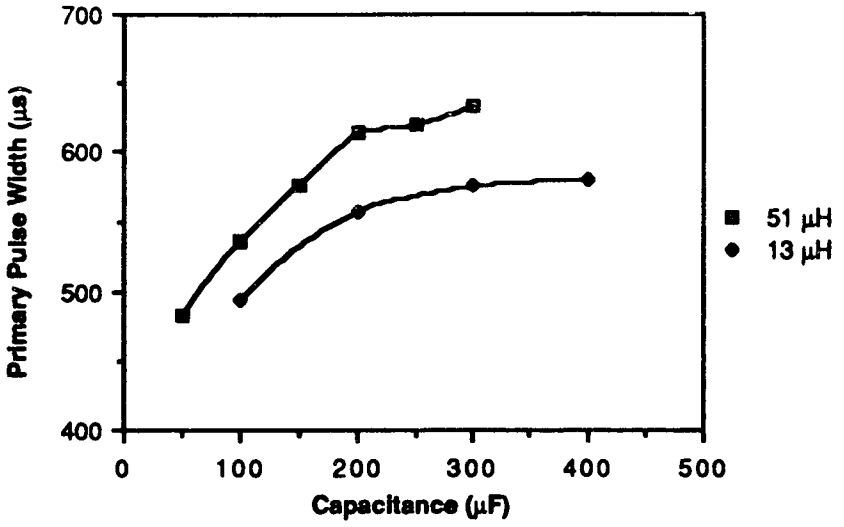

Figure 3.13: Pulse width versus capacitance.

Decreasing either the capacitance or inductance to values low enough to force the circuit into underdamped oscillation beyond the first half cycle complicates the pressure signature. Restriking of the arc creates a series of smaller pressure pulses superposed upon the trailing edge of the primary pressure pulse. This makes pressure

conditions undesirable for use as an acoustic source.

Neither capacitance nor inductance values change the trailing edge of the primary pulse contour significantly. Its shape resembles an exponential decay probably because of transfer of heat energy to the surrounding water.

3.2.5 Results of circuit parameters on the acoustic pressure signature.

The experimental data dealing with the circuit parameters are summarized as follows:

1. ***The peak pressure.*** The peak pressure of the primary acoustic pulse depends upon the square of the peak current. Current amplitude can be altered by either increasing the capacitance, decreasing inductance, or by increasing voltage. For constant energy the most efficient method is to decrease inductance.
2. ***The width of the primary acoustic pulse.*** This depends most strongly on the circuit inductance but it is also influenced by the capacitance. The leading edge of the acoustic pulse follows the rise time of the current pulse reasonably closely. Rise times of the current pulse can be controlled quite effectively by varying the inductance of the circuit, particularly if constant energy and hence constant bubble period is desired. The trailing edge appears to be related to the cooling by the surrounding water of the gases within the bubble.

Chapter 4

Frequency and Energy Measurements

4.1 Acoustic spectral analyses.

Because the Society of Exploration Geophysicists [Johnston et al. 1988] recommends that the surface reflection be included in the measurement of pressure signatures, measurements at sea should allow the best opportunity to measure the far field signature (which includes the surface reflection). The technical problems in maintaining a constant immersion depth from a small boat, particularly in moderate seas, made these measurements extremely difficult. Immersion depth uniquely determines the amount of time after the beginning of the pressure pulse that the reflected pulse begins to combine to produce the outgoing far-field pressure signature. Because this amount of time affects the pressure waveform so strongly, the frequency domain of the pressure signature is also heavily affected.

To separate circuit parameter changes from those of source motion as they affect the pressure signature and to maintain conditions as similar as possible between pressure measurements using different electrical circuit values, it was decided to measure the pressure signature in the near field where more control could be exercised. The data from these measurements could then be processed to simulate the proper timing of the surface reflection. Most measurements were carried out in the acoustic testing tank

(dimensions 2.4 m in diameter and 2.4 m in height) in the Plasma Physics laboratory. The plasma gun was placed in the geometric center of the tank and the measuring hydrophone was placed 0.13 m directly ahead of the cavity orifice. These dimensions result in surface and wall reflections that are reduced by spherical spreading to about six percent in amplitude at the hydrophone location and a two way reflection time of approximately 1.5 ms. It was felt that this experimental design would avoid the many uncertainties that might be encountered aboard ship.

Previous measurements (see Chapter 3) have shown that the bubble period is at best only slightly affected by the electrical circuit parameters because it is only dependent on the total energy deposited in the water. Energy deposited into the water was determined by calculating the potential energy, (p_0V), of the maximum sized bubble, (from the video images), produced by the plasma gun discharge , [Lamb 1945].

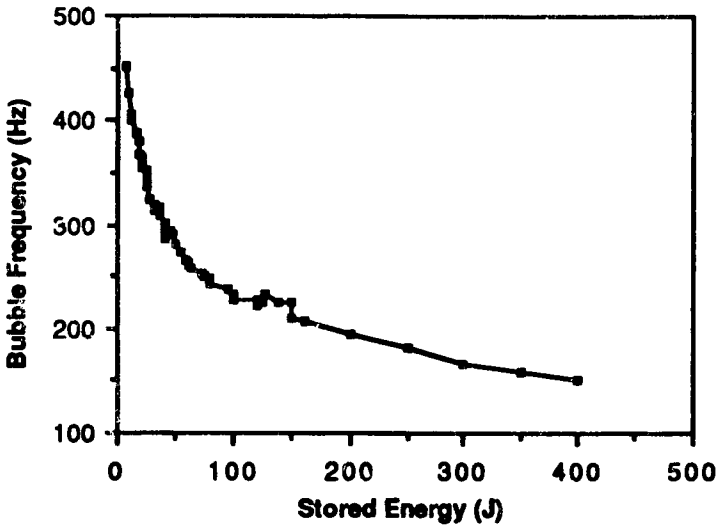

Figure 4.1: Bubble frequency versus stored energy.
(the anomoly between 125 and 150 J
is due to depth uncertainties)

Experimentally it is approximately 4% of the total stored electrical energy. Figure 4.1 is the result of bubble period measurements versus stored electrical energy for a large number of varying circuit parameters and deployment schemes in both laboratory and under conditions at sea. The bubble frequency is defined as 1/(bubble period), $(1/T_B)$, (see Figure 3.6).

The frequencies that result from changes in the electrical circuit components of the plasma gun will essentially only affect the primary pulse and its reflection. Pressure was measured with an EDO 6166 hydrophone having sensitivity of -207 ± 2 dB re 1 V/μPa between 0 to 100 kHz. Data was collected with a Tektronics 7D20 digital oscilloscope, and recorded on an Atari 1060 or PDP 1120 computer. Waveform processing was done with a Tektronics 7854 digital oscilloscope with waveform calculator. Frequency analysis was performed using a fast Fourier transform based power spectra package using either of the two computers. The power spectrum program derived a 512 point power spectrum from a 1024 point pressure signature captured by the oscilloscopes.

In order to obtain the surface reflected pressure pulse, the negative of the primary pressure pulse, displaced 500 μs (the return time to the surface from the plasma gun at a depth of 0.375 m) was added to the primary pulse. This approximates the depths used in the preliminary seismic surveys.

Only the pressure information of the primary pulse and its reflection was processed by the power spectrum program. Figure 4.2 shows the simulated pressure signatures that result for discharges of the highest circuit frequency, f_{max} = 3,680 Hz, and the lowest circuit frequency, f_{min} = 1600 Hz (a ratio of frequencies of 2.3). Frequencies were measured from current discharge times. Circuit parameters are included in Figures 4.2. Figure 4.3 shows the corresponding power spectra.

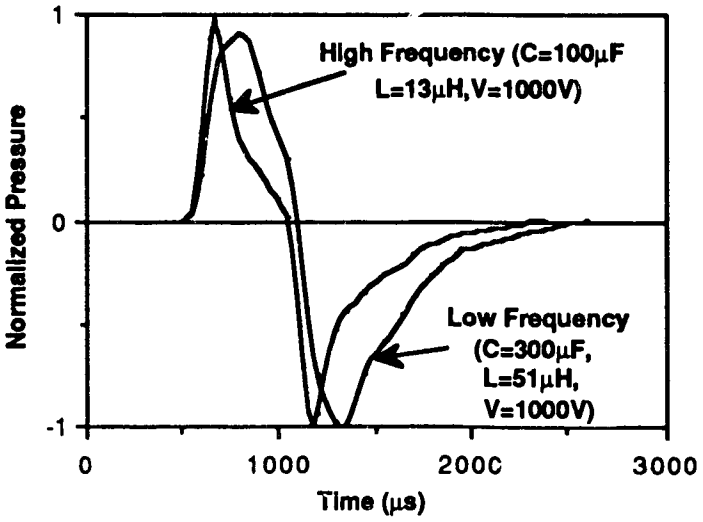

Figure 4.2: Normalized pressure versus time for low and high frequency discharges.

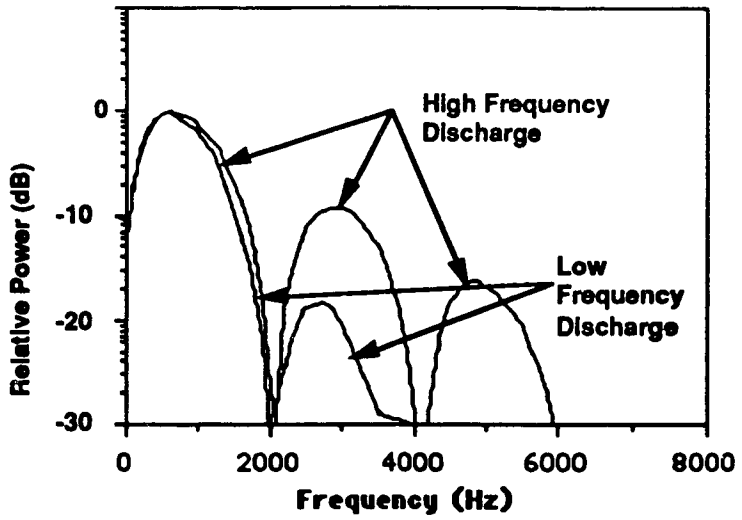

Figure 4.3: Power spectra for low and high frequency discharges.

It is clear from Figure 4.3 that the circuit parameters do affect the power spectra. Some energy is moved into higher frequencies by the higher frequency circuit. The minimums at even multiples of 1000 Hz are the result of destructive interference effects from reflection at the effective surface distance of 0.375 m from the

source.

Figure 4.4 is a far field pressure signature synthesized from near field measurements made at the Institute of Ocean Sciences dock. Figure 4.5 is the corresponding power spectra. Because this was a more open environment producing limited reflections, both the primary pressure pulse and the bubble pulse could be convolved to produce the far field signature equivalent to a reflection time of the same 500 μs (immersion depth 0.375 m). By comparing Figures 4.3 and 4.5 it is seen that the shape of the power spectrum is changed toward lower frequencies by the inclusion of the bubble pulse. Energy and circuit values used in the low frequency signature of Figure 4.2 and Figure 4.4 were identical.

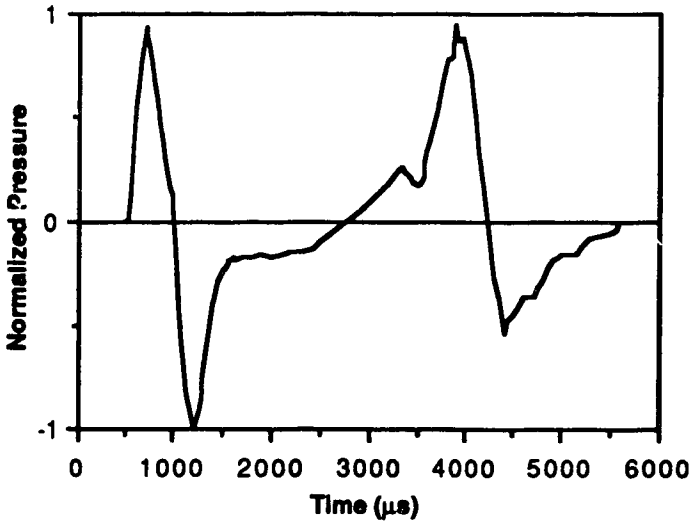

Figure 4.4: Synthesized normalized pressure versus time.

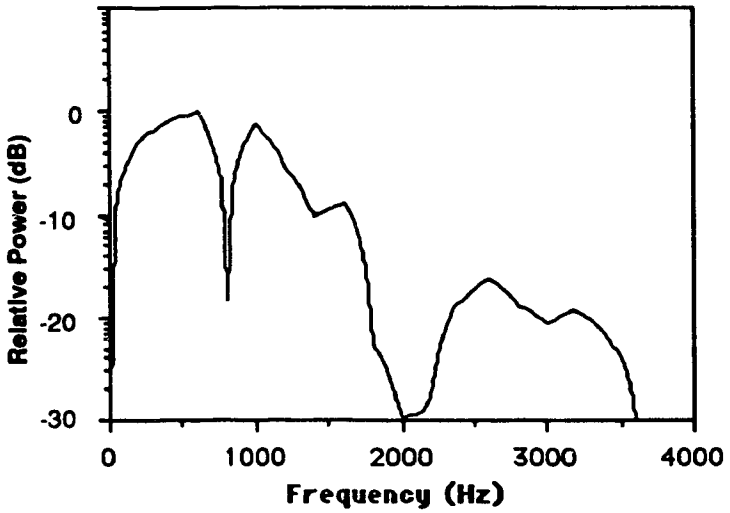

Figure 4.5: Power spectrum including bubble pulse.

Figure 4.6 is a portion of a real far field pressure signature obtained in Haro Strait. The signature was truncated after the bubble pulse. Energies and circuit components are the same as those of Figure 4.4. Effective immersion was different and the bubble pulse is slightly smaller because of higher hydrostatic pressure where the near field signature was measured. Although the bubble pulse of the real signature is broadened somewhat, the shapes of the real signature and the synthetic one are approximately the same. Much of the difference may be caused by reflections on the real trace from the surveying boat or from the survey boat-- to--sea surface. Figure 4.7 is the power spectrum of the signature of Figure 4.6. Here a relatively larger amount of low frequency components make up the power spectrum. The difficulty in interpreting complicated spectra of this type initially led to the development of the near field to far field synthesis techniques.

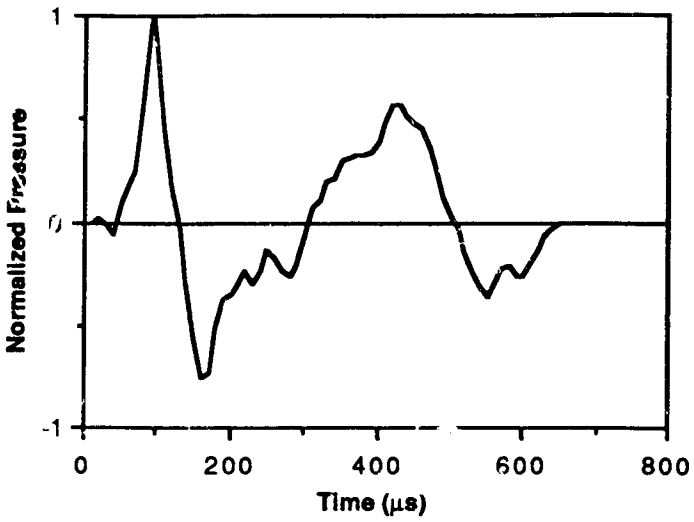

Figure 4.6: Actual far field signature.

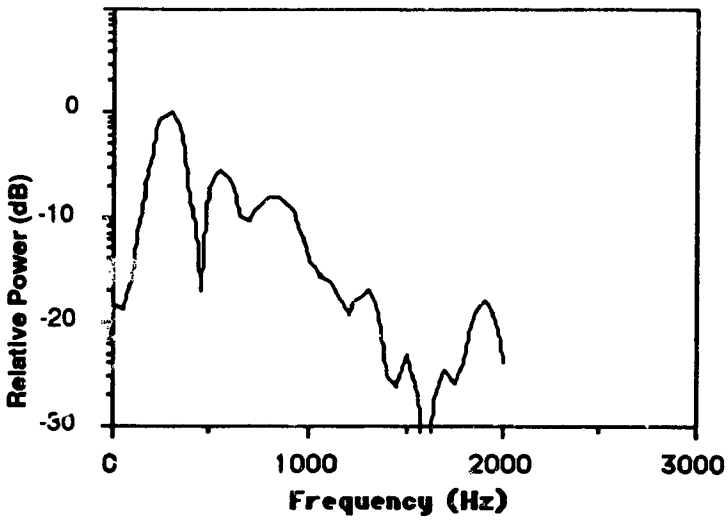

Figure 4.7: Power spectrum of real pressure signature.

A synthetic far field pressure signature using the same near field signature as that of the minimum frequency circuit of Figure 4.2 is shown in Figure 4.8. The difference is that the reflection time was set at 333 μs instead of 500 μs. The power spectrum is shown in Figure 4.9. The previous pressure signature and power spectrum are repeated on both of the latter figures. The difference because of reflection time (167 μs) is equivalent to a depth difference of only 0.125 m.

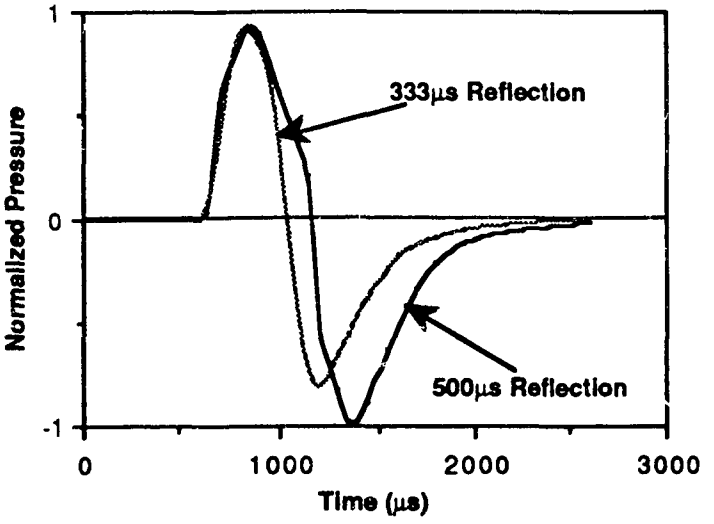

Figure 4.8: Pressure signatures for different reflection times.

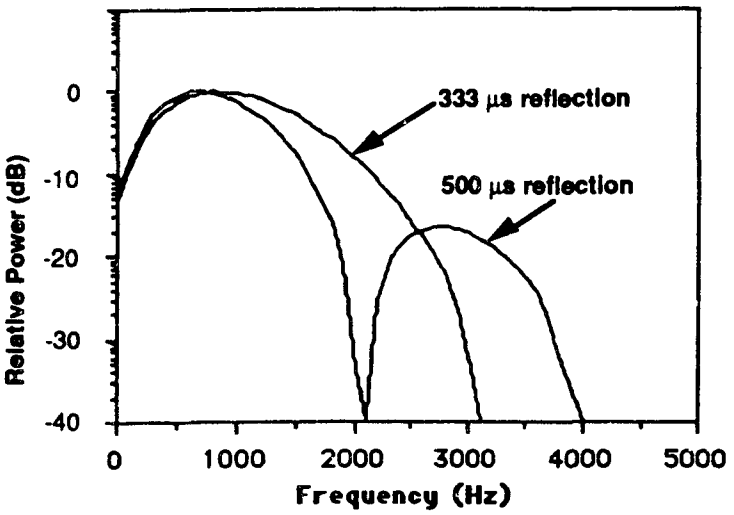

Figure 4.9: Power spectra of pressure signatures with different reflection times.

The immersion depth difference, is particularly significant in the power spectra. A larger portion of energy occurs between 1.2 and 2.4 kHz with less at higher frequencies.

4.1.1 Frequency analyses conclusions and discussion.

The spectral content of the plasma gun can be controlled by three methods:

Electric circuit components. The values of capacitance and inductance determine the frequency and nature of the discharge current. Discharge current frequency and the frequencies contained in the primary pressure shape are not strongly related.

Total stored electrical energy. The bubble frequency depends upon the inverse cube root of the stored electrical energy, i.e. $(1/2\ CV^2)^{-1/3}$. Larger stored energies shift more of the acoustic energy toward lower frequencies. This alters the shape of the acoustic spectrum and produces a larger relative

content of lower frequencies. Higher frequencies produced by the primary pulse shape, however, are not eliminated.

Reflection time. The most effective means of altering acoustic spectra is to adjust the surface reflection time. Surface reflection time, τ, is simply related to the immersion depth of the source by

$$\tau = \frac{2d}{c}$$

where d is the immersion depth and c the velocity of sound in water. The shallower the immersion the higher frequency content of the signal. Note that the reflection time affects both the primary and bubble pressure pulses.

4.2 Energy and efficiency analysis.

A measure commonly used to describe far field signatures is peak-to-peak amplitude between the primary pulse and its reflection, A_1. Another measure is the primary to bubble ratio, A_1/A_2 , [Parkes and Hatton 1986]. Figure 4.10 shows the relationship of these quantities to the pressure signature.

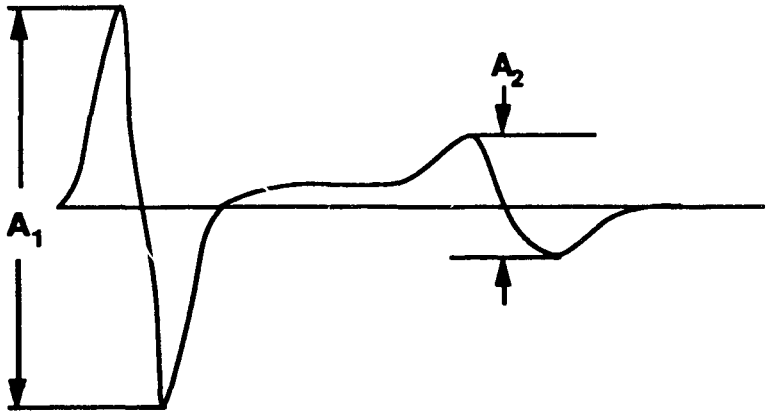

Figure 4.10: Commonly used pressure signature parameters.
A_1; the peak to peak amplitude.
A_1/A_2; the primary to bubble ratio.

Pressure signatures for the plasma gun and for the parallel and co-axial sparkers described in Chapter 3 were measured in the open waters of Haro Strait using the same equipment described in **4.1**. The sparker sources were included for comparison because of the similarity between sparkers and the plasma gun. All signatures used the same electrical parameters: C = 200 μF, L = 51 μH, V = 1800 V giving stored electrical energy of 324 J. The higher voltage (and energy) reported here rather than the 1000 V usually chosen as typical was necessary because the sparker devices did not fire reliably at the lower voltage.

Calculations from the data of the pressure signatures (seen as insets in Figures 4.11, 4.12, and 4.12 below) yield:

Plasma gun: $A_1 = 1.3 \times 10^{10}$ μPa @ 1 m
$A_1/A_2 = 1.48$
SPL = 20 log A_1 = 202 dB re 1 μPa

Parallel sparker: $A_1 = 1.6 \times 10^{10}$ μPa @ 1 m
$A_1/A_2 = 0.60$
SPL = 20 log A_1 = 204 dB re 1 μPa

Coaxial sparker: $A_1 = 1.7 \times 10^{10}$ μPa @ 1 m
$A_1/A_2 = 0.60$
SPL = 20 log A_1 = 204 dB re 1 μPa

(re 1μPa is the pressure value on which the logarithm calculation is referenced)

Similar measurements using lower stored energies within the operational limits of the sparkers show essentially the same relative relationships between the three devices.

The total acoustic energy radiated by the plasma gun and the sparkers was calculated using the same far field pressure signatures described above. Energy was calculated by integration of the

acoustic intensity assuming the spherical isotropy measured in **3.1**. Because the acoustic energy measured is radiated directly from the source and reflected by the sea surface, only the energy flux passing through a hemisphere was calculated from

$$E_A = \frac{2\pi x^2}{\rho_f c} \int_0^t p^2(t)\,dt \qquad (4.1)$$

where E_A is the total energy radiated, x is the distance to the recording hydrophone, ρ_f the density of water, c the speed of sound in water, and p(t) the pressure as a function of time, t. In practice the time base selected on the oscilloscope determines the length of the pressure signature over which integration is performed. Figure 4.11, 4.12, and 4.13 are graphical solutions for each of the three systems of the calculation represented by (4.1).

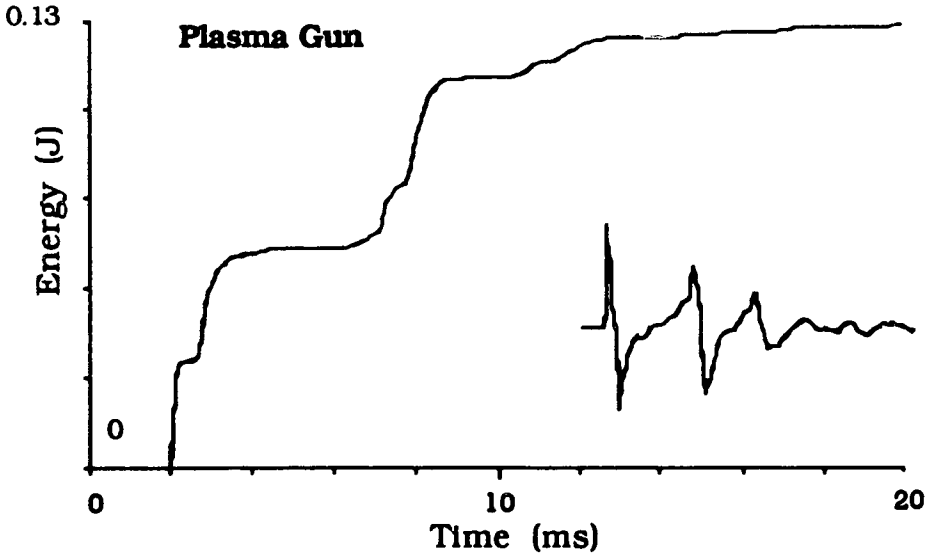

Figure 4.11: Energy versus time for plasma gun.

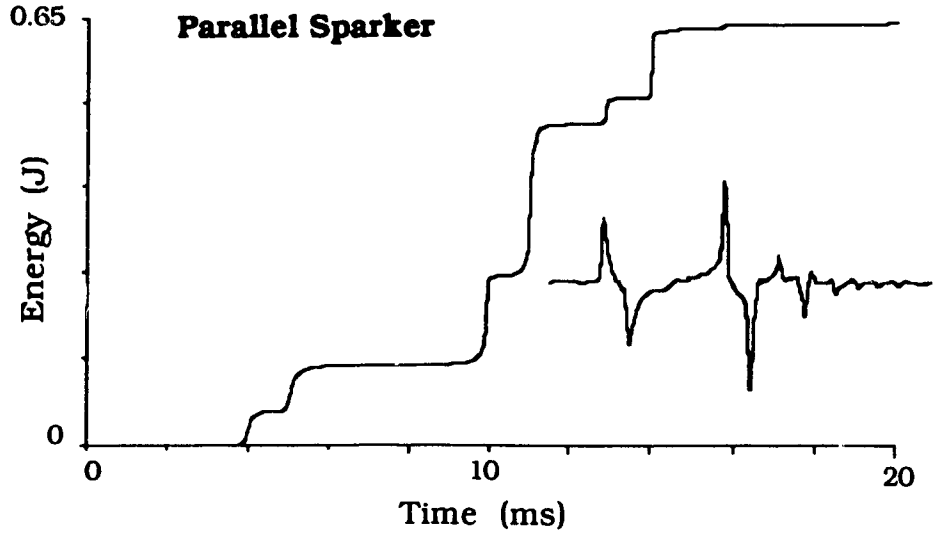

Figure 4.12: Energy versus time for a parallel sparker.

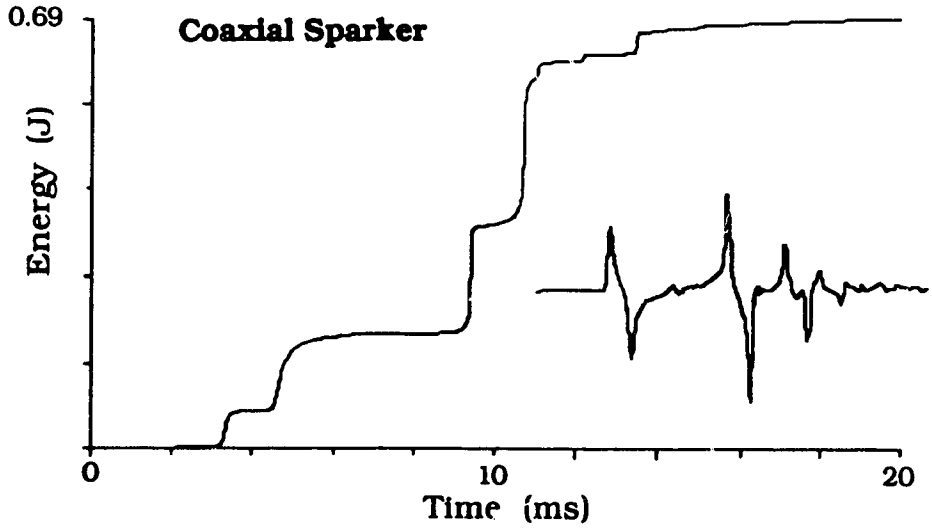

Figure 4.13: Energy versus time for a coaxial sparker.

The acoustic efficiency is calculated from

$$\eta = \frac{\text{Acoustic Energy Received}}{\text{Electrical Energy Stored}} = \begin{cases} 4.1 \times 10^{-4}, \text{ Plasma Gun} \\ 2.0 \times 10^{-3}, \text{ Parallel Sparker} \\ 2.1 \times 10^{-3}, \text{ Coaxial Sparker} \end{cases}$$

Calculations show that the plasma gun is only approximately one-fifth as efficient as either of the sparkers.

4.3.1 Energy and efficiency results.

The above figures and calculations yield several important differences between the plasma gun and the sparkers:

1. The plasma gun radiates approximately 50% of its acoustic energy in the primary pulse and 50% in the bubble pulse.
2. The sparker systems radiate approximately 20 to 30% in the primary pulse and 70 to 80% in the succeeding bubble pulses.
3. Sparker devices typically have bubble pressure amplitudes exceeding the primary pressure amplitude. This feature prevents the exclusion of this pressure feature by simple level discrimination. The plasma gun generally produces a signature with the primary pressure amplitude greater than the bubble pressure amplitude.
4. Sparkers are nearly five times more efficient than the plasma gun.

Chapter 5

Theoretical models

5.1 Introduction to the modeling.

Development of a theoretical model that explains the conversion of stored electrical energy into useful acoustic energy is divided into three separate time regimes: the very early (the first few microseconds), the early, (approximately the first hundreds of microseconds), and the later, (a few milliseconds following the early regime). These regimes correspond approximately to: the electrical arc processes within the cavity, the interaction of plasma produced by the cavity with the surrounding water that results in its vaporization from the cavity--bubble--water interface, and the expansion of the bubble into the surrounding water. The models were designed to predict the pressures as functions of time in the cavity, in the expanding bubble, and in the surrounding water.

Modeling of the processes was based upon the early experimental data and predictions were confirmed by specific experiments.

5.2 The first few microseconds.

When a sufficiently high voltage pulse is applied to a gas, electrical breakdown occurs which creates conducting pathways which may enlarge, allowing large currents to develop. The development of the large currents results in a fully developed electrical arc.

Works by Topham [1971, 1972a, b] and by Cowley [1974] have produced an integral method of treating cylindrical arcs. Applying this treatment to the plasma gun the energy per unit time per unit length that heats the gas in the cavity is given by

$$\frac{\partial}{\partial t}\int_{o}^{R_c} \rho (h - h_\infty) 2\pi b db \qquad (5.1)$$

where ρ is the plasma density, h the specific enthalpy in the channel, h_∞ the specific enthalpy of the cold gas, and R_c the radius of the cavity. The geometry of the system is shown in Figure 5.1.

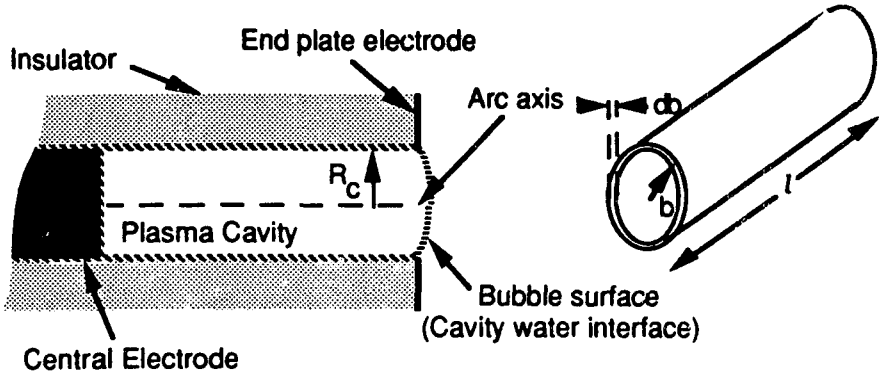

Figure 5.1 Geometry of the plasma cavity (left) and of the expanding arc channel (right).

The electrical energy per unit time per unit length is $[I(t)]^2 R/l$ where I is the current, and R/l is the resistance per unit length of the arc column. Since $R/l = 1/(\sigma A)$ where σ is the conductance, and A the arc area, the heat energy (5.1) may be equated to the electrical energy if radiation losses calculated to be approximately 10% of the input power are neglected

$$\frac{\partial}{\partial t}\int_{o}^{R_c} \rho (h - h_\infty) 2\pi b db = \frac{[I(t)^2]}{\int_{o}^{R} \sigma 2\pi b db} \qquad (5.2)$$

The left term of (5.2) is the rate that heat is being stored in the expanding cylinder of ionized gas, and the right term is the electrical power input to the arc. Following Cowley, as the heated cylinder expands between the arc radius and the cavity radius, R_c, the unheated gas surrounding the arc is adiabatically compressed by the advancing

arc. The effectiveness of the heated gas is given by

$$\int_0^{R_c} (\rho_\infty - \rho)\, 2\pi\, bdb = \rho_\infty \int_0^{R_c} (1 - \frac{\rho}{\rho_\infty})\, 2\pi\, bdb = \rho_\infty\, \theta_\delta \qquad (5.3)$$

where ρ_∞, the density of the unheated gas has been used to normalize the integrand and θ_δ is called the thermal area [Cowley 1974]. The quantity ρ/ρ_∞ is near unity outside the thermal boundary of the arc and has a relatively small value inside it, so that θ_δ is a good measure of the thermal influence of the arc. Similar treatment of the enthalpy yields

$$\theta_\Delta = \int_0^{R_c} \frac{\rho\, h}{\rho_\infty\, h_\infty} (1 - \frac{h_\infty}{h})\, 2\pi\, bdb, \text{ the enthalpy area} \qquad (5.4)$$

and for the conductance yields

$$\theta_c = \int_0^{R_c} \frac{\sigma}{\overset{*}{\sigma}}\, 2\pi\, bdb, \text{ the conductance area} \qquad (5.5)$$

where $\overset{*}{\sigma}$ is the specific conductance of the heated gas.

Substitution of these values into (5.2) yields

$$\frac{\partial}{\partial t} (\rho_\infty\, h_\infty\, \theta_\Delta) = \frac{[I(t)]^2}{\overset{*}{\sigma}\theta_c} \qquad (5.6)$$

θ_δ is regarded as the effective area of the heated gas: the arc may be thought of as making a hole of area θ_δ in the unheated gas of cross-sectional area A_c (the cavity area); then $(1 - \theta_\delta/A_c)$ is the compressed area of the unheated gas. The density, ρ_∞, of the compressed gas is

$$\rho_\infty = \rho_o/(1 - \theta_\delta/A_c) \tag{5.7}$$

where ρ_o is the initial gas density in the cavity.
The ideal gas law may be written

$$\frac{p}{\rho} = \Re T = \frac{\Re h}{c_p} \quad \text{or} \quad \frac{p_\infty}{\rho_\infty} = \frac{\Re h_\infty}{c_p} = \frac{\gamma-1}{\gamma} h_\infty \tag{5.8}$$

where $\Re$ is the ideal gas constant and γ is the ratio of specific heats.
To further simplify the equations the area integrals are taken in ratio to θ_δ, which is taken as a standard measure of the size of the arc that may be experimentally measured, e. g.

$$\Lambda_\Delta = \frac{\theta_\Delta}{\theta_\delta} \quad \text{and} \quad \Lambda_c = \frac{\theta_c}{\theta_\delta}$$

These Λ ratios are called shape parameters and are used to simplify the various equations. The Λ's are generally of unknown functional dependence that depend on the shapes and magnitudes of the temperature distributions, but not on their radial scale. Shape parameters are found to depend mainly on the electric field-current product in many situations. To proceed it is necessary to make some assumptions or estimates, the simplest is to take Λ_Δ and Λ_c as constants. This has been found to be a good assumption at high power gradients [Topham 1972 b].

Substituting the shape parameters into (5.6) gives

$$\frac{\partial}{\partial t}\left[\frac{\gamma}{\gamma - 1} p_\infty \theta_\delta \Lambda_\Delta\right] = \frac{\left[I(t)\right]^2}{\sigma^* \theta_\delta \Lambda_c} = \frac{\gamma}{\gamma - 1} \Lambda_\Delta \frac{d}{dt}\left(p_\infty \theta_\delta\right) \tag{5.8}$$

Adiabatic conditions may be written

$$\frac{p_o}{\rho_o^\gamma} = \frac{p_\infty}{\rho_\infty^\gamma} = \text{constant} \tag{5.9}$$

where p_o is the initial gas pressure. Finally substitution of the adiabatic conditions and some algebraic rearrangement yield the following

$$\theta \frac{d}{dt}\left(\frac{\theta}{(1-\theta)^{\gamma}}\right) = \frac{\gamma - 1}{\gamma p_o \Lambda_c \Lambda_\Delta \sigma^* A_c^2}\left[I(t)\right]^2 \qquad (5.10)$$

Solution of this differential equation for $\theta = \theta\delta/A_c$--the normalized thermal area--using gas constants, shape parameters, conductivity, cavity dimensions, and currents appropriate to the experimental conditions yielded the results shown in Figure 5.2.

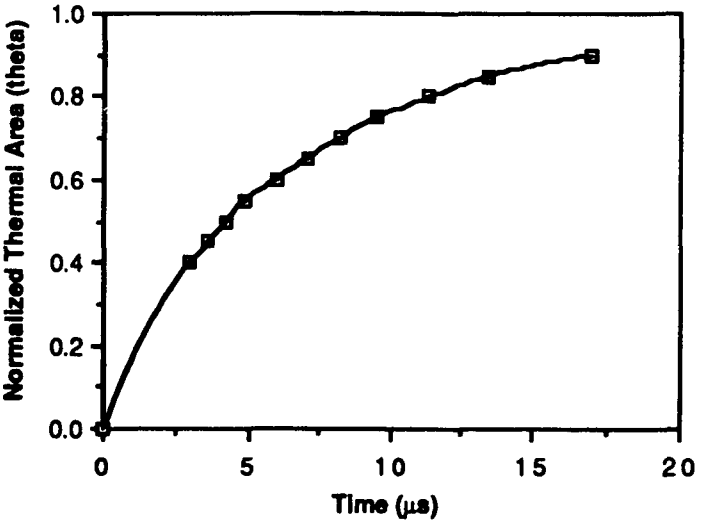

Figure 5.2: Normalized thermal area versus time.

Results from the calculations predicted that the arc would expand to approximately 90% of the cavity volume in only 15 to 18 μs. At this time the arc would become wall stabilized with most of its energy going into the cavity walls. This condition was clearly not a viable candidate for the production of a pressure pulse lasting for hundreds of microseconds.

5.3 The first few hundred microseconds.

Calculations for the arc processes showed that the arc reached the cavity wall in the first few microseconds of the current pulse. The end of the arc is in direct communication with the surrounding water through the end plate electrode exit port. Heat from the cavity is available to evaporate water from the cavity-water interface of an assumed hemispherical expanding vapor bubble. Figure 5.3 is a schematic of the process. Heat must be added to evaporate this amount of water at the rate of

$$\frac{dQ}{dt} = L\frac{dm}{dt} \tag{5.12}$$

where Q is the heat, m the evaporated water mass, L the effective heat of evaporation and t, the time.

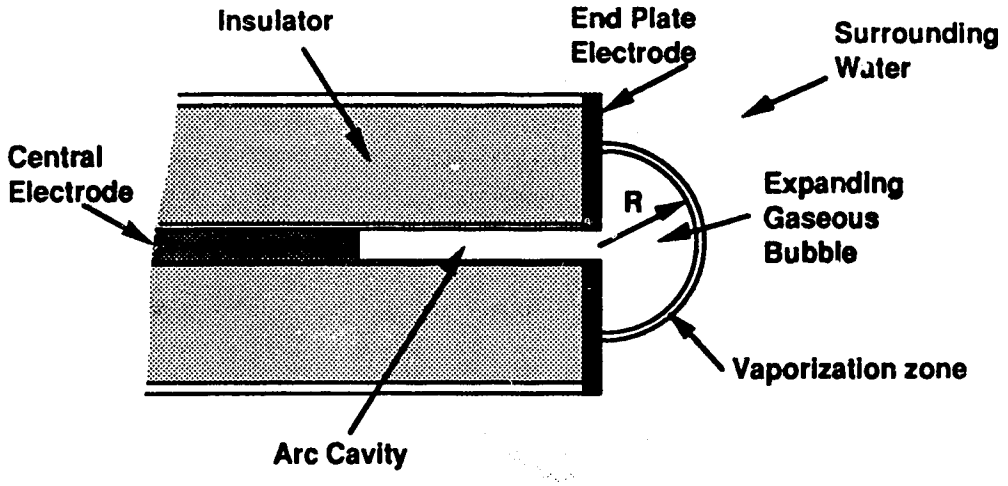

Figure 5.3: Expanding hemispherical vapor bubble.

This heat is supplied by the arc, assuming an underdamped discharge

$$\frac{dQ}{dt} = \frac{[I(t)]^2}{\int_0^{R_c} \sigma 2\pi b db} = \frac{l I_o^2 \sin^2 \omega t}{\overset{*}{\sigma}\theta_c} = I_e V_e \qquad (5.13)$$

The subscripted e's on the current and voltage represent experimental values. The remaining quantities are defined in **5.2.**

An extensive series of measurements using capacitances of 100, 200, and 300 μF, inductances of 13 and 51 μH, and charging voltages of 600, 800, and 1000 volts were performed to determine experimental values for the right hand side of (5.9). The current was measured with a standard Rojowski coil and the voltage by a differential method, to compensate for the fluctuating ground level, using two matched, equally compensated high voltage probes. Similar methods are detailed by van Rien [1978] and Golding [1971]. Figure 5.4 shows the results for a 100 J stored energy discharge (V = 1000 V, C = 200 μF, L = 51 μF). The drop in the voltage below zero following cessation of current (0.47 ms) is thought to be caused by the

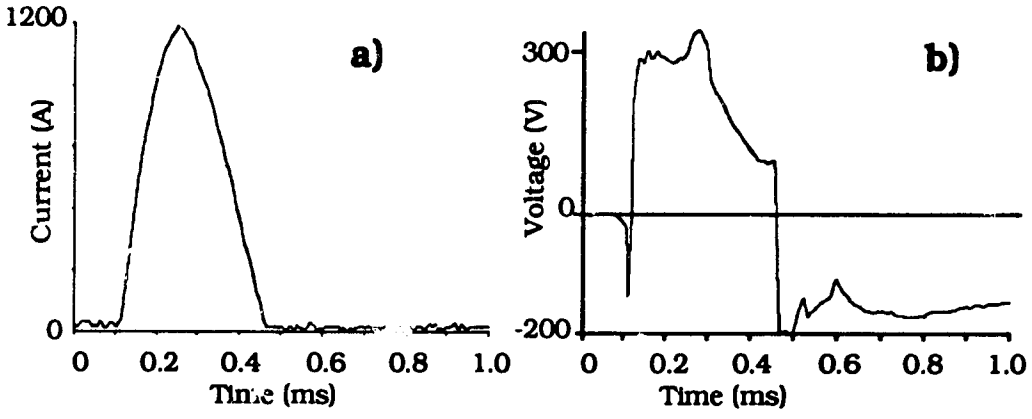

Figure 5.4: a) Arc current and b) voltage for a 100J discharge.

overloading of the differential amplifiers of the 7D20 oscilloscope. Values from this discharge will be used as an example in the modeling that follows. In general, results of the measurements are that the arc voltage peaks at approximately 30 to 50% of the capacitor voltage during the current discharge. Higher frequency discharges peak at higher voltages. The shape of the voltage waveform is approximately trapezoidal.

Arc temperatures in cylindrical arcs are reasonably insensitive to the electric power gradient, $T \sim (IE)^{2/7}$, where I is the current and E the electric field strength [Topham 1970]. After the arc is established temperatures would remain nearly constant during most of the current discharge. With the arc temperature changing slowly and evaporation being essentially an isothermal process, it is reasonable to assume an isothermal process during the evaporation inside the bubble.

The time derivative of the ideal gas law may be written as

$$\frac{d(pV)}{dt} = \frac{dm}{dt}\Re T \tag{5.14}$$

where p is the pressure within the bubble, V its volume, m the mass of liquid being evaporated, $\Re$ the ideal gas constant, and T the absolute temperature. Substituting for dm/dt in (5.12) and (5.13) yields:

$$\frac{dQ}{dt} = L\frac{dm}{dt} = \frac{L}{\Re T}\frac{d(pV)}{dt} = I_e V_e \tag{5.15}$$

Rearranging and integrating gives an expression for the pressure

$$p(t) = \frac{1}{V}\left[\frac{\Re T}{L}\int_0^t I_e V_e \, dt + p_o V_o\right] \tag{5.16}$$

where the subscripts on the pressure and volume symbols indicate initial conditions.

Both the high speed photographic and videographic images of the plasma gun discharge are limited during the early parts of the discharge. The intense light of the arc discharge overexposes both the photographic film and the charge coupled device in the video system. In addition, the electromagnetic pulse associated with the arc discharge interferes with the electronic circuitry of the video system. Filters are of little use when it is desired to image the bubble during discharge and after the discharge is complete. To overcome some of these difficulties experiments using a high speed rotating prism drum camera as a streak camera imaged the expanding bubble during the time it was illuminated by the current discharge. This system sweeps the expanding image across a strip of film at the rate of approximately 1.3 mm/μs, allowing the measurement of the diameter of the bubble versus time.

The measurements show that the bubble expands at very nearly constant radial velocity during the current discharge, this has been observed by others [Arsentev, V. V. 1965] for sparkers and explosives. Work by Steward and Baird [1980] also show an initially constant rate of bubble expansion but with a 100 μs or so delay in the initiation of the bubble growth after discharge. The delay in bubble growth was not seen in this study. With constant radial expansion the volume of the expanding bubble can be represented by

$$V(t) = \frac{2}{3}\pi(R_o + vt)^3 \qquad (5.17)$$

where R_o is the effective initial spherical radius of the bubble representing the cavity volume and v is its constant radial velocity.

Not all of the heat developed by the arc will evaporate water at the bubble interface: some is lost to the insulator, the electrodes, and a minor amount to radiation. To account for these losses only a fraction, f, of the arc energy should be included in the pressure equation. Incorporating $V(t)$ and f into (5.14) yields

$$p(t) = \frac{3}{2\pi(R_o + vt)^3}\left\{\frac{\Re T}{L} f \int_0^t I_e V_e \, dt + p_o V_o\right\} \qquad (5.18)$$

Measurements made from the high speed video images show that the total energy within the bubble is about six to seven percent of the delivered electrical energy ($\int I_e V_e dt$). An estimate of f is then of the same magnitude. Figure 5.5 is a plot of the bubble pressure using a constant expansion velocity, v, of 40 m/s obtained from the streak photographs and an electrical efficiency, f, of 7% from the bubble and power measurement data. The best fit of the model to the experimental pressure curve was found for a temperature of 2,000 K. An experimental pressure signature obtained in the acoustic test tank corrected for the inverse distance spherical spreading loss is also shown. Figure 5.6 plots the bubble pressure with an expansion velocity of 33 m/s along with an experimental pressure obtained using the same stored energy, and capacitance, but with approximately four times the inductance (Figure 5.6 is the pressure model for the voltage and current values given in Figure 5.4). Both model and experimental pressure signatures had the same electrical parameters. Again the best fit for the model was found at 2,000 K.

Values incorporated into each model calculation for delivered electrical energy ($\int I_e V_e dt$), the expansion velocity of the bubble, v, and the efficiency, f, were obtained from separate experiments (voltage and current measurements, streak photographs, and video bubble diameters) but all circuits for each of the separate experiments used the same electrical parameters. Experimental pressure traces using the EDO 6166 hydrophone shown on the figures were obtained from discharges with the same electrical parameters as those used in the modeling.

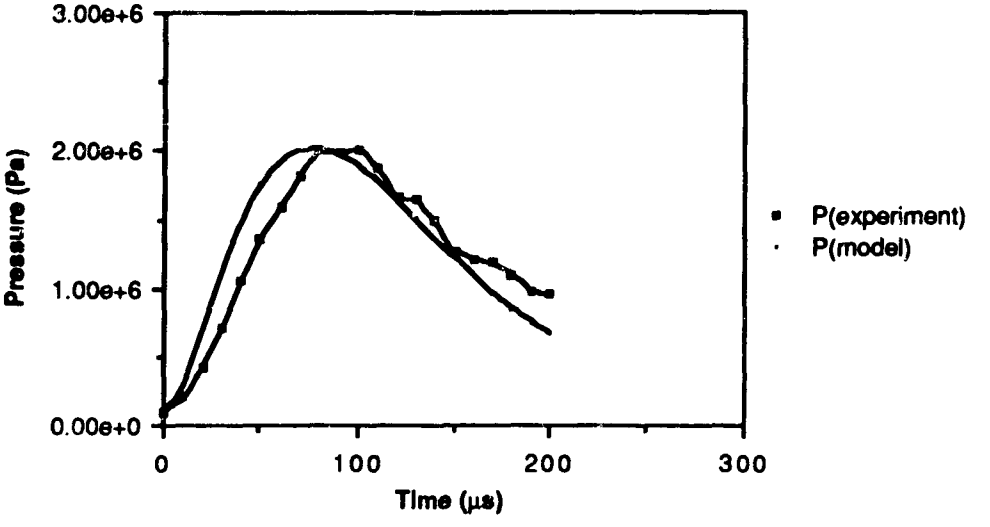

Figure 5.5: Pressure versus time for model and experiment I.
Experimental values: C=200μF, L=13μH, V=1000V.

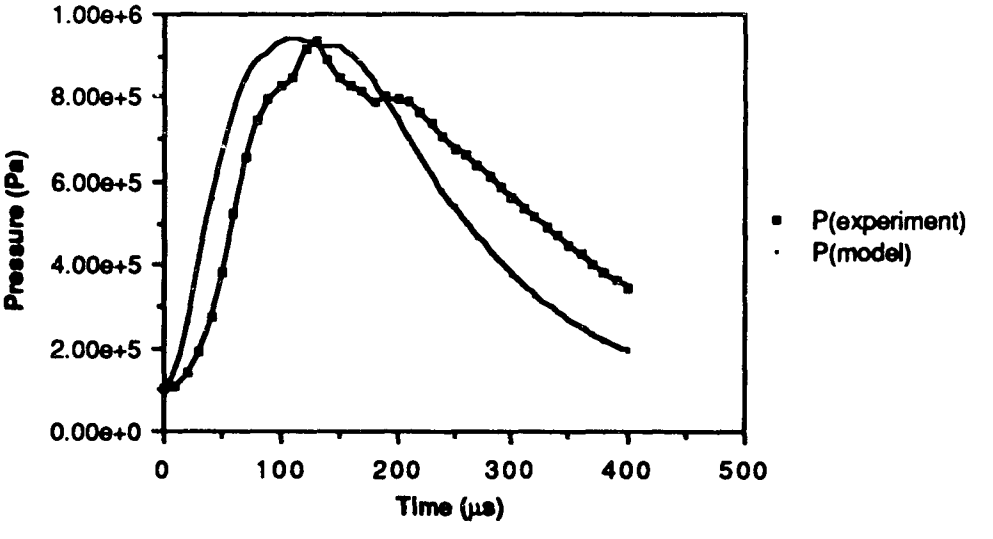

Figures 5.6: Pressure versus time for model and experiment II.
Experimental values: C=200μF, L=51μF, V=1000V.

Typically there is nearly a ten percent shot to shot variation in the peak pressures of the signatures obtained in the acoustic test tank. There is also considerable raggedness along the crest of the pressure signature from discharge to discharge. The model, even so, is seen to predict the experimental results quite well for an assumed temperature of 2,000 K, when experimental conditions for f, v, and $\int I_e V_e dt$ are incorporated. In both cases the model risetime exceeds the experimental conditions slightly. This is possibly related to the time that it takes the arc to establish itself in the cavity (see **5.2**).

5.4 The first few milliseconds.

Following the initial inflation of the vapor bubble and after reaching the peak of the power input the bubble continues to grow due to its inertia. Cooling of the hot vapor through the bubble boundary by the surrounding water and the decreasing internal pressure slows the bubble expansion to a halt. At maximum volume the pressure within the bubble is below ambient hydrostatic pressure so bubble collapse begins. Continuing collapse causes the pressure to increase dramatically producing a bubble pulse. This expansion and contraction may continue for several cycles. Physical modeling of the complex processes best proceeds along lines similar to those developed by Lamb [1945], and Keller and Kolodner [1956].

Newton's law applied to incompressible, non-flowing fluids in spherical symmetry may be written as

$$\frac{dp}{dr} = - \rho_f \frac{du}{dt} \tag{5.19}$$

where p is the pressure, r the radial distance, ρ_f the fluid density, u the velocity of a fluid element, and t the time. An expanding spherical bubble in an incompressible fluid will produce an expanding pressure pulse at a distance, the geometry of this situation is shown in Figure 5.7.

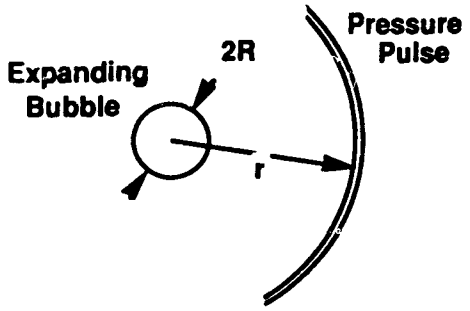

Figure 5.7: Expanding spherical bubble and pressure pulse.

The bubble velocity is u(R) and the pressure pulse velocity is u(r). The equation of continuity applied to both surfaces is

$$u(R)\ 4\pi\ R^2 = u(r)\ 4\pi\ r^2$$

Solving for u(r) in terms of bubble velocity, u(R) = dR/dt, and substitution into (5.19) with some algebraic manipulation yields

$$\frac{dp}{dr} = -\rho_f \left[\frac{R^2 \frac{d^2R}{dt^2} + 2R\left(\frac{dR}{dt}\right)^2}{r^2} - \frac{2\left(\frac{dR}{dt}\right)^2 R^4}{r^5} \right] \tag{5.20}$$

Integration with respect to r with the conditions p(r) = p, and p(∞) = p_o gives the result

$$p - p_o = \rho_f \left[\frac{R}{r}\left(R\frac{d^2R}{dt^2} + 2\left(\frac{dR}{dt}\right)^2 \right) - \frac{1}{2}\left(\frac{R^2 \frac{dR}{dt}}{r^2} \right)^2 \right] \tag{5.21}$$

This equation predicts the pressure at a distance r, due to the motion of a spherical bubble centered at the origin in a fluid with ambient pressure p_o. If r = R is substituted into (5.21) the difference between

the pressure of the gas inside the bubble and the ambient fluid pressure will result:

$$\Delta p = \rho_f \left[R\frac{d^2R}{dt^2} + \frac{3}{2}\left(\frac{dR}{dt}\right)^2 \right] \tag{5.22}$$

From (5.21) it can be seen that contributions of the bubble displacement, velocity, and acceleration to the far field pressure signature are inversely proportional to r, and to the near field are proportional to $(1/r)^4$.

To test the validity of (5.21) a series of several hundred images of expanding bubbles were made using the high speed video system at the University of Alberta. A shadowgraph optical system allowed the bubbles to be imaged because of the density difference between the vapor and the liquid water. An image is made each 250 μs, magnification of the image is 0.3. A sequence of images for a single discharge is shown in Figure 5.8. Unfortunately, the electromagnetic pulse associated with the breakdown circuit of the plasma gun, generally obliterated the first two or three images. (Time increases top to bottom within each pair of images and then right to left.) Measurements were made of the average radius for each image and the result plotted versus time. A quartic polynomial fit of the data was calculated with a standard graphic package. The first and second derivatives were then easily obtained from the polynomial allowing the predicted pressure to be calculated. Figure 5.9 shows the results for both the pressure at a distance of 1 m and for the pressure within the bubble.

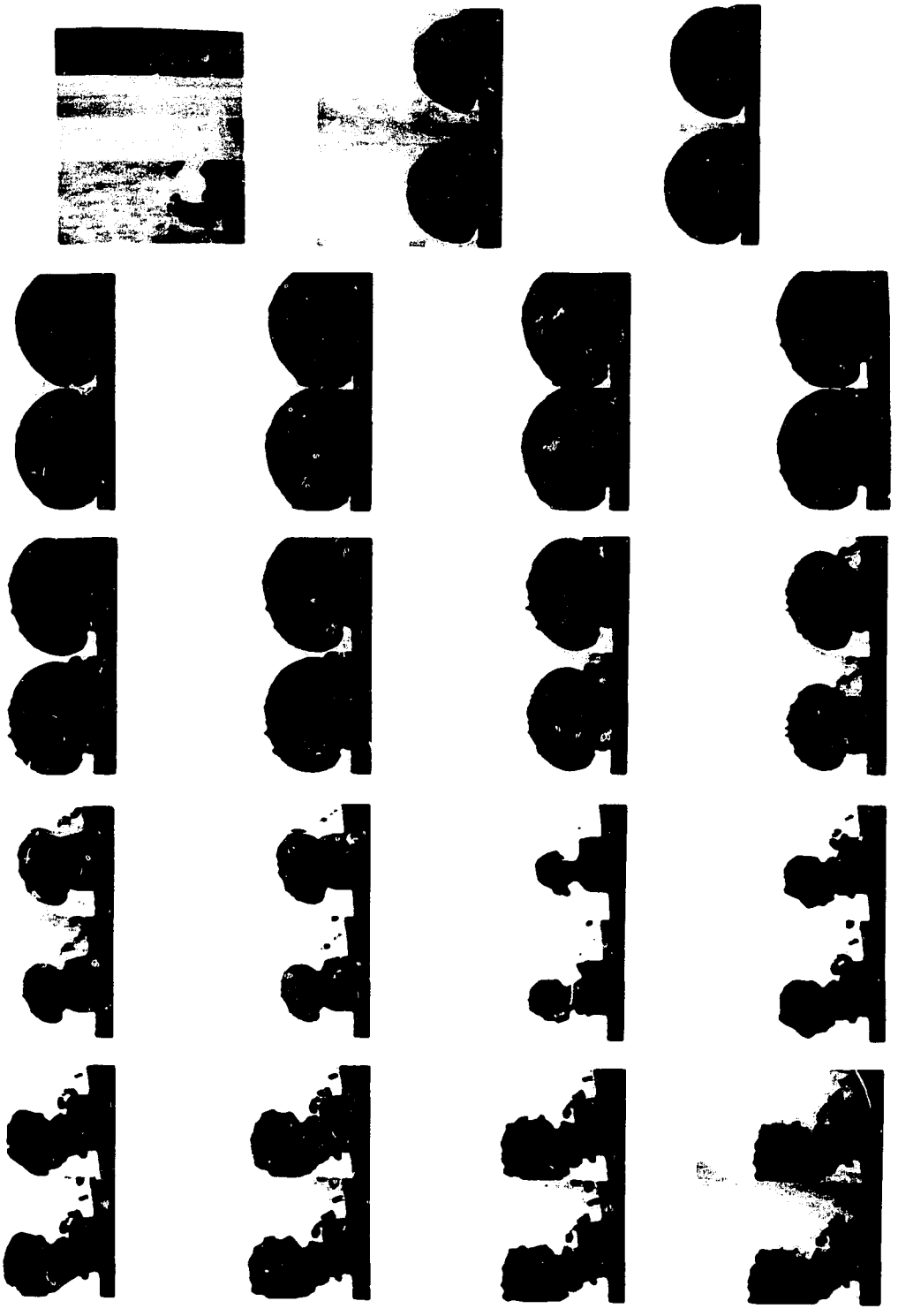

Figure 5.8: Sequence of shadowgraph video images showing bubble growth during a single discharge.

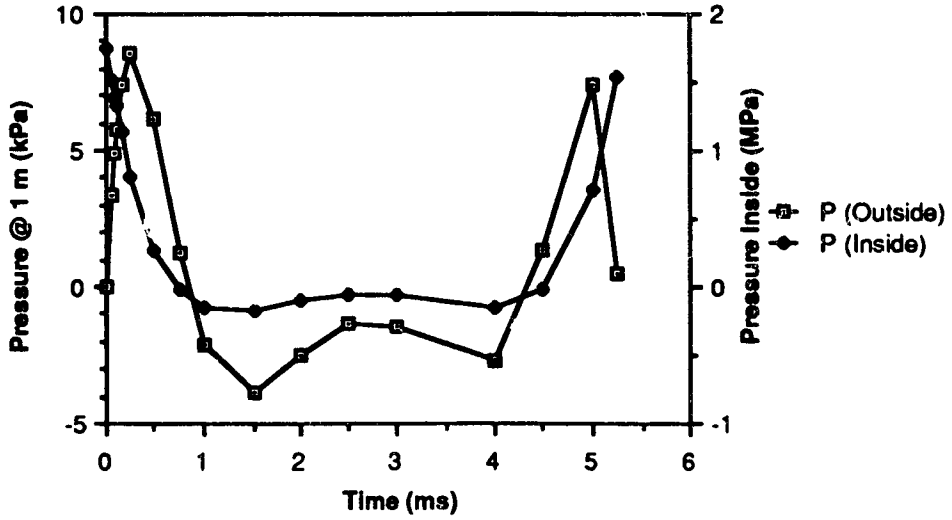

Figure 5.9: Pressure vs time for spherical bubble model.

Figure 5.10 shows results for normalized pressure at 1 m, i. e. without the near field contribution, along with an experimental normalized pressure trace obtained with the same electrical parameters (capacitance, inductance, and stored energy).

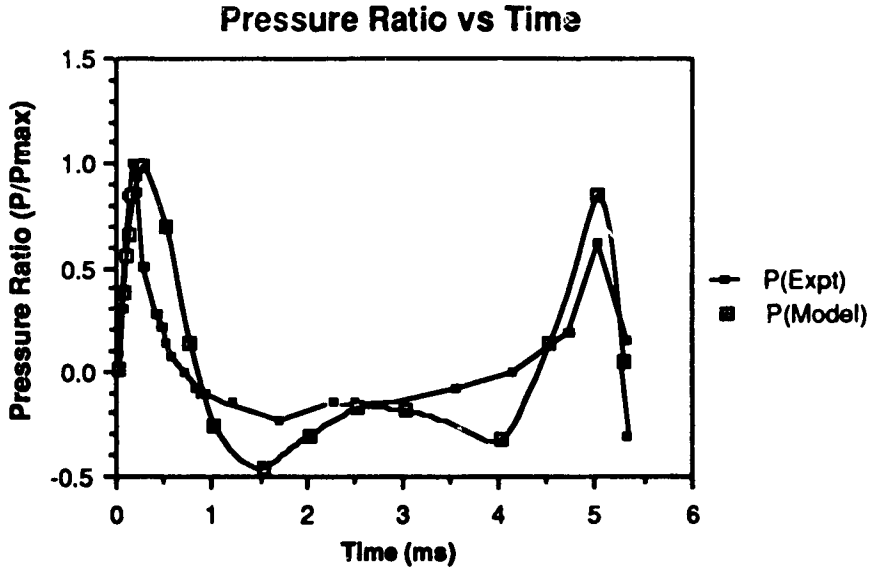

Figure 5.10: Bubble model and experimental pressures.

5.4.1 Discussion of the millisecond modeling.

Although the overall shape of the two figures are similar significant differences are apparent:

1. ***The bubble period.*** Experimentally $T_B \approx 4.2$ ms whereas the model gave $T_B \approx 4.7$ ms. It is well documented [Arons, et al. 1948] that the bubble period varies as the depth in water to the negative 5/6 power. The video images of the bubble were recorded at a depth of a few centimetres while the experimental pressure trace was the result of the plasma gun being immersed at a depth of 1.2 m. With corrections for depth the bubble periods are nearly identical. The depth effects are corrected for in the figure to give equal bubble periods.
2. ***The peak pressure.*** The model predicted a peak pressure of approximately 8,600 Pa while the measured pressure was12,000 Pa. At maximum pressure the radiating bubble is approximately 15 mm in diameter and is in fact more nearly a hemisphere than an actual sphere. A hemispherical source mounted on a infinite baffle will produce twice the pressure at a given distance compared to that of a spherical source [Kinsler and Frey, 1962]. Although the bubble is not bounded by an infinite baffle it is bounded by a 30 mm diameter disk. In addition the polynomial fit to the bubble images predicts initial radial velocities of approximately 34 m/s when streak photographs of a similar bubble gives values of approximately 40 m/s. The $2R(dR/dt)^2$ term in (5.18) is the most influential during the first millisecond of the model.

   As reported earlier the streak photographs showed that the initial radial velocity of the bubble was nearly constant, i.e. the radial acceleration near zero. This being the case the polynomial fit during the first hundred microseconds or so is probably not a good representation of the actual physics of the situation. Note also that the bubble images

indicate that the bubble differs somewhat from a true hemisphere. Other bubble images show that the bubble is not radially symmetric for all bubbles. Lack of symmetry would alter the experimental pressure signatures. It was not possible to measure pressure during the video imaging process.

3. ***The trailing edge of the primary pressure pulse.*** The polynomial fit model produces a primary pulse that is nearly symmetric about the maximum pressure point. Experimentally, the trailing edge of the pressure pulse appears to be a decaying exponential as would be expected when the bubble cavity is filled with hot vapor transferring heat to the environment. The bubble parameters do not include any energy exchanges with the surrounding water.

Nevertheless, the polynomial fit gives an adequate representation of the overall shape of the pressure signature but many details of the process cannot be predicted.

5.5 Discussion of the overall modeling

Modeling of the processes that predict the acoustic pressure signature for the plasma gun presents a considerable challenge. The arc processes; expansion, pressure increase, and temperature have reached their maximum values before bubble growth due to evaporation of water by the arc has begun. Expansion of the bubble, driven by this evaporation lasts approximately ten times the lifetime of the arc, 3 ms versus 300 μs. All of the processes seem to be very nearly decoupled in time from one another.

Physically the acoustic pressure signature measured in the surrounding fluid must be primarily due to the motion of the expanding and contracting bubble. The rate of pressure increase in the far field is determined mostly by the magnitude of the bubble expansion velocity (5.18), this in turn is determined by the electrical power input to the arc (Figure 5.6). Here the model does reasonably

well in predicting rate of pressure increase and maximum pressure, (Figures 5.5 and 5.6), although model pressures do develop faster than experiment. Following the extinction of the arc the bubble motion is due to complex interactions of fluid motion, heat transfer through the bubble surface, and condensation of the vapor in the bubble. Here the model is weakest. During this phase even more complications must occur from any asymmetry of bubble shapes. Many of the high speed video images showed definite asymmetry during expansion of the bubble. Because the nature of the bubble expansion is the cause of the pressure pulse in the surrounding water, any asymmetry is bound to have a profound effect on the pressure pulse.

An interesting experiment would be to study the plasma gun discharge in a fluid (of large volume to suppress reflections) with a latent heat of evaporation significantly less than water. Acoustic effects should be strongly dependent on the value of the heat of evaporation. Because this study dealt with an underwater acoustic source this avenue was not pursued.

It is remarkable that the bubble period seems only to depend on the total amount of energy deposited into the water by the arc over a very wide range of electrical parameters (see Figure 4.1).

Chapter 6

Seismic profiling

6.1 Introduction to profiling.

When acoustic energy is incident on an interface of materials having different acoustic impedances--such as a water-sediment interface--reflection and transmission occur. The reflected and transmitted signals obey laws similar to those of a light ray incident upon layered material of different optical densities. A portion of the reflected acoustic signals from the different layers present in the sea floor substructure may be detected by a suitable hydrophone (or array). The signal may then be amplified, filtered, and further processed prior to recording. The result, a seismic-reflection record, is an acoustic time image of the sea floor and its sub-bottom structure.

Marine seismic profiling has the objective of mapping a shallow section of the sea floor substructure--usually for various engineering objectives such as sediment investigations for harbor and channel dredging, pipe and transmission line routes, and aggregate and placer deposits. [Sheriff and Geldart 1982]. Deep seismic profiling--a similar method but with deeper penetration, higher energy, longer wavelength, and lower resolution--is of interest in petroleum exploration and is often confused with shallower marine profiling. Profiling is accomplished by firing an acoustic source at regular time intervals while it is being towed along the water surface (or below it) at constant speed along a predetermined geographic track. Receivers of the reflected acoustic signals may be either single or multi-element hydrophones (arrays) towed by the surveying vessel. A system that records the interval between the source discharge time and receipt of

the reflected signals, and ideally the position of the vessel, is necessary to reconstruct a profile of the sub- bottom structure.

Figure 6.1 is a block diagram of an acoustic profiling system. The

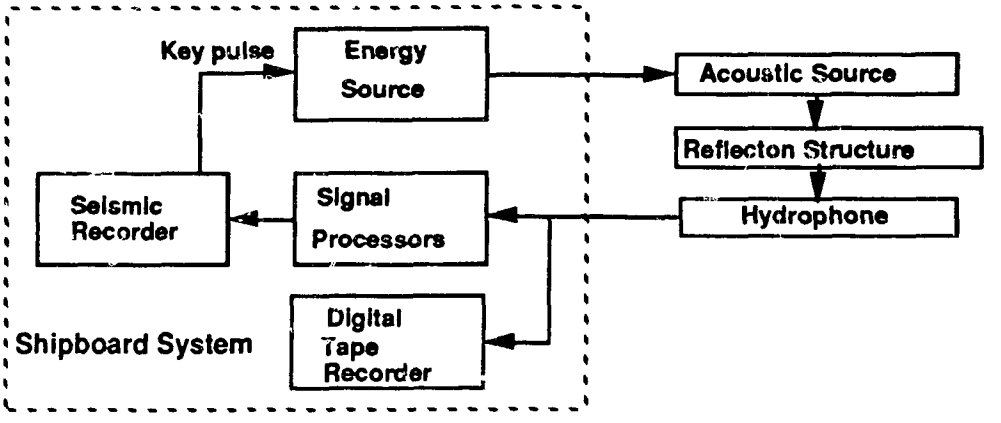

Figure 6.1: Block diagram of seismic profiiing system.

seismic recorder can trigger the seismic source at the desired time, and record the pressure information detected by the hydrophone(s). The recorder consists of a continuously moving belt carrying a metal stylus that contacts a special conducting paper moving in steps perpendicularly to the stylus. As the stylus moves with the belt it comes into contact with a conducting strip connecting it electrically to the conducting paper. The voltage between the conducting strip and the paper is proportional to the signal received by the hydrophone. Current from the conducting strip through the stylus tip produces a spark that marks the paper in varying shades of gray (actually varying sized black dots) proportional to the strength of the acoustic signal. Each sweep of a stylus across the recording paper produces a column of reflected acoustic signal versus time. Successive sweeps build up a record of the reflected signals as the chart recording paper advances with each sweep. At times during the profiling annotations on the chart paper mark the position, the sea state, and the proximity of other ships etc. The resulting record--actually a time of signal receipt versus time the recorder is

running--can then be combined with the vessel's position and an estimate of the acoustic impedance of the substructure. A depth of substructure versus position along the profiling track can be inferred.

6.2 Comparison sub-bottom reflection profiles.

Appendix B is a map showing the location of the survey sites. The survey sites Patricia Bay, Cadboro Bay, and Haro Strait were chosen for their proximity to equipment and the university, the rest were chosen for their interesting geology.

6.2.1 Plasma gun records over various bottoms.

To determine the plasma gun performance over various bottom types, sea trials were performed in shallow water depths (tens of metres or less) over a variety of sediments and substrates. Sediments included sandy muds, muds, and poorly sorted glacial diamictons. All profiles were recorded using analog acoustic chart recorders (EPC or EDO brands). Records using the plasma gun and the 1 in^3 air gun were obtained using similar deployment techniques, i.e. immersion depth, firing rates, and boat speeds.

Figure 6.2 shows portions of reflection records acquired with the plasma gun. Depth is indicated as equivalent water depth and as two-way time, the time required for an acoustic signal to travel from the surface to the given water depth and back to the surface. An array consisting of 19 Geospace MP-17 hydrophones connected in parallel and equally spaced with active length 6.1m, a preamplifier of 100x, a passband of 20 kHz, and a low frequency cutoff of 800 Hz was used.

Record 6.2 a is over sandy muds off Roberts Bank on the Fraser River delta. Coring and other surveying in the area [Hamilton and Luternauer 1983] have shown the upper series of horizontal reflectors to be Holocene sands. Record 6.2 b, was acquired over the crest of Halibut Bank: a drumlinized bank of older glacial deposits. The Cadboro Bay record, 6.2 c, is compacted glaciomarine silt that allows little acoustic penetration as evidenced by the multiple reflections.

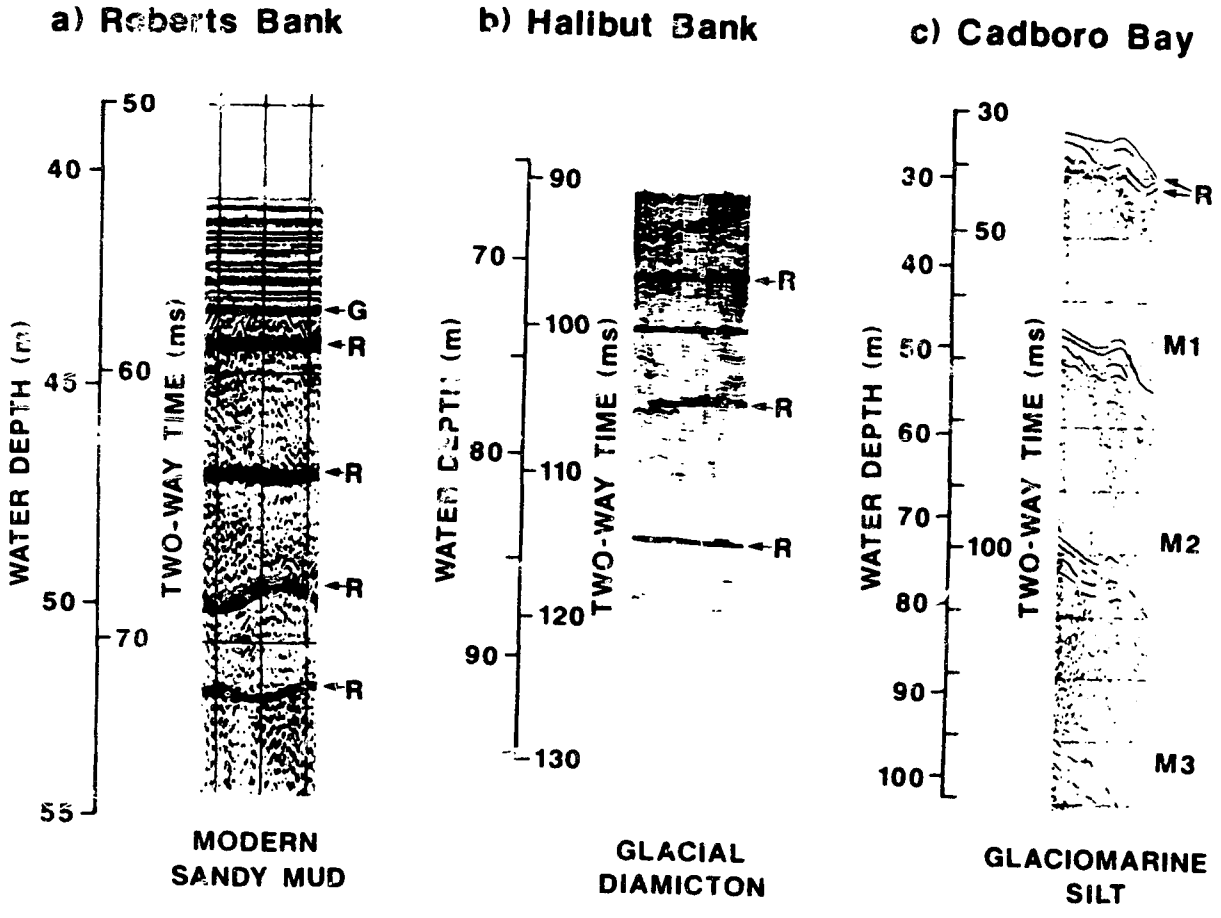

Figure 6.2: Examples of plasma gun records over three sub-bottoms. a) Roberts Bank on the Fraser River delta, b) Halibut Bank in Georgia Strait, and c) Cadboro Bay, S.E. Vancouver Island. G denotes top of glacial reflectors, R reflectors of a few hundred metres lateral continuity, and M denotes multiples. (After Pitt et al. 1988)

6.2.2 Air gun and plasma gun comparison.

The air gun (described in Chapter 2) and the plasma gun were deployed from the CSS *Parizeau* and the CSS *Vector* during separate trials. Although the profiles were approximately coincident, exact reproduction of the lines was not achieved. Figure 6.3 shows sub-bottom profiles over territory near Boatswain Bank using both the plasma gun and the air gun sources and the 19 element array described above.

The hard bottom of sediments of Boatswain Bank permit little energy into the sub-bottom. This is shown by first and second multiples from both sources in the reflection records, those of the air gun being slightly stronger. The plasma gun profile shows a suggestion of layering below the shoulder of the bank (labeled on the figure as layering). With a pulse duration of less than 1 ms, it resolves the bottom near 100 ms (74 m) with a series of short-period reverberation multiples. These multiples, called peglegs, imply a thin surface layer. In the same location the air gun reflection signature changes, also implying a veneer of less reflective material.

A comparison of survey techniques over Boatswain Bank demonstrates some of the capability of the plasma gun source. Results are shown in Figure 6.4. Note the approximate line of survey (Fig 6.4 a) for the profiles in both Figures 6.3 and 6.4. The 3.5 kHz profile (O.R.E. piezoelectric profiler Model 140) in Figure 6.4 b shows only featureless hard bottom for the bank and a shallow gas shadow developed beneath the sediments of the surrounding regions. This is consistent with the observation that piezoelectric sources, such as the 3.5 kHz transducer used here, do not penetrate hard bottomed surfaces well [Des Vallieres et al. 1978]. Apparently, the acoustic impedance contrast at the top of the gas zone is responsible for the pegleg multiple reverberation on the plasma gun profile (Figure 6.3 a) and for the different character of the reflected pulse on the air gun profile (Figure 6.3 b). These are believed to be true pegleg multiples

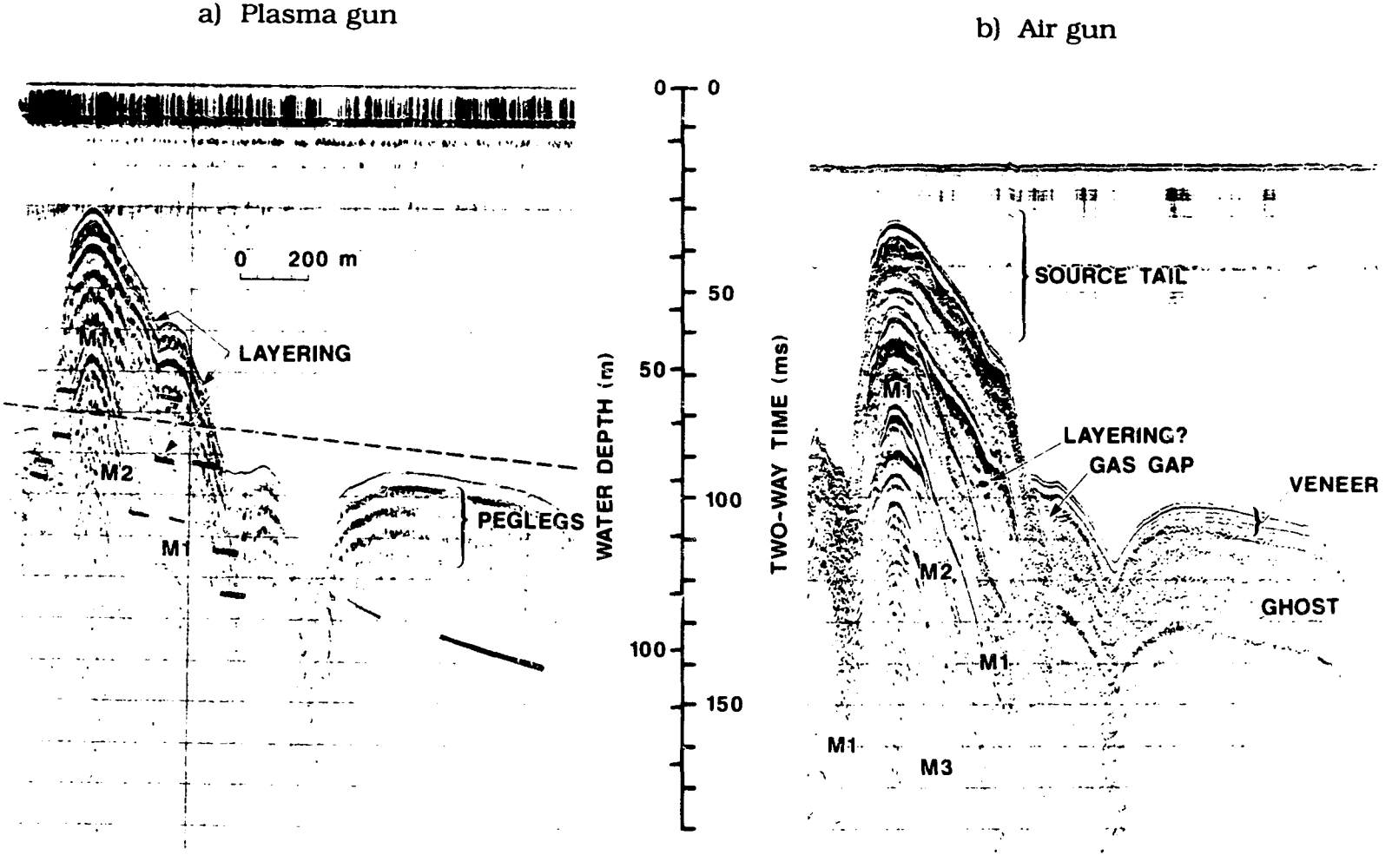

Figure 6.3: Comparative seismic reflection profiles, a) plasma gun and b) air gun over Boatswain Bank. The direct pulse (at the top of the plasma gun profile) was removed from the air gun profile. (After Pitt et al. 1988)

and not a bubble pulse because the low cut filter for Figure 2.2 a (800 Hz) should have filtered out any bubble pulse. Information necessary to better interpret the structure of this submarine feature is shown in Figure 6.4. These sub-bottom profiles were obtained using the hull mounted 3.5 kHz transducer as a passive detector. The transducer array was detuned to a passband of 1.5-3.5 kHz allowing detection of only the higher frequency components of the plasma gun. At these frequencies the hard bottom only allows about 25 ms penetration, but the erosionally truncated layers that make up the edge of bank are effectively imaged. Other electrical discharge sources, such as sparkers and boomers typically achieve about 10 ms penetration in hard bottom areas [Des Vallieres et al. 1978]. The submarine outcrops of these strata as eroded ledges are imaged in plan view by the sidescan sonar record shown in Figure 6.4 d.

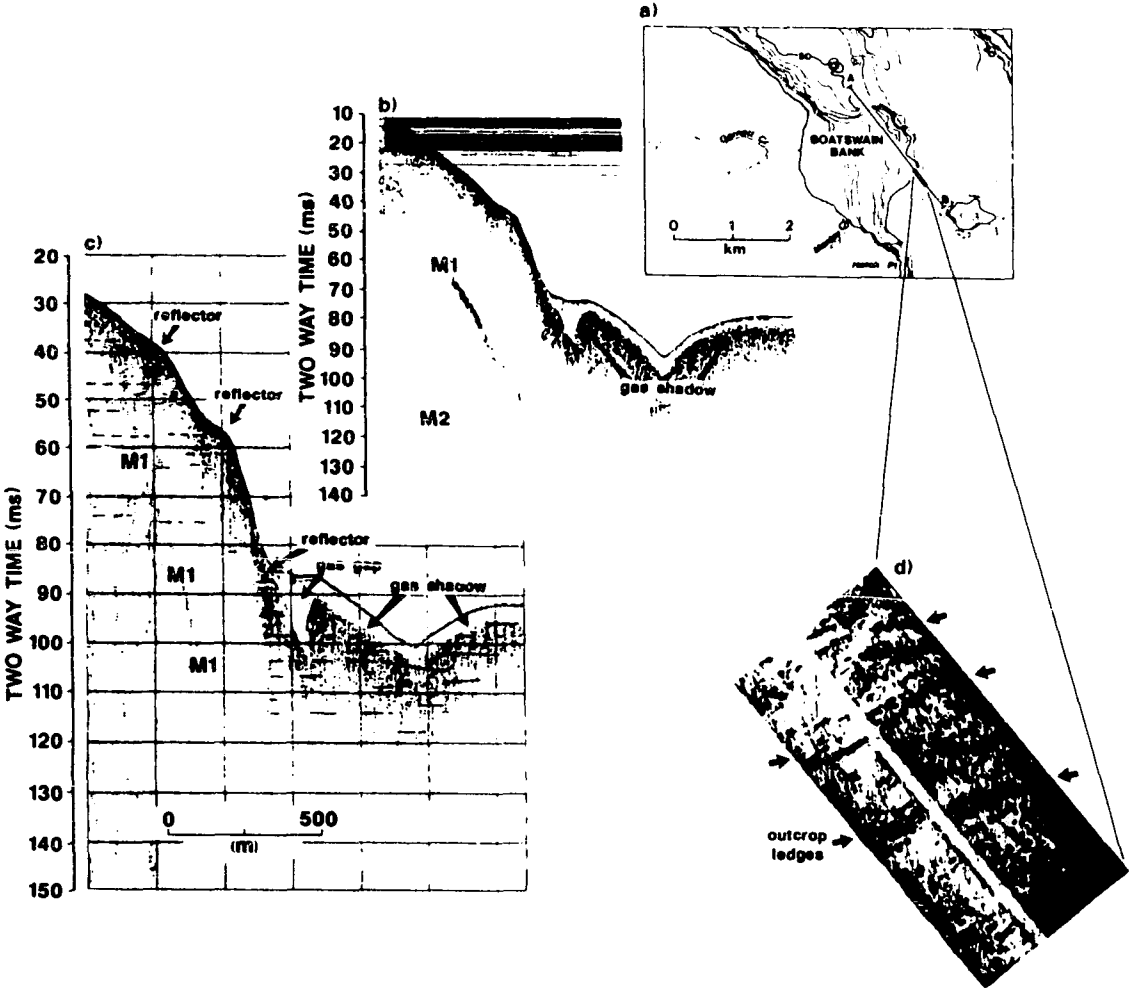

Figure 6.4: Comparison of acoustic survey techniques. a) Location map showing approximate line of profile. b) O.R.E. Model 140, 3.5 kHz profile. c) Plasma gun source with O.R.E. Model 140 as receiver. d) Klein sidescan sonar, tick marks at 25 m intervals. (After Pitt et al. 1988)

6.2.3 Comparison of plasma gun and sparker units.

Surveys of the sub-bottom of Cadboro Bay along almost identical tracks were conducted with the plasma gun and the parallel sparker (described in Chapter 3). Both devices operated with the same power supply and electrical circuit components (C = 200 μF, L = 51 μH, V = 1800 V, total energy 324 J). A Nova Scotia Research Corporation 9 element tapered hydrophone array with a variable to 30 dB preamplifier was used for these trials.

In the early development of the plasma gun, profiling was done using various filters and amplifiers that were changed as necessary during the actual profiling. What was thought to be necessary at the time proved in hindsight not always to be the case. Later in the profiling evolution the signal level was adjusted with amplifiers to produce a reasonable record on the electrographic recorder and to simultaneously record the unfiltered signal with a digital recording system similar to digital audio tape. The tape recordings could then be played back in the laboratory where suitable filtering and amplification could be introduced to produce an enhanced profile. Penetration and resolution, the opposing criteria of seismic surveying, which are always at odds with one another have to be compromised depending upon the survey requirements. With the simultaneous recording technique, it is easier to arrive at a satisfactory compromise.

Figures 6.5 and 6.6 are sub-bottom profiles made in Cadboro Bay using the plasma gun and the parallel sparker respectively. These profiles were obtained with the recording filtering technique. The direct pulse marking the sea surface has been removed from the figures. Note the lower band width, lesser resolution, and stonger multiples in the sparker profile, Figure 6.6.

The more complicated bubble pulse structure associated with the sparker units (see Figure 3.4) fails to resolve details of the sub-bottom sediments layers imaged by the plasma gun between horizontal positions 2 through 8 (the horizontal position numbers are arbitrary, the time given on the vertical scale is two-way time). The flat lying

sediments just beyond horizontal position 18, to the right of the vertical line, are overwritten by the bottom-surface multiple on the sparker profile. There is also a suggestion of deeper penetration in the plasma gun profile near horizontal position 6. The coaxial sparker produced nearly the same profile as the parallel sparker shown in Figure 6.6. The multiple bubble oscillations of the sparkers, airguns, and of conventional explosives are well documented in the literature. (see Sheriff and Geldart [1982]).

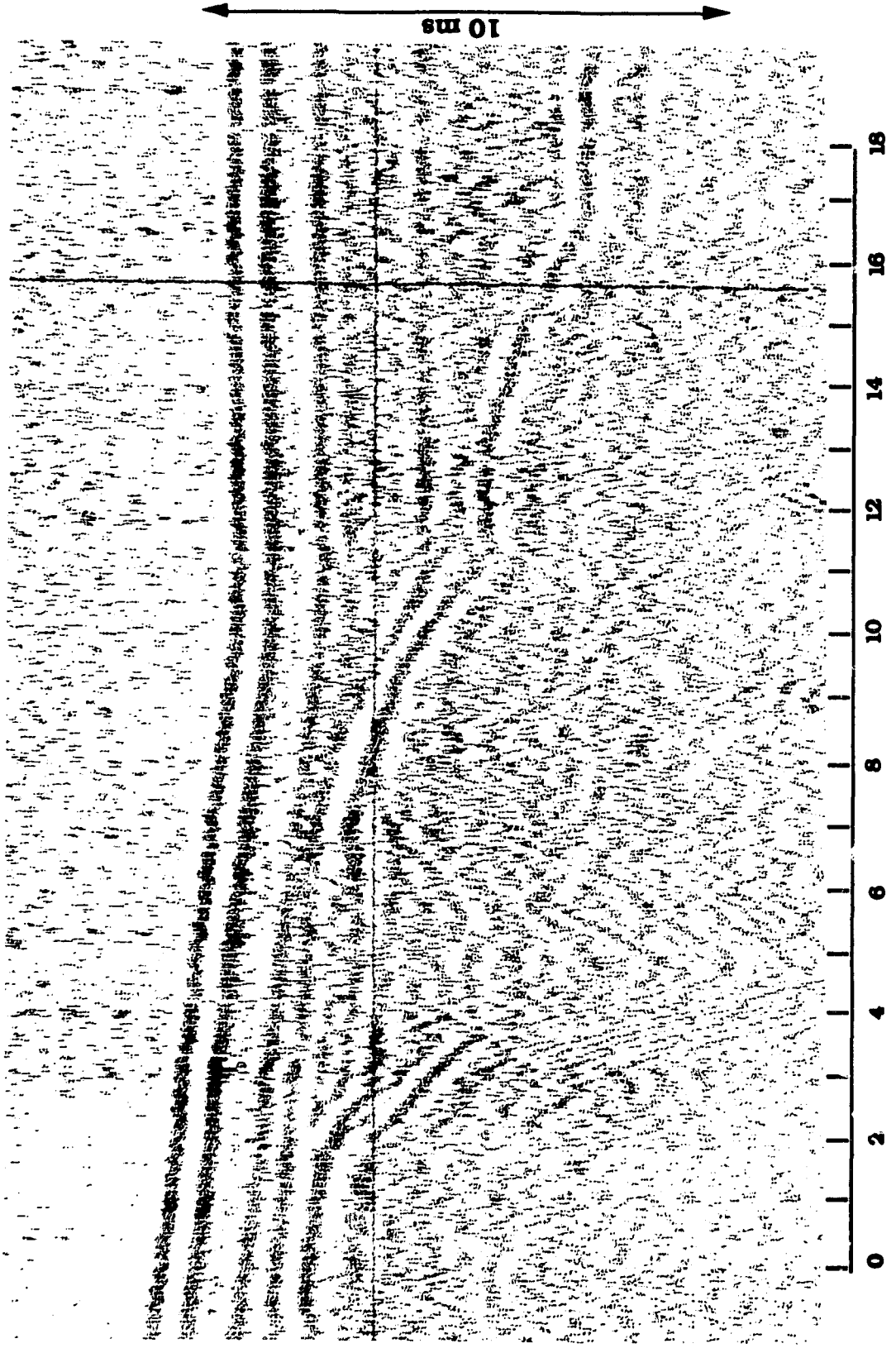

Figure 6.5: Plasma gun profile of Cadboro Bay.

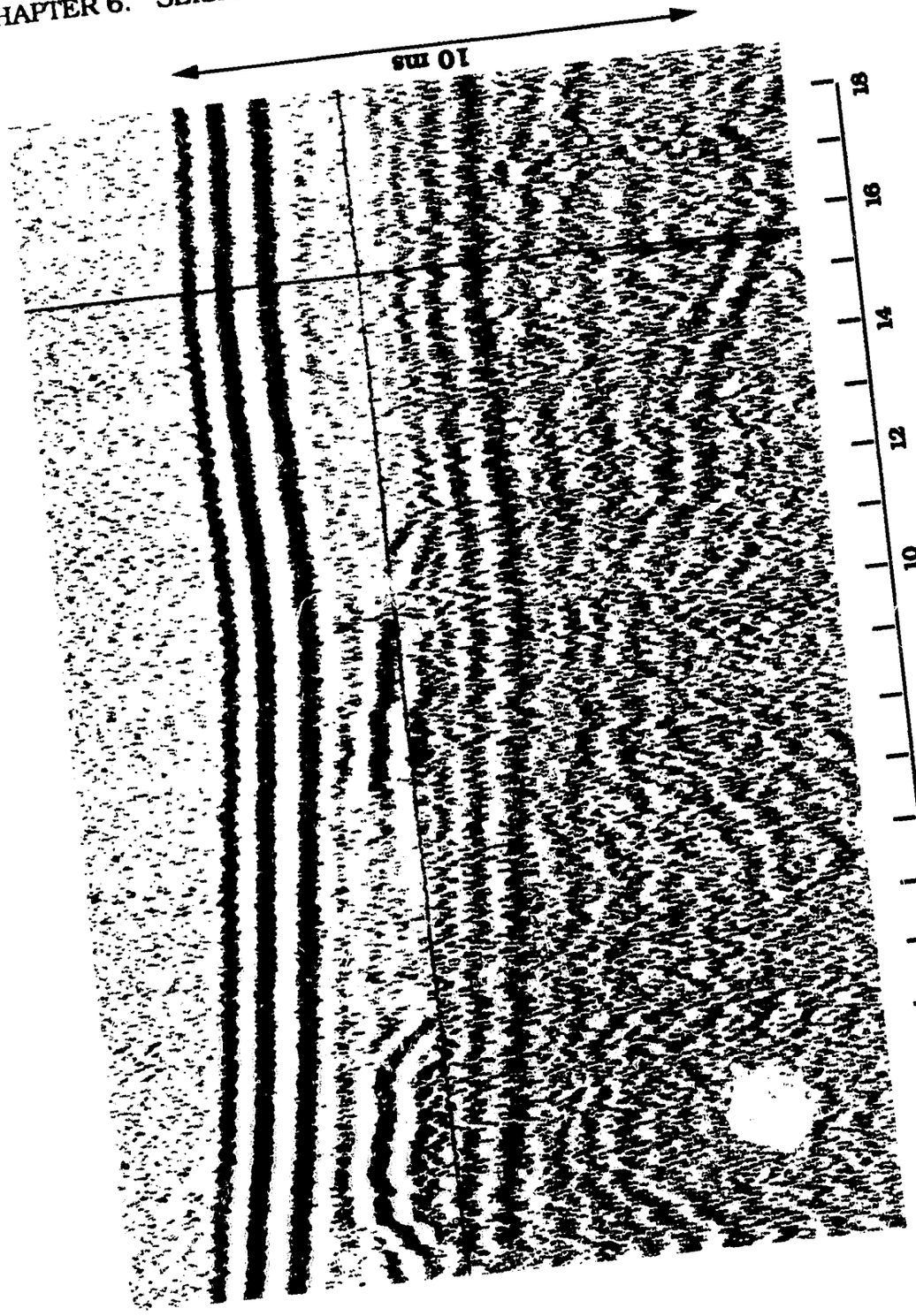

Figure 6.6: Parallel sparker profile of Cadboro Bay.

6.2.4 Comparison of the pinger source and the plasma gun.

The pinger source used was a piezoelectric transducer system (manufactured by the Raytheon Corporation in Portsmouth, RI) that operates at a carrier frequency of 7 kHz. A short wavetrain of this frequency "pings" for 1/2 ms every 1/4 s. Input power to the device is 1,000 W. A receiving transducer system is built into the pinger with variable delay and sweep to receive its own reflected acoustic signal. The receiver for thplasma gun was the 19 element array described in **6.2.1**.

A simultaneous survey on Patricia Bay compared the pinger and the plasma gun. Because of the difference in the operating frequencies (7 kHz for the pinger and 0 to 4 kHz for the plasma gun) and their separate receivers, simultaneous profiling was conducted without significant interference. Firing times for the two devices were not correlated so the plasma gun signal appears as random interference on the record. A slight amount of interference can be seen on Figure 6.7, (as dark dashes) a section of the pinger profile, indicating that the plasma gun has some energy at least up to 7 kHz. Figure 6.8 is a section of the plasma gun record over the same territory. The stored energy of the plasma gun was 150 J and its firing rate was approximately once every two seconds.

The character of the profiles are quite different. Over these hard bottoms, resolution by the 7 kHz pinger of the upper sub-bottom is better than the plasma gun but the penetration seen in the plasma gun profile is lacking. Sedimentary layers imaged by the plasma gun under the hilly structure between horizontal positions 0 and 12 are not seen on the pinger profile. Layering seen on the pinger record near horizontal position 18, between the sea floor and the hilly structure, is not imaged well by the plasma gun.

With the frequency and electrical energy differences between the two devices being quite substantial, (pinger ≈ 500 J per ping, plasma gun ≈ 150 J per shot), the lesser penetration expected from the pinger is somewhat compensated for by the larger energy.

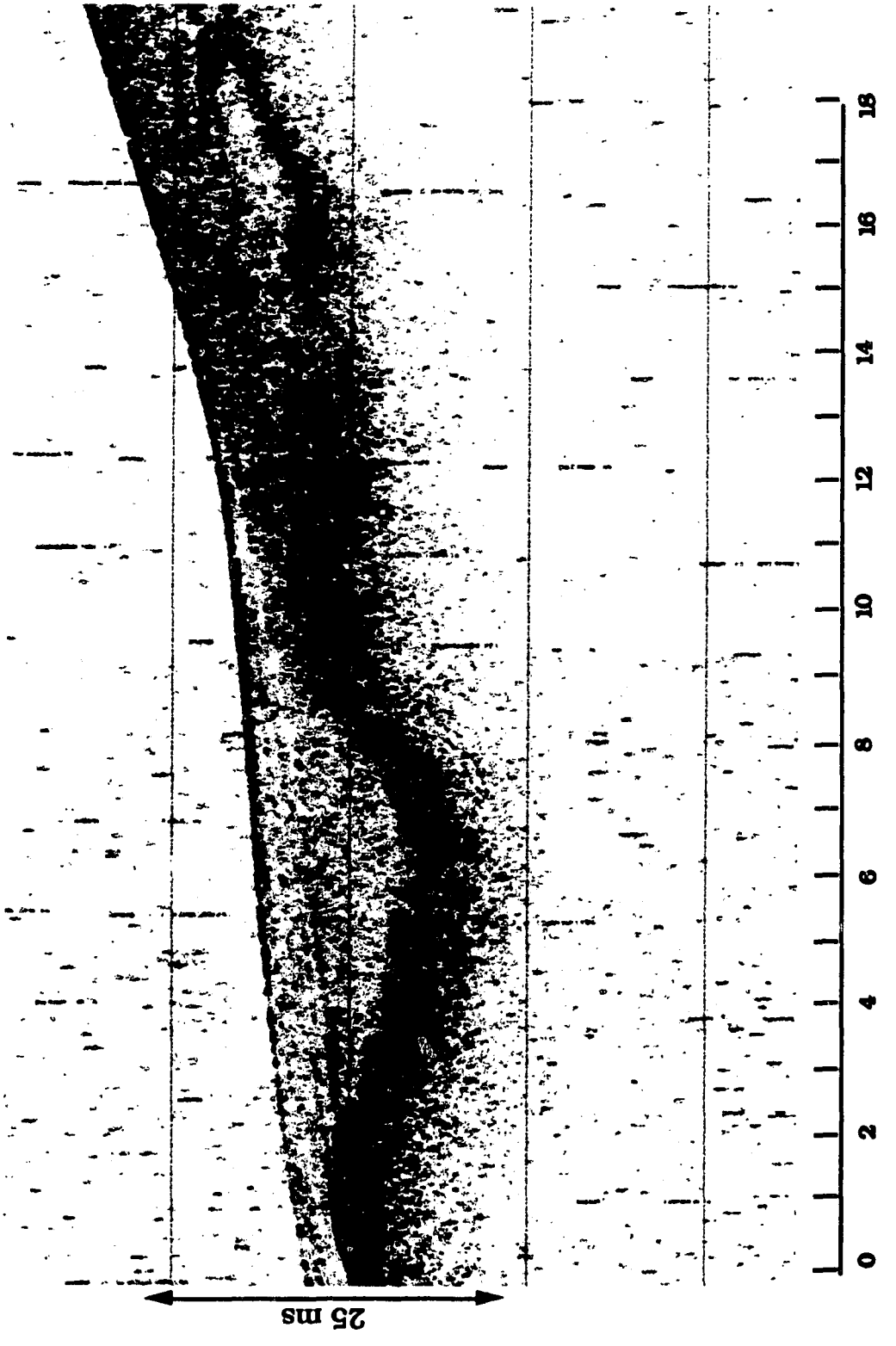

Figure 6.7: Pinger sub-bottom profile of Patricia Bay.

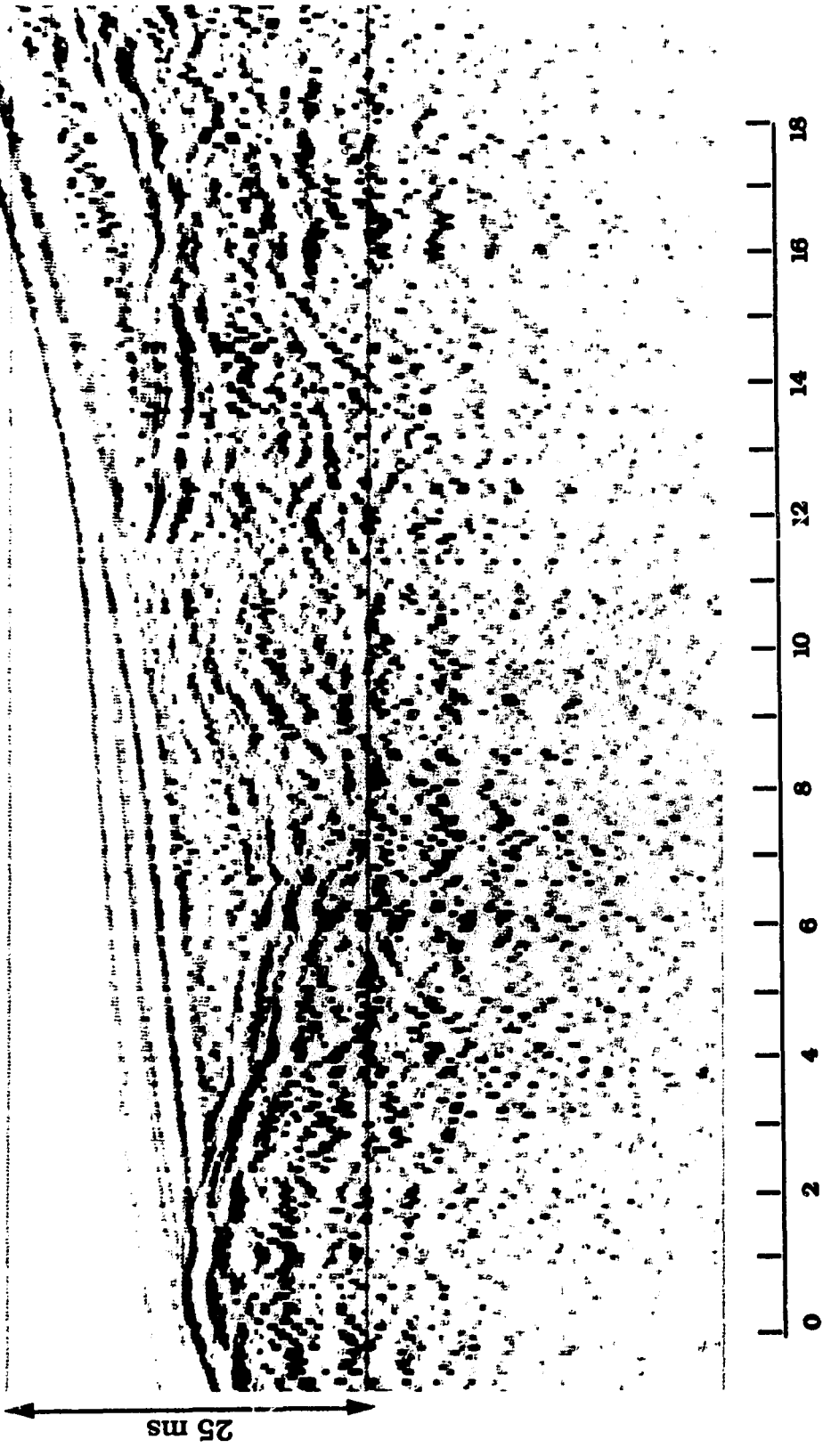

Figure 6.8: Plasma gun sub-bottom profile of Patricia Bay.

6.2.5 Comparison of the plasma gun and boomer source.

The plasma gun and the boomer source (Uniboom®, manufactured by EG&G, Waltham, MA) were compared in Patricia Bay using a jet drive vessel supplied by Terra Surveys Inc. of Sidney, B. C. Mounted on a float, the boomer projector was towed approximately 8 m behind the boat. To avoid the stern wash the plasma gun was mounted over the side of the boat. The 9 element hydrophone array described above was used with both devices. Firing rates were approximately once per second for the plasma gun and twice per second for the boomer. Both devices operated with stored electrical energy of about 160 J. A lesser boat speed than used with the boomer was necessary for the slower firing plasma gun. Because of the slower speed maneuverability, and maintaining constant speed and proper direction over the profile track was difficult.

Figure 6.9 is a profile by the plasma gun source over a section of Patricia Bay and Figure 6.10 is a profile by the boomer in the same area. (Note that the profiles are not over exactly the same territory). The site selected for profiling was parallel to the edge of a relatively steep bank. Consequently profiling along slightly different tracks produced significant differences in the appearance of the two profiles.

Comparison of the two profiles presents some difficulties because of the differences in deployment schemes, problems of positioning, and maneuverability. The peak like feature near the center of each figure is apparently a sloping ridge that is imaged below the sediments in the boomer profile, Figure 6.10, and above the sediments in the plasma gun profile, Figure 6.9. Plasma gun penetration compares favorably with the boomer, but resolution is not as detailed. Some of the lack of resolution of the plasma gun can certainly be attributed to the deployment method and boat maneuverability problems, some must also be attributed to the bubble pulse and its lack of exact reproducibility. The highly reproducible nature of the boomer source also enhances its record.

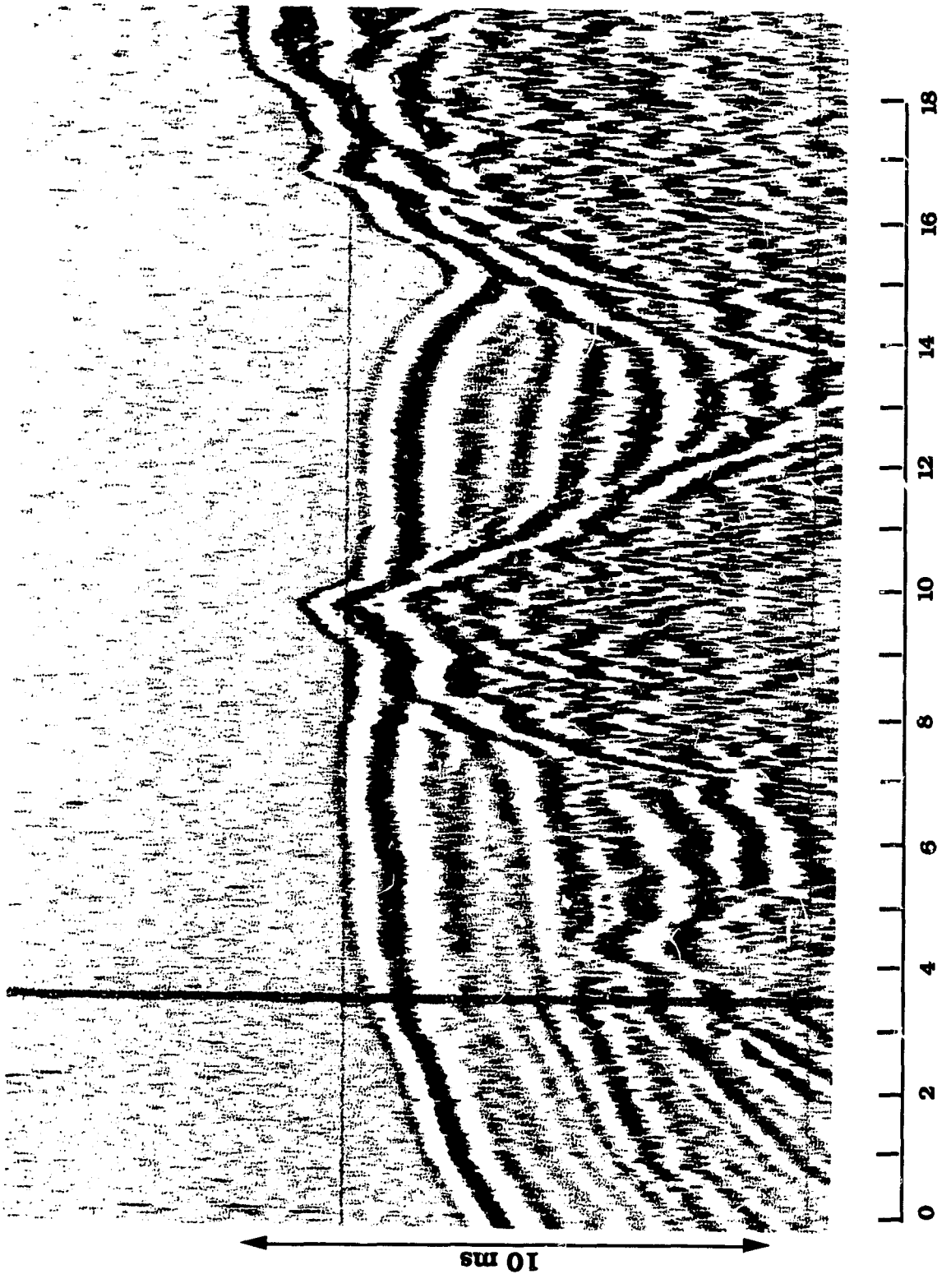

Figure 6.9: Plasma gun profile of Patricia Bay.

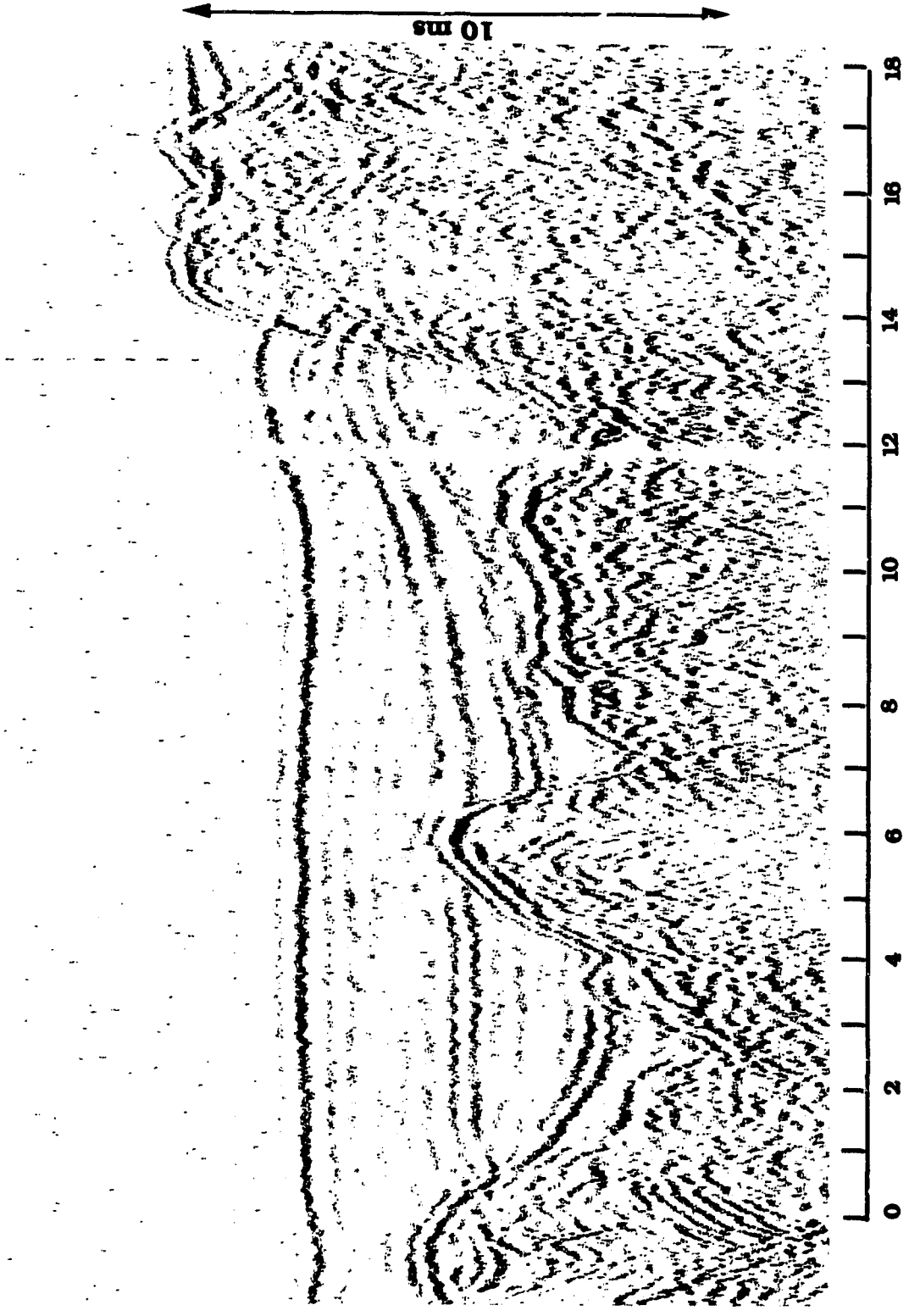

Figure 6.10: Boomer profile of Patricia Bay.

6.3. Profiling system development.

The ultimate goal of the plasma gun development is a small easy-to-handle seismic profiling system needing minimal ancillary equipment. Sufficient energy to penetrate sub-bottom structure to a depth of a few tens of metres must also be available. At the present time the system consists of a deployable section similar to that shown in Figure 2.7, and a d.c. power supply capable of charging the capacitor bank of 200 μF to 2,000 V, (400 J), twice per second. Ancillary equipment consists of a standard electrographic recorder and/or a digital recording system, two gasoline electric generators, and an air supply. A newer system, under development, considerably reduces the size of the deployable section and is designed either to be towed similar to a side scan sonar system or to be hung behind a surveying vessel as the present model is. The newer system will be of lower energy (125 J) but a commensurately higher firing rate.

A towed float system to solve some of the problems encountered with immersion, survey line direction control, and avoidance of boat wake is in the planning stages. The plasma gun system at the present time has a distinct size advantage over competing systems and it is believed that this advantage can be enhanced even more with careful design.

Conclusions and Recommendations

7.1 Conclusions.

A device suitable for sub-bottom profiling has been investigated in detail. The plasma gun has been proven suitable to probe the structure of loosely consolidated sediments to a depth of approximately sixty metres (see Figure 6.3). Comparison profiles with other standard profiling devices show satisfactory performance. A decided advantage in size, weight, and ease of deployment is enjoyed by the plasma gun. With development a very small system could evolve that would be deployable from a boat the size of a medium sized inflatable.

Considerable flexibility exists in the frequency control possible with a carefully designed system. High frequency components of the pressure signature are controlled by the electrical components of the discharge circuit (capacitance and inductance), and by the depth of immersion of the plasma cavity. Immersion depth is important because it determines the time when the surface reflected signal convolves with the outgoing signal. Low frequency components are primarily from the pressure signature shape associated with the bubble pulse and by the bubble period. Immersion depth influences the shape of the bubble pulse and its reflection in a way similar to the effect reflection has on the primary pressure pulse. The bubble period is dependent almost exclusively on the total amount of energy that is deposited into the water (deposited energy is proportional to the stored electrical energy).

The physics of the pressure production of the plasma gun is primarily the interaction of the plasma cavity arc with the surrounding

water. Arc temperatures of approximately 10^4 K develop in the cavity when the arc becomes fully developed only a few microseconds after initiation of the current discharge. After this short period of time the arc begins to evaporate water at the air-water bubble interface at the cavity exit (where air that maintains the gaseous environment in the cavity exits into the water). Evaporation of the water by the arc for the lifetime of the current discharge drives up the pressure, expanding a vapor bubble. Theoretical modeling of this process produces a best fit with an average temperature of 2,000 K.

Following the initial buildup of pressure inside the vapor bubble and its initial expansion, the vapor bubble dynamics are similar to those of a small explosion. Momentum carries the expanding bubble beyond its equilibrium pressure position until the pressure inside the bubble becomes less than the local hydrostatic pressure. Eventually the pressure of the surrounding fluid brings bubble motion to a halt. The motion is reversed, the bubble starts to collapse, this causes the pressure to increase until the collapse stops and another expansion begins. This expansion--collapse process may repeat several times. Each collapse produces another bubble pressure pulse. Pressure signatures generally show that the plasma gun "suffers" a smaller number, and less intense bubble pulses than other impulsive sources.

The rate that the bubble initially grows depends on the rate energy is deposited into the water by the arc. This rate is controlled by the time constant of the electric circuit. Maximum pressure produced by the expanding bubble depends on the square of the peak current. The peak current is also determined by the time constant of the circuit and additionally the voltage on the storage capacitors. Unfortunately the two quantities are not independent. For a given discharge current frequency, the maximum current is determined by the voltage.

The time between the first pressure maximum and the bubble pulse pressure maximum (the bubble period) is determined by the stored energy to the one-third power, i. e. $E_S^{1/3}$, the same relationship as for a small explosion.

A plasma gun design optimized for resolution, i. e. high frequency, would be built with low inductance, low capacitance, and voltage that would minimize the bubble period as much as possible. Such a source would be deployed so the reflected pulse would complement the primary pulse to produce a sharply rising pressure excursion followed by an equally sharply falling one. If the desired high frequency pulse resulted in a undesirable bubble period with too much low frequency content, filters in the receiving-recording system could probably be designed to remove it. Conversely, a low frequency source, one designed for maximum penetration, would have large inductance and capacitance and use voltages that would enable the bubble period to enhance the desired low frequencies. Immersion of the source would be deeper, allowing the reflected signal to add to the primary pulse at the time of the primary pulse half period. This would maximize the period of the primary pulse and its reflection to further enhance low frequency content.

7.2 Recommendations for further study.

7.2.1 Platform stability.

The time between the beginning of the pressure pulse and its reflection from the sea surface is important not only to the repeatability of the pulse but to its frequency content. Profiles obtained with the plasma gun when deployed from the sailboat *Sabrina* where horizontal and vertical stability of the plasma gun was the norm are much superior to those obtained using the jet drive powercraft where source stability was a serious problem.

A deployment scheme using a towed float that could be deployed away from the wake and turbulence of the survey vessel would certainly eliminate some of the problems caused by source motion and acoustic coupling. The plasma gun could be constructed with the plasma cavity exit orifice at the end of an adjustable cylinder that would allow control of immersion depth.

7.2.2 Multiple sources.

The bubble pulse, the plague of all explosive types of acoustic sources, has been mitigated considerably by the use of air gun arrays [Larner et al. 1982] and sparker arrays [Le Tirant 1979]. Several plasma gun devices of different energies designed to discharge simultaneously should produce results similar to the other arrays.

7.2.3 Reproducibility of pressure signature.

Some reproducibility problems exist with the plasma gun. Both the peak pressure and the bubble period for a given energy discharge show noticeable variation. Some discharges produce both a pressure signature and sound that are distinctly different. These anomalies are believed to be caused by the size and shape of the air bubble that happens to be attached to the plasma cavity exit at the instant of firing. Inflow of water into the cavity following discharge by the partial vacuum that results when the cavity cools between firings may also be a cause. Both of these problems need study and may be helped by some type of fast acting valve that can control the air supply to the plasma cavity prior to and after firing.

7.2.4 Study of other physical processes.

Figure 7.1 is a 1 ms long high speed video image of an 800 J plasma gun discharge (C = 400 μF, L = 13 μH, V = 2,000 V) taken after bubble collapse was well underway. The smaller bubbles adjacent to the vapor bubble edge are cavitation bubbles indicating that the pressure at that location is less than the vapor pressure of the water. At a pressure of one atmosphere (100 kPa) the cavitation threshold is 3,000 W/m^2 [Urick 1975]. Cavitation is of interest to acousticians because of the noise generated and to the limits it places on acoustic sources by its onset. Materials scientists also are interested in cavitation effects because of surface erosion produced by the large forces associated with the collapsing cavitation bubbles. Use of the plasma gun as a cavitation source for materials science studies could prove useful.

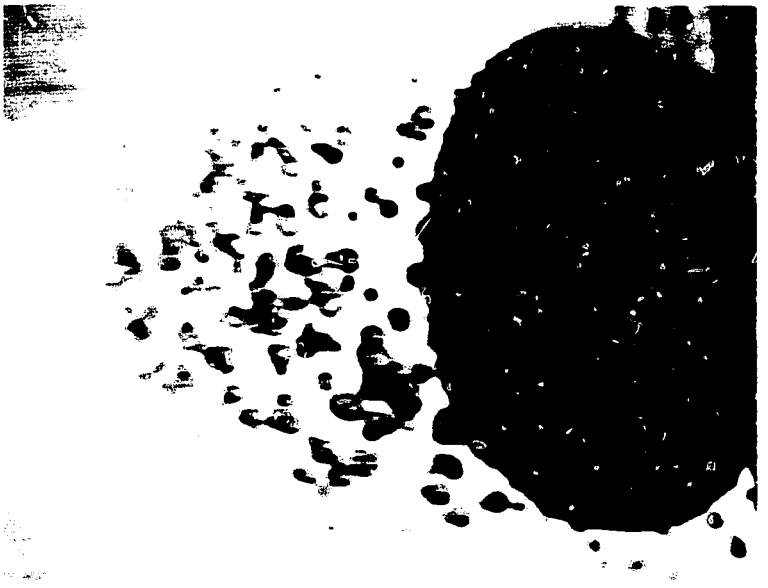

Figure 7.1: Bubble collapsing showing cavitation effects.

Periodically during the study of the acoustic properties of the plasma gun in the laboratory exceptionally long lived vortex rings were observed in the acoustic test tank (they were also recorded in some video images). The hydrodynamics of the vortices as related to the discharge conditions and cavity shapes would be another theoretical and experimental study of interest.

References

Adamson, T. C. and Nicholls, J. A., 1959, *Structure of jets from highly underexpanded nozzles into still air*, J. Aerospace Sci. **26**, 16-23

Albers, V. M., 1965, *Underwater Acoustics Handbook, 2nd Ed*, Pennsylvania University Press. University Park, PA

Arons, A. B., Slifko, J. P., and Carter, A. 1948, *Secondary pressure pulses due to gas globe oscillation in underwater explosions. I. Selection of Adiabatic parameters in the theory of oscillation.* J. Acoust. Soc. Am., **20**, 271-276

Arsentev, V. V., 1965, *On the theory of pulse discharge in a liquid*, J. Appl. Mech. and Tech. Phys. **5**, 34-37

Bunce, E. T., 1980, *Assessments of Seabed Seismic Systems*, Woods Hole Oceanographic Institution, Woods Hole, MA

Caulfield, D. D., 1962, *Predicting sonic pulse shapes of underwater spark discharge*, Deep-Sea Research, **9**, 339-348

Cheriyan, G. K., Krallis, K., and Weinberg, F. J., 1990, *Adapting continuous-flow plasma jets for intermittent ignition in gas turbine combustors.* Comb. Sci. and Tech. in press

Clements, R. M., 1984, Review of plasma jet ignition. In *"The Chemistry of Combustion Processes"* , T. M. Sloane (Ed.), The American Chemical Society, Washington, 193-204

Clements, R. M., Smy, P. R., and Topham, D. R., 1984, *Chemical activity and transport processes in the vicinity of a plasma jet igniter*, Comb. and Flame, **57**, 265-274

Cole, R. H., 1948, *Underwater Explosions*, Princeton University Press, Princeton, New Jersey

Cote, T., Ridley, J. D., and Clements, R. M., 1986, *The ignition characteristics of igniters at sub-atmospheric pressures*, Comb. Sci. and Tech., **48**, 151-162

Cowley, M. D., 1974, *Integral Methods Of Analysing Electric Arc: I Formulation* , J. Phys. D: Appl. Phys, **7**, 2218-2232

Davie, O. H., 1964, *The Elements Of Pulse Techniques*, Chapman and Hall, London

Des Vallieres, T., Kuhn, H., LeMoal, R. and Duval, J., 1978, *Test of various high resolution seismic devices in hard bottom areas*, Offshore Technology Conference Proceedings **10**:2, 1455-1466

Golding, J. F., 1971, *Measuring Oscilloscopes*, Butterworth, London

Goldstein, R. J., 1970, Optical Measurement of Temperature, in *Measurement Techniques in Heat Transfer*, E. R. G. Eckert and R. J. Goldstein (Eds.), Technivision Services, Slough, England, 177-228

Hamilton, T. S. and Luternauer, J. L., 1983. Evidence of seafloor instability in the south central Strait of Georgia, British Columbia: a preliminary compilation. *Current Research, Part A*, Geological Survey of Canada, **831A**, 417-421

Johnston, R. C., Reed, D. H., and Desler, J. F., 1988, SEG standards for specifying marine seismic energy sources, *Geophys.* **53**:4, 566-575

Keller, J. B. and Kolodner, I. I., 1956, Damping of Underwater Bubble Oscillations, *Jour. Appl. Phys.*, **27**, 1152-1161

Kinsler, L. E. and Frey, A. R., 1962, *Fundamentals of Acoustics 2nd*, Ed, John Wiley and Sons, New York

Kosenko, A. V., Portugalskii, A. V. and Tafai, E. I., 1980, Suppression of the pulsation of a vapor-gas cavity formed by an electrical discharge in water, *Sov. Phys. Accoust.* **26**:6, 491-494

Kramer, F. S., Peterson, R. A., and Walter, W. C., Eds, 1968, *Seismic Energy Sources--1968 Handbook*, Bendix United Geophysical Corp., Pasadena

Lamb, H., 1945, *Hydrodynamics*, Dover Publications, New York

Larner, K., Hale, D., Zinkham, S. M. and Hewitt, C., 1982, Desired seismic characteristics of an air gun source. *Geophysics*, **47**, 1273-1284

Le Tirant, Pierre, 1979, *Seabed Reconnaissance and Offshore Soil Mechanics for the Installation of Petroleum Structures*, Institut Francais du Petrole Publications, Paris

Levin, P. A., 1974, Underwater impulse measurements, *Tech. Review* **4**. Reprinted in Bruel and Kjaer Application Notes: *Introducation to Underwater Acoustics*, Bruel and Kjaer, Naerum, Denmark

Parkes, G. and Hatton, L., 1986, *The Marine Seismic Source*, Reidel and Co., Dordrecht, Holland

Pearce, N. G., Warren, R. D. and Clements, R. M., 1990, *Liquid fuel ignition at low temperature using a pulsed plasma jet.* Submitted for publication to Comb. Sci. and Tech.

Pitt, P. L., Smith, R. D., Sheffler, G. C., Warren, R. D., Clements, R. M., and Hamilton, T. S., 1988, *A pulsed plasma jet acoustic source for profiling the ocean floor.* Geophys. Pros. **36**, 523-536

Ridley, J. D., Pitt, P. L., and Clements, R. M., 1985,*The effect of feed gases on plasma jet ignition.* Comb. Sci. and Tech. **36**, 523-536

Scott, W. T. 1959, The Physics of Electricity and Magnetism, John Wiley and Sons, New York

Sheriff, R. E., Geldart, L. P., 1982, Exploration seismology vol. 1, History, theory and data acquisition, Cambridge University Press, Cambridge

Smith, R. D., Pitt, P. L., Ridley, J. D., Sheffler, G. C. and Clements, R. M., 1987, *Underwater sound from a pulsed plasma jet.* Acoustics Letters **10,** 161-165

Smy, P. R., Clements, R. M., Simeoni, D. and Topham, D. R., 1982, *Plasma expulsion from the plasma jet igniter,* J. Phys. D: Appl. Phys., **15** 2227-2239

Smy, P. R., Clements, R. M., Dale, J. D., Simeoni, D. and Topham, D. R., 1983, *Efficiency and erosion characteristics of plasma jet igniters.* J. Phys. D: Appl. Phys., **16,** 783-791

Smy, P. R., Clements, R. M., Oppenheim, A. K. and Topham, D. R., 1987, *Structure of the pulsed plasma jet,* J. Phys. D: Appl. Phys., **20** 1016-1020

Stewart, D. B. and Baird, J. P., 1980, *Laser interferometer probe for underwater pulse from electric arc,* Acoustic Letters, **4,** 58-64

Sun, Lin, 1988, Personal communication

Topham, D. R., 1970, *The aerodynamics of electric arcs in axial flow,* Ph. D dissertation, Loughborough University of Technology, Loughborough

Topham, D. R., 1971, *The electric arc in constant pressure axial gas flow.* J. Phys. D: Appl. Phys., **4,** 1114-1125

Topham, D. R., 1972a, *The characteristics of axial flow electric arcs subject to pressure gradients,* J. Phys. D: Appl. Phys., **5,** 533-541

Topham, D. R., 1972b, *Scaling laws for the interaction of a gas-blast circuit breaker arc with an electric circuit.* Proc. IEE **119,** 1469-1476

Topham, D. R., Smy, P. R. and Clements, R. M., 1975, An investigation of a coaxial spark igniter with emphasis on it practical use, Comb. and Flame, **25,** 187-195

Topham, D. R., Clements, R. M., Ridley, J. D. and Smy, P. R., 1986, *The initiation of combustion by a hot turbulent mixing element,* Comb. Sci. and Tech., **50,** 41-60

Topham, D. R., 1990, Personal communication

Urick, R. J., 1975, *Principles of Underwater Sound*, McGraw-Hill, New York

van Rien, K., 1978, *Oscilloscope*, Mc-Graw-Hill, New York

Waterston, K., 1973, *Some operating characteristics of novel ignition devices for hydrocarbon air mixtures*, Ph. D thesis, Oxford University, Oxford

Weinberg, F. J., Hom, K., Oppenheim, A. K., and Teichman, K. 1978, *Ignition by plasma jet*. Nature, **259**, 341-347.

Wright Jr., H. A., 1970, *The electrodeless spark underwater sound source*, Avco Government Products Group, Lowell, MA

Patents

Patents 1988, Canadian patent 1268851 and U. S. patent 099,344, *Method and Apparatus for Generating Underwater Acoustics*, Clements, R. M., Pitt, P. L., Ridley, J. D., Smith, R. D. and Topham, D. R.

The Near and Far Radiation Fields

A pulsating compact source in an infinite environment will produce acoustic waves that spread spherically outward. The waveform will be dependent upon the distance r from the center of the source but will be independent of the spherical angles θ and ϕ if the source is spherically symmetric. The wave produced at a large distance r will be as though the source were a sphere located at the origin expanding and contracting radially.

It is shown in Chapter 5 that a spherical bubble in an infinite fluid environment produces a pressure pulse given by

$$\Delta p = \rho \left[\frac{R}{r} \left(R \frac{d^2R}{dt^2} + 2 \left(\frac{dR}{dt} \right)^2 \right) - \frac{1}{2} \frac{R^4}{r^4} \left(\frac{dR}{dt} \right)^2 \right] \qquad \text{(A1)}$$

where p is the pressure at a point r distant from the center of a sphere of radius R. Equation (A1) shows that the particle velocity is composed of two terms, the ***far field***, dominated by the 1/r term, and the ***near field***, dominated by the $1/r^4$ term. At large distances the near field term becomes insignificant compared with that of the far field.

One author [Kramer et al. 1968] attributes the near field term physically to motion of water particles circumferentially along the spherical wavefront when the pressure wave compresses the water as it passes. Near a source, where pressures are higher, the effect would be more noticeable than at distance where pressures are lower.

Underwater acoustics use of the ***far field*** : Pressure measurements in underwater acoustics are made from sources that are usually immersed reasonably near the water surface. A hydrophone deployed at some distance from the source will detect a pressure wave from the source directly plus a pressure wave reflected from the water-air interface. Because of the differing acoustic impedances of air and water, the reflected wave is inverted compared to the direct wave. This reflected wave is sometimes called the "ghost" [Parkes and Hatton 1986]. Because of the small additional travel time the ghost signature takes to reach the hydrophone, the ghost signature adds directly with latter parts of the primary signature. Figure A1.1 shows the essential features of this phenomenon.

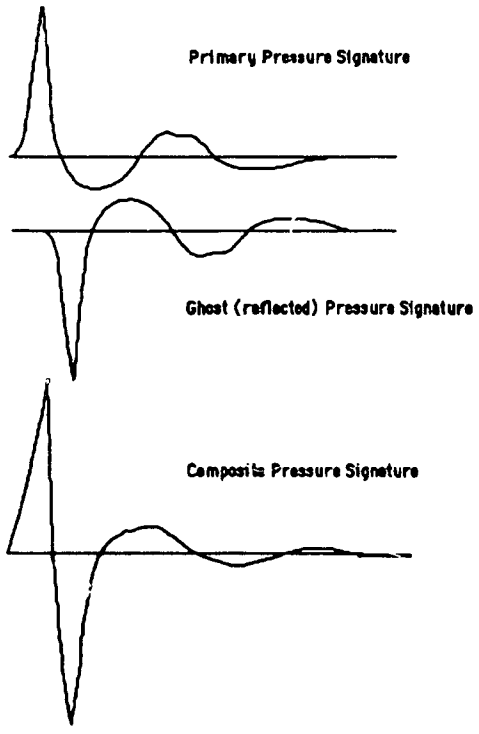

Figure A1: Development of composite pressure signature by the addition of the primary and reflected pressure signatures.

In general, when the far field is discussed by underwater acousticians it is understood that the receiving hydrophone is located perpendicularly under the surface sufficiently far from the source and the surface so that the pressure signature received results from the primary pressure and the reflected pressure signatures convolving to produce a vertically traveling pressure signature [Parkes and Hatton 1986]. The term far field is frequently misapplied to pressure signatures not produced by strictly vertically traveling waves, the reflected portion of the signature may be at a considerable angle, particularly in shallow water.

In a special report of the Society of Exploration Geophysicists Technical Standards Committee, Johnston et al. [1988] defined the near field and far field signatures. These definitions are quoted below:

Near-field signature

A near field signature is an acoustic wavelet whose direct arrival from the marine source is very large (> 20 dB) compared with reflections from adjacent boundaries or interfaces. Near-field signatures are usually recorded for a single source or a point source. A point source is one whose dimensions are small compared with the shortest wavelength of interest, $L << \lambda$.

Far-field signature

A far-field signature is characterized by a direct wavelet plus its reflection (ghost) from the air-water interface. The ratio of the direct-to-ghost travel distances should approach 1.0. Far-field signatures are usually recorded for an array of sources (a directional source). A directional source is one whose dimensions are of the same order as the wavelengths of interest, $L \approx \lambda$.

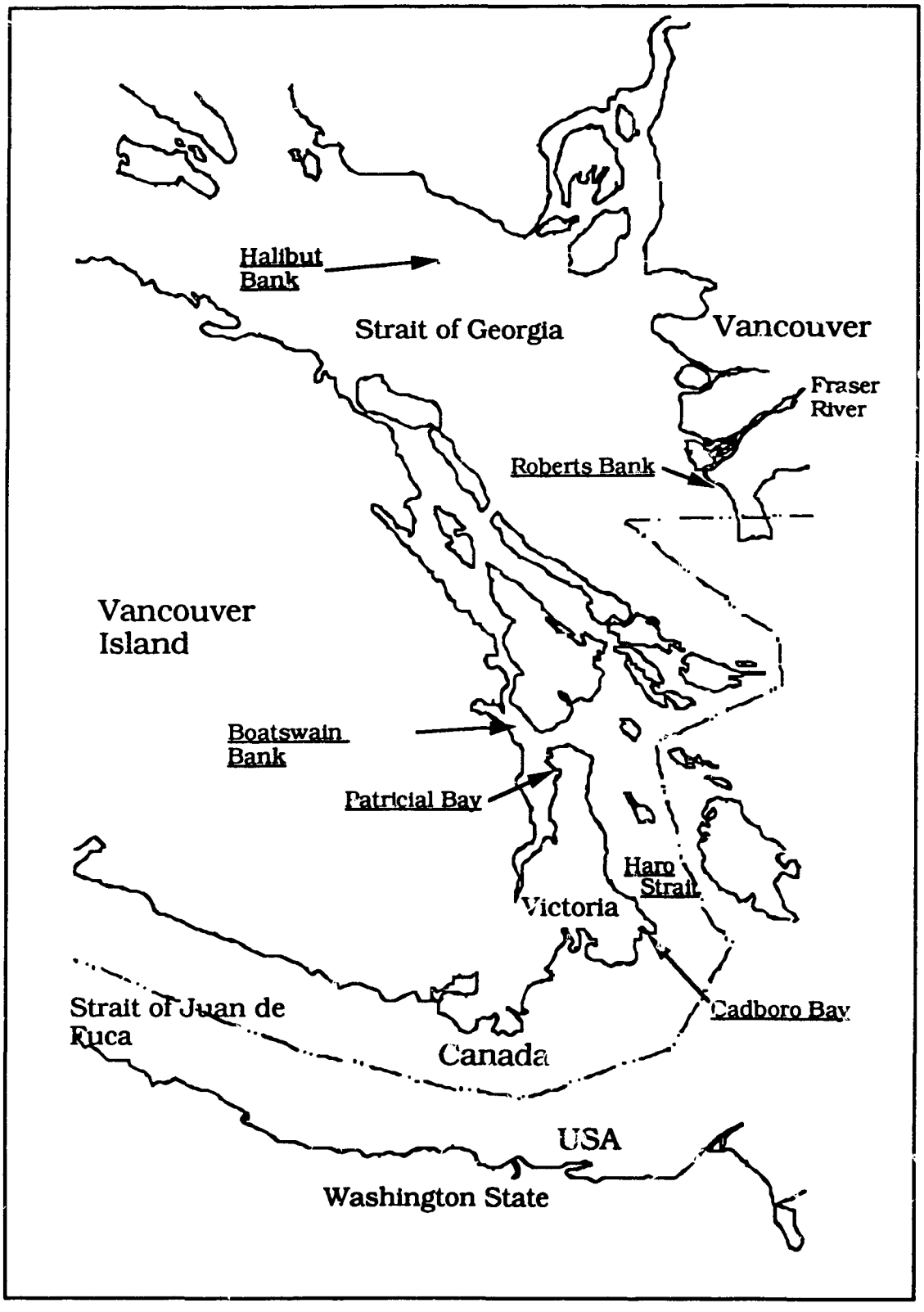
Halibut Bank
Strait of Georgia
Vancouver
Fraser River
Roberts Bank
Vancouver Island
Boatswain Bank
Patricial Bay
Haro Strait
Victoria
Strait of Juan de Fuca
Cadboro Bay
Canada
USA
Washington State